International Journal of Polymer Science

Preparation and Application of Conducting Polymer-Based Nanocomposites

Lead Guest Editor: Yang Liu
Guest Editors: Lin Zhang, Feng Wu, and Chao Zhang

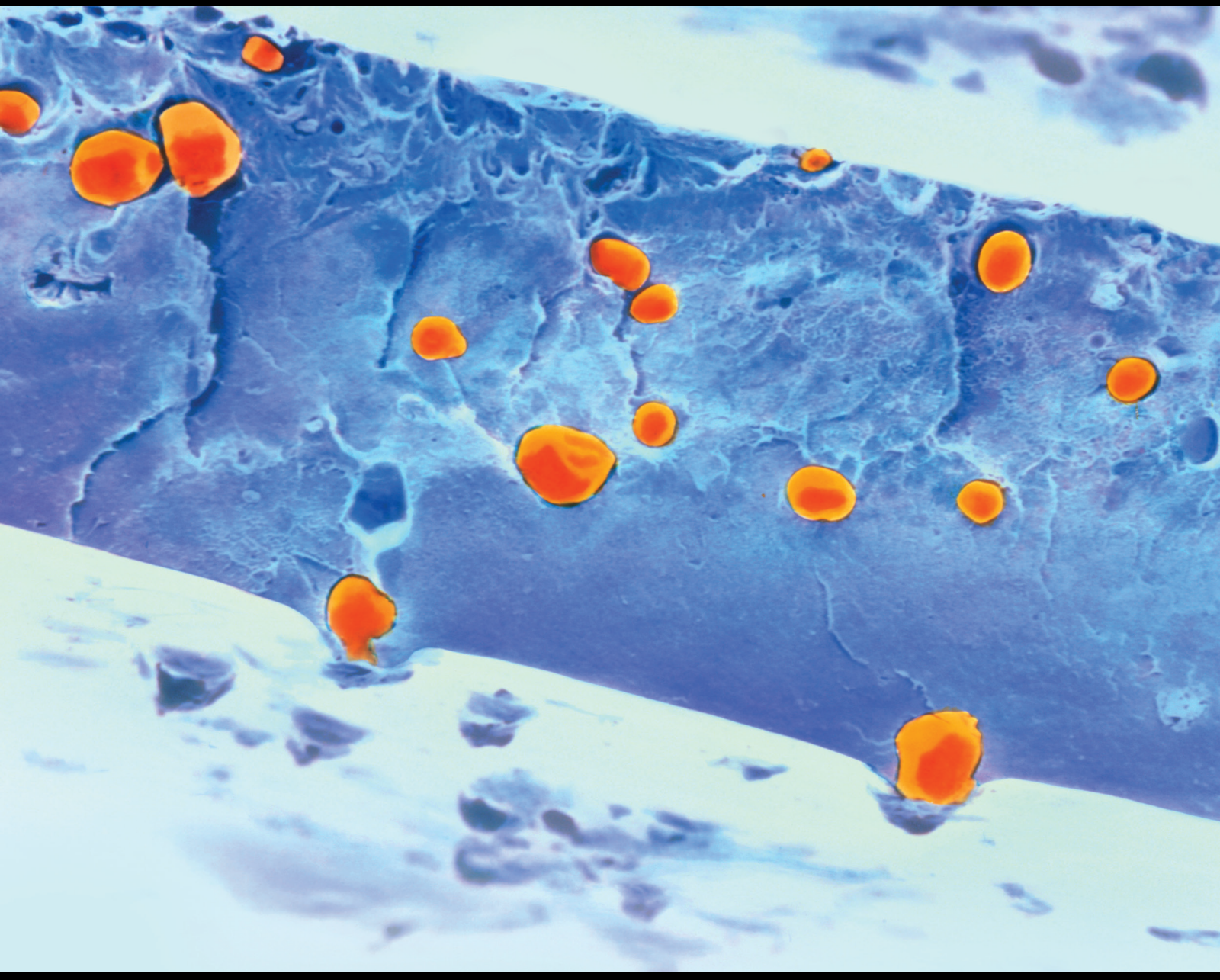

Preparation and Application of Conducting Polymer-Based Nanocomposites

International Journal of Polymer Science

Preparation and Application of Conducting Polymer-Based Nanocomposites

Lead Guest Editor: Yang Liu
Guest Editors: Lin Zhang, Feng Wu, and Chao Zhang

Chief Editor

Academic Editors

Contents

Hindawi
International Journal of Polymer Science
Volume 2020, Article ID 9031535, 10 pages
https://doi.org/10.1155/2020/9031535

Research Article

Facile Synthesis of Hollow Carbon Nanospheres by Using Microwave Radiation

Jiareng Chen, Jiaqi Lin, Bin Cui, and Yang Liu

Department of Biomedical Engineering, Sun Yat-sen University, Guangzhou, China 510006

Correspondence should be addressed to Yang Liu; liuyang56@mail.sysu.edu.cn

Received 16 December 2019; Revised 8 February 2020; Accepted 13 February 2020; Published 11 March 2020

Academic Editor: Huining Xiao

Carbon-based nanomaterials have attracted much research interest in recent years due to their excellent chemical and physiological properties such as chemical stability, low cytotoxicity, and biocompatibility. The traditional methods to prepare hollow carbon nanospheres require complicated instrumentation and harsh chemicals, including high-temperature furnace, gas inlets, and hydrogen fluoride etching. Herein, we propose a new strategy to prepare hollow carbon nanospheres in a simple and fast manner by using microwave radiation. Polypyrrole-coated silica core-shell nanoparticles (SiO_2@PPy NPs) were firstly prepared and subsequently processed by microwave radiation and aqueous alkaline solution to obtain the hollow carbon nanospheres. This facile method has potent potential to be utilized in the preparation of different types of hollow carbon nanospheres with various microstructure and elemental composition.

1. Introduction

Carbon nanomaterials, such as carbon nanospheres, mesoporous carbon nanomaterials, and carbon dots, are considered to be important for the next-generation structural, energy, and bioengineering materials due to their unique physical, chemical, optical, mechanical, and thermal properties, together with their high stability, good conductivity, and high biocompatibility. Carbon nanospheres have been widely explored and applied in different research fields [1, 2], such as electrode materials [3], flexible electronic devices [4], bioimaging [5], and drug carriers [6]. For example, sodium-ion hybrid supercapacitors which used mesoporous Nb_2O_5@-Carbon core-shell nanoparticles and reduced graphene oxide as the anode material showed high energy/power densities and long cycle life [7]. Carbon dots, synthesized from the folic acid, exhibited selectivity towards cancer cells with folate receptors, making such cells easily distinguishable in fluorescence microscopy imaging [8]. A DOX-loaded HB5-modified mesoporous carbon nanomaterial-based drug delivery system provides highly efficient methods for the treatment of HER2-positive cancers, which has better therapeutic efficacy and lower side effects [9]. Among variant morphology of carbon, hollow carbon nanospheres have received more and more attention due to their unique properties such as encapsulation ability, controllable permeability, surface functionality, high surface-to-volume ratios, and excellent chemical and thermal stability [10]. The application prospects of hollow carbon nanospheres are broad. The traditional preparation methods of hollow carbon nanospheres include emulsion synthesis [11], soft-templating synthesis [12], hard-templating synthesis [13], modified Stöber method [14], and template-free strategy [15]. These methods often need to be carried out under high temperatures and pressures, while the process is complicated, and the processing time is considerably elongated [16]. Furthermore, it was hard to control the morphology of the target product during the soft-templating synthesis, and the template removal process was often challenging during the hard-templating synthesis [10].

Herein, we intend to use a microwave rapid nanosynthesis method to synthesize hollow carbon nanospheres. As a nontoxic and biocompatible conductive polymer material, PPy has been used in electrode materials [17], in vivo photodynamic and photothermal therapy [18], etc. We have explored a rapid synthesis method of hollow carbon

Table 1: Microwave parameters of each group.

Samples	Carbon fiber mass (mg)	SiO_2@PPy NPs : carbon fiber (mass ratio)	Microwave time (min)	Subsequent treatment
MW1	1	100 : 1	5	H_2O washing
MW2	3	100 : 3	5	H_2O washing
MW3	5	100 : 5	2	H_2O washing
Hollow C	1	100 : 1	5	NaOH stirring

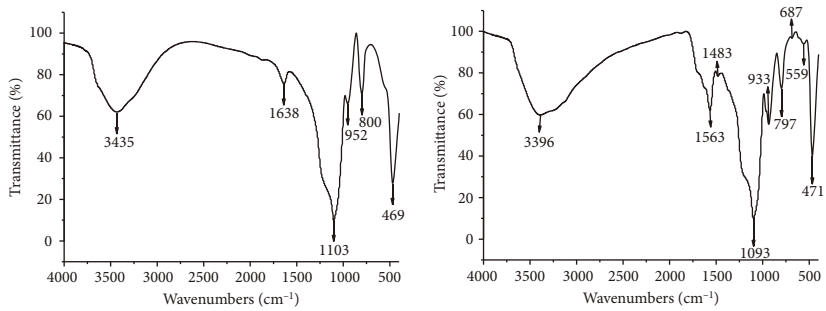

Figure 1: FT-IR spectra of (a) SiO_2 NPs and (b) SiO_2@PPy NPs.

nanospheres by using PPy as the carbon source under microwave irradiation. This method is environmentally friendly and eliminates the need of harsh conditions. It takes only a domestic microwave oven to synthesize the carbon nanospheres in a short time (1–30 min). Then, hollow carbon nanospheres are obtained by using NaOH to etch the template. By controlling the process parameters and precursor materials used in the microwave process, carbon nanospheres with different structure and morphology can be obtained.

2. Experimental Section

2.1. Materials. Tetraethyl orthosilicate (99.99%) was purchased from Aladdin. Ammonia solution (25%) and ethanol absolute (99.7%) were purchased from Tianjin Zhiyuan Reagent Co., Ltd. Pyrrole was purchased from Macklin. Chondroitin sulfate A sodium salt from bovine trachea was purchased from Sigma. Ammonium persulfate was purchased from Sinopharm Chemical Reagent Co., Ltd. Sodium hydroxide was purchased from Tianjin Damao.

2.2. Synthesis of SiO_2@PPy NPs. SiO_2 NPs were synthesized according to the classical method reported by Stöber et al. [19]. Briefly, add 5 mL ammonia water and 1 mL pure water to 50 mL ethanol with stirring. Add 5 mL tetraethyl orthosilicate (TEOS), and continue to stir for 2 h. After centrifugation (4000 rpm, 15 min), the products were washed by water twice and ethanol for one time, then dried to obtain silicon nanospheres. PPy coating was according to method described by Zhou et al. [20]. 0.2 g SiO_2 NPs templates were dispersed to 100 mL water by ultrasonic, and then 0.1 g Chondroitin sulfate A sodium salt was added to form a solution with a concentration of 0.001 g/mL. The solution was stirred overnight, so that the SiO_2 NPs could fully absorb chondroitin sulfate. 0.070 mL pyrrole monomer was added to the mixture. Then $(NH_4)_2S_2O_8$ (0.228 g, 10 mL H_2O) was added to the system, and the mixture was stirred at 4°C for 12 h. The samples were washed twice by water and once by alcohol (5500 rpm, 20 min), then dried for 12 h at 60°C.

2.3. Microwave SiO_2@PPy NPs and Template Etching. After mixing 100 mg SiO_2@PPy NPs with carbon fiber at different mass ratios, microwave reactions were initiated at 1000 W in different reaction time. The conditions for each group are recorded in Table 1 and named as MW1, MW2, and MW3. Then the microwave products were washed and centrifuged (5500 rpm, 15 min) to obtain the carbonization products with silicon spheres templates. Silicon cores were then removed by stirring in 1 M NaOH, and the Hollow C was obtained.

3. Results and Discussion

According to the method reported by Zhou et al. [20], we synthesized SiO_2@PPy NPs as templates for carbonization. In this method, the SiO_2 NPs surfaces are modified by chondroitin sulfate A sodium (CSA) so that the PPy can be doped by the CSA molecules in situ. Besides, the CSA molecules are negatively charged so they can repel each other and make the PPy layer uniformly distributed. In order to inspect the functional groups on the surface of the samples, we use Fourier transform infrared spectroscopy (FT-IR) to characterize the as-synthesized SiO_2@PPy NPs (Figure 1). In Figures 1(a) and 1(b), the absorption peaks near 3400 cm^{-1} are attributed to H-O-H stretching [21]. In Figure 1(a), the strong peaks at 1103, 800, and 469 cm^{-1} corresponded to the antisymmetric vibration peaks of Si-O-Si and the symmetric and curved vibration peaks of Si-O bonds. The peak at 952 cm^{-1} belongs to the bending vibration absorption of Si-OH. In Figure 1(b), the absorption at 1563 cm^{-1} is assigned to C-C stretching or C-N stretching [22]. The band at 1483 cm^{-1} corresponds to C-N stretching, and it may also contribute by the

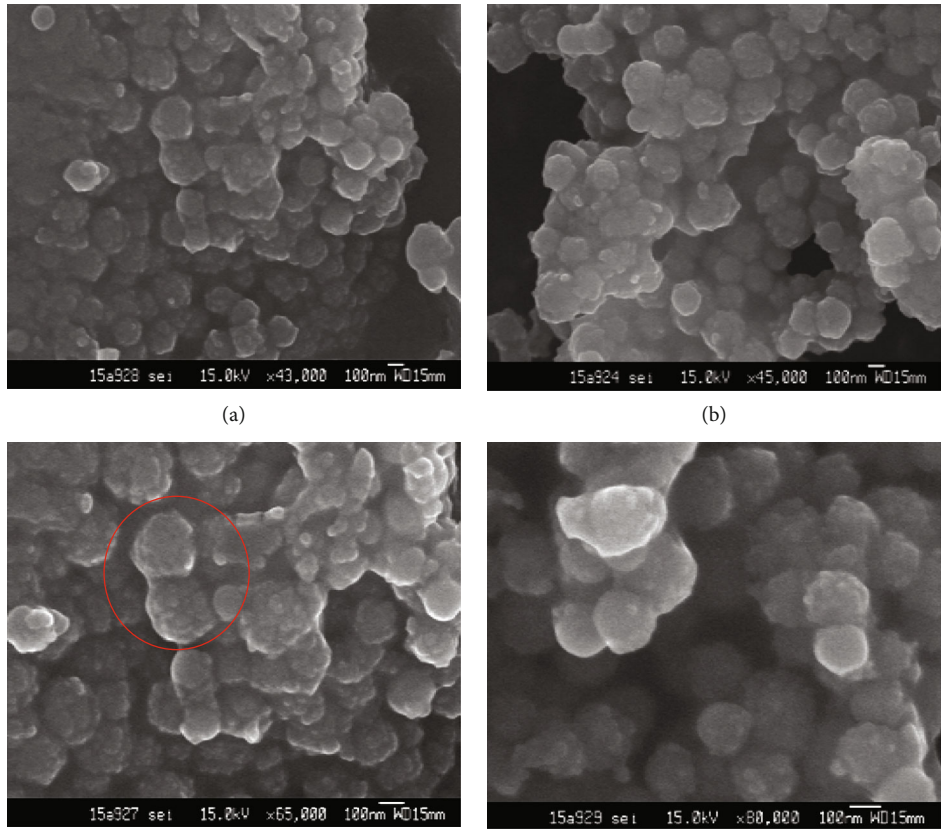

Figure 2: SEM images of (a–d) SiO_2@PPy NPs in different magnifications. (c) is the close up view of (a) and shows the separation state of SiO_2@PPy NPs.

dissymmetrical and symmetric ring-stretching modes [23]. The peaks near 1220 cm^{-1} and 933 cm^{-1} suggest the doped state of PPy [23]. By comparing Figures 1(a) and 1(b), we speculated that the PPy shells of SiO_2@PPy NPs are thin because of the strong Si-O-Si stretching absorption peak near 1100 cm^{-1}. The characteristic absorption peaks of PPy on the SiO_2@PPy NPs surfaces indicate that PPy is successfully coated on the surfaces of SiO_2 NPs.

We then use scanning electron microscope (SEM) to analyze the shape and size of the as-prepared SiO_2@PPy NPs. In Figure 2, we can see that compared to the SiO_2 NPs (Figure S1), the surface of SiO_2@PPy NPs is considerably rougher. The PPy was found to precipitate on the surface of the SiO_2 NPs, forming particulate microstructure. Due to the cross-linking of the PPy coating, the as-obtained SiO_2@PPy NPs generally exhibited an aggregated morphology under SEM, but the structure of individual SiO_2@PPy NPs can be still clearly identified (Figure 2(c)). In the SEM images, the particle sizes of the SiO_2@PPy NPs are measured to be ranged from 200 nm to 300 nm. The existence of PPy coating on the surface of the SiO_2@PPy NPs was further verified by transmission electron microscopy (TEM). In Figure 3, it can be observed that the SiO_2@PPy NPs have a core-shell structure. From the red-circle-marked part of Figure 3(d), the phase boundary between PPy and silica can be seen clearly. The SiO_2 NP can be observed as the solid core, while PPy forms an intact and continuous thin nanoshell on the silica surface. The average thickness of the PPy nanoshells was measured to be 19.62 ± 1.78 nm based on the TEM images. A series of experiments were also conducted to explore the appropriate diameter of silicon spheres (Figure S1, Table S1). Next, we investigated the effect of CSA concentration on the thickness of PPy shell (Figure S2 and S3). In Figure S2, it is obvious that the surface of the spheres in the CSA-doped group (Figure S2b-f) is rougher than that in the control group (Figure S2a) without CSA doping. It indicates that CSA can modify the surface of SiO_2 NPs and promote the coating of PPy. TEM was then used to compare the difference of PPy coating obtained from five different CSA concentrations (Figure S3). Among them, the PPy layer of the 0.1 wt% group (Figure S3a) is the most uniform and continuous. With increasing the concentration of CSA, the agglomeration of SiO_2@PPy NPs becomes weaker, and the granular shape of PPy on SiO_2 NPs surface becomes more obvious. And in the 0.4 wt% and 0.5 wt% groups, where the CSA concentrations are over 0.3 wt% (Figure S3d and S3e), it shows obvious discontinuity of PPy shells. The weaker agglomeration of SiO_2@PPy NPs is the effect of CSA for it can play a role in constructing the grid structure in the reaction and effectively disperse the SiO_2 NPs via electrostatic interactions [20]. The CSA chains with lots of

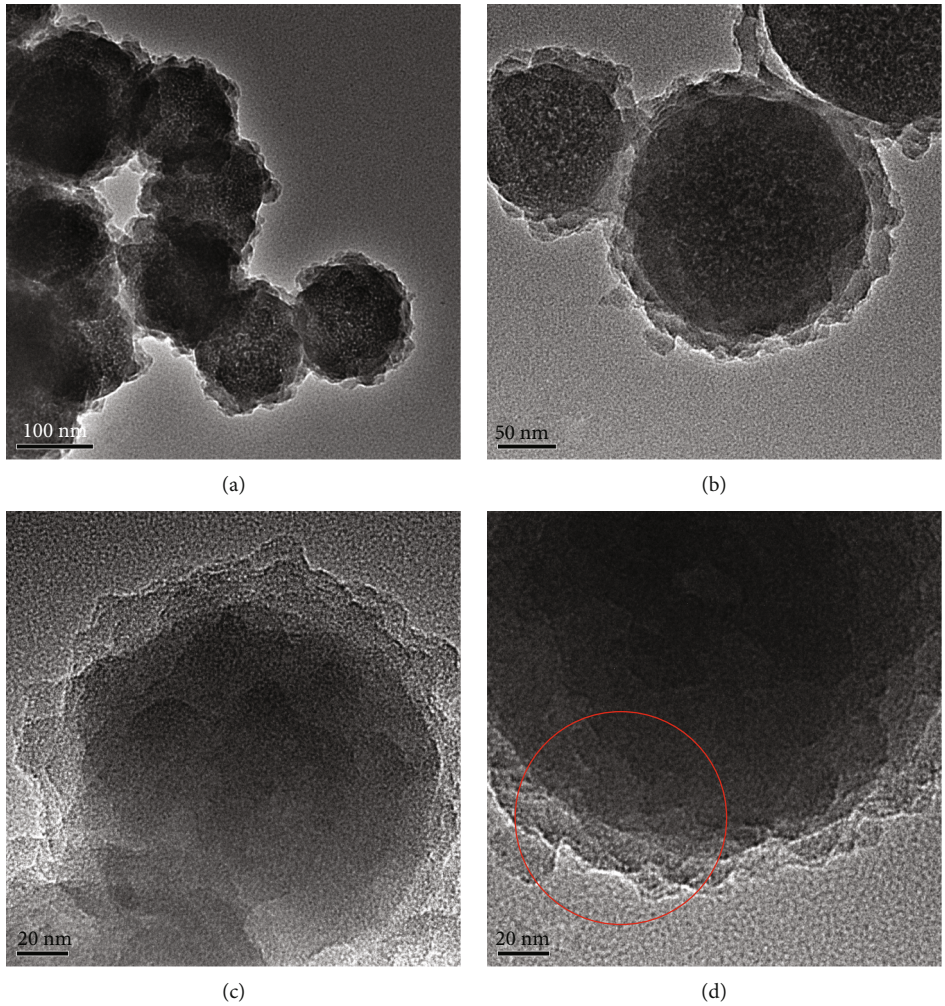

Figure 3: TEM images of (a–d) SiO_2@PPy NPs in different magnifications. (d) is the close view of (b). (d) The circled part shows the double-layer structure clearly.

sulphonic ($-SO_3^-$) and carboxylic ($-COO^-$) groups can interact with Py^+ and form intermediate complexes [24]. When the oxidative polymerization was triggered, the PPy was preferentially formed along the CSA chains [24]. In higher CSA concentrations (≥0.3 wt%), more CSA molecules would adsorb on the surface of the SiO_2 NPs, resulting in higher steric hindrance that hinders the formation of a continuous PPy coating layer. To explore the relationship between size and CSA concentration, we randomly counted more than 50 SiO_2@PPy NPs for each of the different CSA concentrations. The size (in SEM figures) and thickness (in TEM figures) distributions are shown in Figure S4. In the 0.2 wt% group, the SiO_2@PPy NPs feature the largest average size (245.08 ± 6.11 nm) and the thickest PPy layer (23.60 ± 2.20 nm). When the concentration is higher than 0.2 wt%, with increasing the concentration of CSA, the size of SiO_2@PPy NPs becomes smaller, and the PPy layers become thinner.

The SiO_2@PPy NPs were then microwave-treated under different conditions in Table 1, which were labeled as microwave-treated products 1–3 (MW1, MW2, and MW3), and samples obtained after a 1 mol/L NaOH stirring treatment were named as hollow carbon nanospheres (Hollow C). The morphology and microstructure of the products after microwave radiation were characterized by TEM. In Figures 4(a)–4(c), we can clearly see the shells' morphology changed after microwave, and the SiO_2@C NPs still maintain the core-shell structure. The average thickness of shells of SiO_2@C NPs is 29.5 ± 5.5 nm. Compared to the SiO_2@PPy NPs, the shells of the products after microwave radiation become thicker, and the larger standard deviation indicates the heterogeneity of shells. These changes indicate that carbonation reactions may have taken place in the products during microwave. After stirring in NaOH solution, we can obtain carbon nanospheres with hollow core formed by removing SiO_2 NPs templates, and the average hollow size is 135.7 nm (Figures 4(d)–4(f)). The edges of the hollow cores in Hollow C are smooth; however, the shells are heterogeneity, and most of them are incomplete. Also, there is no porous structure that can be observed in Hollow C.

Elemental analysis (EA) was conducted on SiO_2@PPy NPs and SiO_2@C. In Table 2, it can be seen that the weight percentage of carbon elements of SiO_2@PPy is around 15% and is similar to the products after microwave. In the

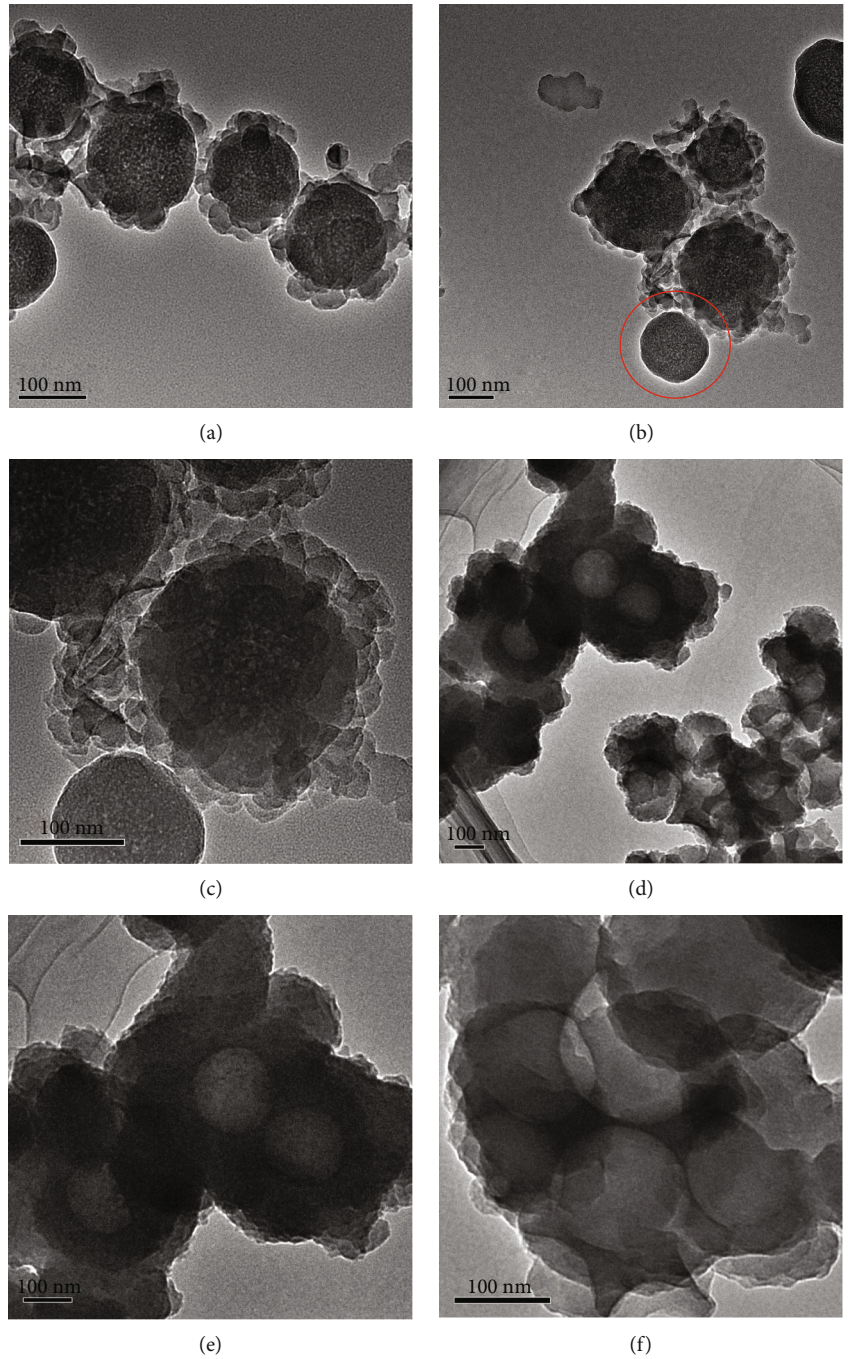

Figure 4: TEM images of SiO_2@C NPs (a–c) and Hollow C (d–f). (b) The circled part shows one of the cores lose its shell during the reaction.

Table 2: EA results of SiO_2@PPy, samples after microwave, and Hollow C.

Samples	C%	H%	N%	C/H	C/N
SiO_2@PPy	15.65	2.51	3.99	6.2313	3.9223
MW1	15.86	2.22	4.33	7.1487	3.6588
MW2	15.45	1.97	4.28	7.8247	3.6111
MW3	15.55	2.1	4.15	7.3967	3.7439
Hollow C	38.06	2.79	10.48	13.654	3.6302

meantime, the C/H ratio increases from 6.2313 to over 7 after microwave radiation, which indicates that SiO_2@PPy is carbonized. Hollow C is the product of MW1 after NaOH treatment, and the contents of carbon, nitrogen, and C/H ratio are 38.06%, 10.48%, and 13.654. Compared to MW1, these parameters significantly increased, which suggests that the effect of microwave carbonization is good and the SiO_2 NPs were successfully etched. Carbon cannot be dissolved by the aqueous alkaline solution so it remains after NaOH stirring resulting in the increase of weight percentage of carbon elements and C/H ratio. This demonstrates that the

carbonization reaction happened. As can be seen from Table 2, the sum of the percentage of C, H, and N elements is only slightly higher than 20% in SiO_2@C while in Hollow C it is slightly more than 50%. It shows that there are other elements in the samples with a high content cannot be detected, considering to be Si and O elements.

In the process of microwave radiation, it is the PPy in the shell to be carbonized, so we are more concerned about the change of element content in the surface. X-ray photoelectron spectroscopy (XPS) was used to study the surface element content. Figure 5 shows that the samples contain elements such as Na, S, Si, O, N, and C, and the atomic percentages of various elements can be obtained by integrating the peak area (Table 3). The Na and S elements come from the CSA added, and Si comes from silicon sphere core. Meanwhile, peaks at around 533 eV are attributed to O1s, which can be derived from CSA and SiO_2 NPs detected through the shell in SiO_2@PPy NPs and SiO_2@C NPs. Peaks at 400 eV and 285 eV are N1s and C1s peaks. Nitrogen mainly comes from the PPy heterocyclic ring, and carbon comes from the carbon skeleton of the products.

According to the results, the atomic percentage of C elements is the highest (75.4%), followed by O, Si, and N in SiO_2@PPy NPs. In MW1 and MW2, the C content decreases to 57.76% and 55.44%, respectively, after the microwave treatment, while the C content in MW3 is significantly higher (70.09%) than MW1 and MW2. However, there are only slight differences among the C contents of the MW1, MW2, and MW3 samples according to the EA analysis. It thus indicates that during the sample preparation process of MW3, a higher mass ratio of the carbon fiber and a shorter microwave time may result in a higher C content on the sample surface. The EA analysis of the O element indicates that the atomic percentage of O in MW3 increases slightly to 19.83% and in MW1 and MW2 increases up to 27.34% and 28.42%, respectively. Compared with the EA result that the weight percentage of C has no obvious change in SiO_2@PPy NPs and SiO_2@C, this shows that the C elements do not lose a lot in the reaction and it is the addition of O elements in the shells that mainly causes the decrease of the proportion of C elements in SiO_2@C. Also, these changes indicate that the effect of microwave time on the element ratio of C and O is greater than the mass ratio of carbon fiber in the precursor. By increasing the radiation time, the carbon content decreases while the oxygen content increases. As for the percentage of Si elements, it is 2.9% in SiO_2@PPy NPs and increases to 8.82%, 9.88%, and 3.62% in MW1, MW2, and MW3 individually. The possible cause of this is that a portion of the SiO_2 cores lost their shells in the reaction, which can be seen in Figure 4(b) (red circle), and the reaction between SiO_2 and C is also expected to attribute to this. SiO_2 can be reduced by carbon under the high temperature, and the happening of this reaction can also let a few Si elements mix into the shells.

Compared with MW1 washed by water, the proportion of carbon atoms in the products treated by NaOH increases to 78.85%, while the proportion of silicon elements decreases to 1.16%, and the weight percentages of C and N elements

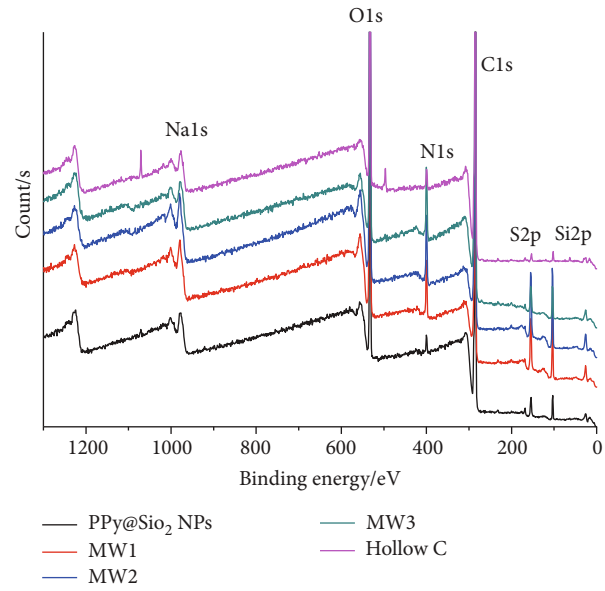

Figure 5: XPS results of SiO_2@PPy NPs, samples after microwave, and Hollow C.

Table 3: The atomic percentages and peak positions of different elements obtained by XPS characterization of SiO_2@PPy NPs, samples after microwave, and Hollow C.

Elements	SiO_2@PPy NPs	MW1	MW2	MW3	Hollow C
C peak (eV)	284.8	284.81	284.82	284.81	284.79
C (%)	75.4	57.76	55.44	70.09	78.85
O peak (eV)	532.63	533.03	532.99	532.81	532.2
O (%)	19.57	27.34	28.42	19.83	17.14
N peak (eV)	399.78	399.77	399.81	399.83	399.72
N (%)	1.53	6.09	6.26	6.15	2.02
Si peak (eV)	103.45	103.81	103.76	103.78	102.1
Si (%)	2.9	8.82	9.88	3.62	1.16

both increase in the EA results. It shows that the silicon cores were successfully etched, and Hollow C was obtained. However, the percentage of silicon atoms on the surface decreases by only 7.66%, while the percentage of carbon atoms increases by 21.09%. This suggests that the percentage of carbon atoms rise is not totally formed by removing the silicon cores, and there are some other reasons: (1) The oxygen content decreases in Hollow C, which may be caused by the break of the noncovalently bound between CSA and the particles. (2) The nitrogen in the system mainly exists in the heterocyclic ring of PPy, which content also decreases after NaOH treatment. This indicates that the residual PPy in the shells was also removed. However, the increase of weight percentage of N in the EA results is because of the etching of silicon cores.

The deconvolution of the XPS peaks was performed by using the software of XPSpeak41 (Figure 6). It can be seen that the proportion of C-C is the largest in C1s and the remaining components of C=C, C=O, and C-O are basically

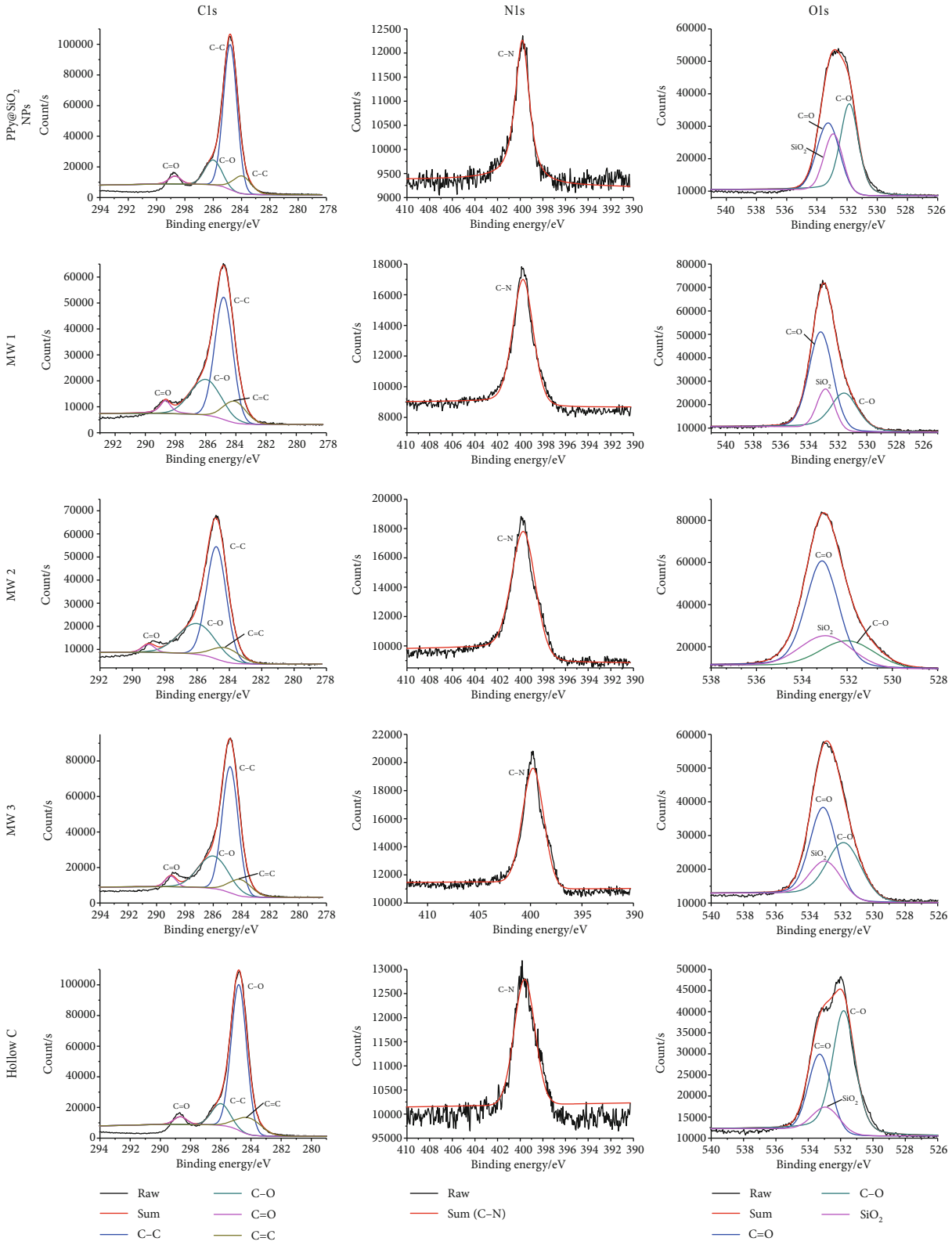

Figure 6: XPS spectra of each group in C1s, N1s, and O1s.

close. According to the peak separation of O1s, the ratio of C-O is higher than that of C=O in SiO_2@PPy NPs, and while the results change in the samples after microwave, the ratio of C=O exceeds that of C-O. The proportion of C-O in Hollow C is higher than that of C=O, which may be due to the aldol reaction or disproportionation. A part of C=O is reduced to C-O, so the proportion of C-O rises while the proportion of C=O decreases.

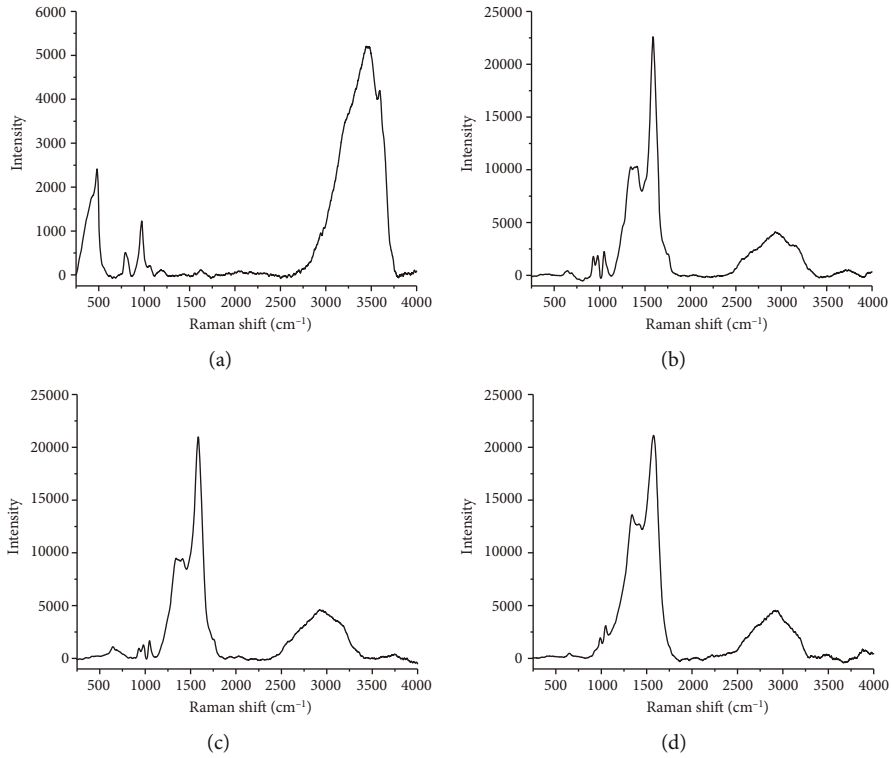

Figure 7: Raman results of (a) SiO_2 NPs, (b) SiO_2@PPy NPs, (c) SiO_2@C NPs, and (d) Hollow C.

Raman analyses were performed to deeper study the form of carbon in SiO_2 NPs, SiO_2@PPy NPs, SiO_2@C NPs, and Hollow C (Figure 7). In the spectrum of the SiO_2 NPs (Figure 7(a)), we can see a small peak at 460 cm^{-1} and a wide peak at 3454 cm^{-1}. These two peaks disappeared after PPy layers were coated (Figure 7(b)) and new peaks near 1360 cm^{-1} (D peak), 1580 cm^{-1} (G peak), and 2930 cm^{-1} (G +D peak) relating to carbon materials appeared [25, 26], which can also be observed in SiO_2@C NPs (Figure 7(c)) and Hollow C (Figure 7(d)). D-band represents structural defects of carbon, and G-band comes from in-plane vibration of sp^2-bonded crystalline carbon, so the I_D/I_G intensity ratio can give the information about the graphitization degree [26]. I_D/I_G is 0.46, 0.44, and 0.64 in SiO_2@PPy NPs, SiO_2@C NPs, and Hollow C, respectively. Compared to SiO_2@PPy NPs, I_D/I_G in SiO_2@C NPs is a little higher corresponding to the decrease of the proportion of C-C in XPS results. The increasing I_D/I_G ratio in Hollow C indicates the defects and the degree of nongraphitized carbon increased, which may be due to the change of oxygen-containing functional groups [27] and the reduction of sp^2 domains during the NaOH stirring.

Microwave heating method is expected to have the characteristics of faster heating rate and higher efficiency than the traditional heating method. By absorbing microwave energy, it heats the SiO_2@PPy NPs and turns them into SiO_2@C NPs. The absorbing properties of materials are mainly related to magnetic loss, dielectric loss, and transmissivity on the electromagnetic wave [28]. SiO_2 NPs was reported to be one of the most extensive application wave-transmitting materials [29, 30], and due to the interfacial polarization, coating the PPy shell on the SiO_2 core could increase the complex permittivity and dielectric loss [31]. In addition, CSA has negative charges, which can increase the permittivity of SiO_2@PPy NPs. What is more, the activated carbon fibers added can assist SiO_2@PPy NPs to absorb the microwave and enhance the heating effects [32]. The Raman results are similar in SiO_2@PPy NPs and SiO_2@C NPs; however, they have a significant difference in XPS results, which may indicate that changes mainly happened in forming oxygen-containing functional groups instead of the changing of the form of carbon during the microwave heating in an oxygen-containing atmosphere. Alkali could be used as a reagent to remove silica except HF to prepare hollow spheres [33, 34]. However, in this process, not only silica successfully etched, but also a number of oxygen-containing functional groups were reduced in Hollow C leading to the increase in the I_D/I_G ratio and the changes in the proportion of oxygen and carbon, which indicate that we get hollow carbon nanospheres.

4. Conclusions

In this paper, we reported a fast, convenient, and simple strategy to obtain hollow carbon nanospheres with a short-time microwave heating process and an aqueous alkaline solution treatment. We used silicon as the core and PPy coating layers as the shells. We further used the microwave method to carbonize the PPy shells into carbon shells. The SiO_2 NPs templates can be removed by NaOH to produce

the carbon nanospheres. Compared with the traditional carbonization methods, we only need a microwave oven to obtain the carbonization products with different structure and morphology in a few minutes, which is considered to be more energy saving and efficient. We believe that this microwave-assisted synthesis method can be extended for the efficient preparation of carbon nanospheres and the preparation of different carbon materials with different nanostructure.

Data Availability

The data used to support the findings of this study are included within the article and the supporting information.

Conflicts of Interest

The authors declare that there is no conflict of interest regarding the publication of this paper.

Acknowledgments

Financial support was from the College Students' Innovative Entrepreneurial Training Plan Program (201901165, 201901161), Ministry of Education of the People's Republic of China.

Supplementary Materials

The supporting information file contains the experimental details and results, including the scanning electron microscopy (SEM) images, tables containing the experimental parameters, and transmission electron microscopy (TEM) images, to support the discussions in the manuscript. Figure S1: SEM images of EH0 (a), EH1 (b), EH2 (c), EH3 (d), EH4 (e), EH5 (f), and EH6 (g) in the experiment controlled by alcohol/H2O ratio and ET1 (h), ET2 (i), ET3 (j), ET4 (k), and ET5 (l) in the experiment controlled by alcohol/TEOS ratio. Table S1: mean particle size and standard deviation of silica spheres. Figure S2: SEM images of SiO2@PPy NPs at (a) 0 wt%, (b) 0.1 wt%, (c) 0.2 wt%, (d) 0.3 wt%, (e) 0.4 wt%, and (f) 0.5 wt% concentration of CSA. Figure S3: TEM images of SiO2@PPy NPs at (a) 0.1 wt%, (b) 0.2 wt%, (c) 0.3 wt%, (d) 0.4 wt%, and (e) 0.5 wt% concentration of CSA. Figure S4: (a) sizes and (b) thicknesses distributions of SiO2@PPy NPs produced in different concentrations of CSA. *(Supplementary Materials)*

References

[1] Y. Qiao, D. Luo, M. Yu et al., "A precisely assembled carbon source to synthesize fluorescent carbon quantum dots for sensing probes and bioimaging agents," *Chemistry - A European Journal*, vol. 24, no. 9, pp. 2257–2263, 2018.

[2] P. Greil, "Perspectives of nano-carbon based engineering Materials," *Advanced Engineering Materials*, vol. 17, no. 2, pp. 124–137, 2015.

[3] S. Shahrokhian, M. Ghalkhani, R. Kohansal, and R. Mohammadi, "Biomimetic sensor for dobutamine employing nano-TiO_2/Nafion/carbon nanoparticles modified electrode," *Electroanalysis*, vol. 28, no. 5, pp. 970–978, 2016.

[4] L. Yuan, Y. Tao, J. Chen et al., "Carbon nanoparticles on carbon fabric for flexible and high-performance field emitters," *Advanced Functional Materials*, vol. 21, no. 11, pp. 2150–2154, 2011.

[5] J. Ge, Q. Jia, W. Liu et al., "Carbon dots with intrinsic theranostic properties for bioimaging, red-light-triggered photodynamic/photothermal simultaneous therapy in vitro and in vivo," *Advanced Healthcare Materials*, vol. 5, no. 6, pp. 665–675, 2016.

[6] B. Khezri, S. M. Beladi Mousavi, L. Krejčová, Z. Heger, Z. Sofer, and M. Pumera, "Ultrafast electrochemical trigger drug delivery mechanism for nanographene micromachines," *Advanced Functional Materials*, vol. 29, no. 4, article 1806696, 2019.

[7] E. Lim, C. Jo, M. S. Kim et al., "High-performance sodium-ion hybrid supercapacitor based on Nb_2O_5@carbon core–shell nanoparticles and reduced graphene oxide nanocomposites," *Advanced Functional Materials*, vol. 26, no. 21, pp. 3711–3719, 2016.

[8] S. K. Bhunia, A. R. Maity, S. Nandi, D. Stepensky, and R. Jelinek, "Imaging cancer cells expressing the folate receptor with carbon dots produced from folic acid," *Chembiochem*, vol. 17, no. 7, pp. 614–619, 2016.

[9] K. Wang, H. Yao, Y. Meng, Y. Wang, X. Yan, and R. Huang, "Specific aptamer-conjugated mesoporous silica-carbon nanoparticles for HER2-targeted chemo-photothermal combined therapy," *Acta Biomaterialia*, vol. 16, pp. 196–205, 2015.

[10] S. Li, A. Pasc, V. Fierro, and A. Celzard, "Hollow carbon spheres, synthesis and applications – a review," *Journal of Materials Chemistry A*, vol. 4, no. 33, pp. 12686–12713, 2016.

[11] H. Zhang, F. Ye, H. Xu, L. Liu, and H. Guo, "Synthesis of carbon hollow particles by a simple inverse-emulsion method," *Materials Letters*, vol. 64, no. 13, pp. 1473–1475, 2010.

[12] Z. C. Yang, Y. Zhang, J. H. Kong, S. Y. Wong, X. Li, and J. Wang, "Hollow carbon nanoparticles of tunable size and wall thickness by hydrothermal treatment of α-cyclodextrin templated by F127 block copolymers," *Chemistry of Materials*, vol. 25, no. 5, pp. 704–710, 2013.

[13] S. Kubo, R. Demir-Cakan, L. Zhao, R. J. White, and M. M. Titirici, "Porous carbohydrate-based materials via hard templating," *ChemSusChem*, vol. 3, no. 2, pp. 188–194, 2010.

[14] J. Liu, T. Yang, D. W. Wang, G. Q. Lu, D. Zhao, and S. Z. Qiao, "A facile soft-template synthesis of mesoporous polymeric and carbonaceous nanospheres," *Nature Communications*, vol. 4, no. 1, 2013.

[15] J. Kim, J. Han, D. Ha, and S. Kang, "Synthesis of nitrogen and boron co-doped carbon (CNB) and their CO_2 capture properties: from porous to hollow granule structure," *Journal of Materials Chemistry A*, vol. 2, no. 39, pp. 16645–16651, 2014.

[16] Y. Manawi, Ihsanullah, A. Samara, T. al-Ansari, and M. Atieh, "A review of carbon nanomaterials' synthesis via the chemical vapor deposition (CVD) method," *Materials*, vol. 11, no. 5, p. 822, 2018.

[17] F. Wang, X. Zhan, Z. Cheng et al., "Tungsten oxide@polypyrrole core–shell nanowire arrays as novel negative electrodes for asymmetric supercapacitors," *Small*, vol. 11, no. 6, pp. 749–755, 2015.

[18] X. Song, C. Liang, H. Gong, Q. Chen, C. Wang, and Z. Liu, "Photosensitizer-conjugated albumin-polypyrrole nanoparticles for imaging-guided in vivo photodynamic/photothermal therapy," *Small*, vol. 11, no. 32, pp. 3932–3941, 2015.

[19] W. Stöber, A. Fink, and E. Bohn, "Controlled growth of monodisperse silica spheres in the micron size range," *Journal of Colloid and Interface Science*, vol. 26, no. 1, pp. 62–69, 1968.

[20] L. Zhou, G. Tan, K. Ouyang, Y. Liu, and C. Ning, "Highly water-dispersible, highly conductive, and biocompatible polypyrrole-coated silica particles stabilized and doped by chondroitin sulfate," *Particle and Particle Systems Characterization*, vol. 32, no. 12, pp. 1068–1077, 2015.

[21] D. An, Y. Guo, B. Zou, Y. Zhu, and Z. Wang, "A study on the consecutive preparation of silica powders and active carbon from rice husk ash," *Biomass and Bioenergy*, vol. 35, no. 3, pp. 1227–1234, 2011.

[22] M. Marini, F. Pilati, and B. Pourabbas, "Smooth surface polypyrrole-silica core-shell nanoparticles: preparation, characterization and properties," *Macromolecular Chemistry and Physics*, vol. 209, no. 13, pp. 1374–1380, 2008.

[23] T. Dai, X. Yang, and Y. Lu, "Conductive composites of polypyrrole and sulfonic-functionalized silica spheres," *Materials Letters*, vol. 61, no. 14-15, pp. 3142–3145, 2007.

[24] Z. Zhou, W. Zhu, J. Liao et al., "Chondroitin sulphate-guided construction of polypyrrole nanoarchitectures," *Materials Science and Engineering*, vol. 48, pp. 172–178, 2015.

[25] J. Rani, S.-I. Oh, and J.-H. Jang, "Raman spectra of luminescent graphene oxide (GO)-phosphor hybrid nanoscrolls," *Maternité*, vol. 8, no. 12, pp. 8460–8466, 2015.

[26] C. Cheng, R. Fan, Z. Wang et al., "Tunable and weakly negative permittivity in carbon/silicon nitride composites with different carbonizing temperatures," *Carbon*, vol. 125, pp. 103–112, 2017.

[27] B. Liang, Z. Qin, T. Li et al., "Poly(aniline-co-pyrrole) on the surface of reduced graphene oxide as high- performance electrode materials for supercapacitors," *Electrochimica Acta*, vol. 177, pp. 335–342, 2015.

[28] J. Shen, K. Chen, L. Li, W. Wang, and Y. Jin, "Fabrication and microwave absorbing properties of (Z-type barium ferrite/silica)@polypyrrole composites," *Journal of Alloys and Compounds*, vol. 615, pp. 488–495, 2014.

[29] M. F. Casula, A. Corrias, and G. Navarra, "An EXAFS study on iron-cobalt-silica nanocomposite materials prepared by the sol-gel method," *Journal of Sol-Gel Science and Technology*, vol. 26, no. 1/3, pp. 453–456, 2003.

[30] J. Zhu, S. Wei, N. Haldolaarachchige, D. P. Young, and Z. Guo, "Electromagnetic field shielding polyurethane nanocomposites reinforced with core–shell Fe–silica nanoparticles," *The Journal of Physical Chemistry*, vol. 115, no. 31, pp. 15304–15310, 2011.

[31] J. Liu, Z. Wang, S. U. Rehman, and H. Bi, "Uniform core–shell PPy@carbon microsphere composites with a tunable shell thickness: the synthesis and their excellent microwave absorption performances in the X-band," *RSC Advances*, vol. 7, no. 84, pp. 53104–53110, 2017.

[32] T. Zou, N. Zhao, C. Shi, and J. Li, "Microwave absorbing properties of activated carbon fibre polymer composites," *Bulletin of Materials Science*, vol. 34, no. 1, pp. 75–79, 2011.

[33] X. Liu, Y. Liu, X. Shi, Z. Yu, and L. Feng, "Synthesis and catalytic performance of SiO_2@Ni and hollow Ni microspheres," *Applied Physics A*, vol. 122, no. 11, p. 987, 2016.

[34] C. Schliebe, T. Graske, T. Gemming, and H. Lang, "Metal nanoparticle-loaded porous carbon hollow spheres by twin polymerization," *Journal of Materials Science*, vol. 52, no. 21, pp. 12653–12662, 2017.

Hindawi
International Journal of Polymer Science
Volume 2020, Article ID 7659405, 10 pages
https://doi.org/10.1155/2020/7659405

Research Article

Silsesquioxane-Polythiophene Hybrid Copolymer as an Efficient Modifier for Single-Walled Carbon Nanotubes

Shuxi Gao, Xiaoyong Hu, Lei Zhang, Yuliang Mai, Hao Pang, Yongqiang Dai, and Bing Liao

Guangdong Provincial Key Laboratory of Industrial Surfactant, Guangdong Research Institute of Petrochemical and Fine Chemical Engineering, Guangzhou, 510000 Guangdong, China

Correspondence should be addressed to Shuxi Gao; gaoshuxi@163.com and Bing Liao; liaobing@gic.ac.cn

Received 8 October 2019; Accepted 30 December 2019; Published 11 March 2020

Guest Editor: Feng Wu

One silsesquioxane-polythiophene hybrid copolymer, with combined star-like structure and intramolecular heterogeneity, was synthesized and sufficiently characterized via various methods, including FTIR, NMR, and SEC measurements. According to the exploration and characterization results, it was much more efficient at modifying SWNTs than its linear analogs in aqueous solution. The hydrophobic silsesquioxane core and PEDOT chains could locally anchor to the surface of the nanotubes, while the soluble flexible copolymer chains extended into the solution and rigid conjugated chains provided some π-π stacking effect to enhance adhesive force with the conjugated structure of the carbon nanotube, imparting steric stabilization to nanotube dispersion. The noncovalent interaction with SWNTs and solubility in aqueous solution improved the electrochemical characteristics of the modified-SWNT composite and availed for the preparation of a flexible and transparent electroactive film. Accordingly, this kind of silsesquioxane-polythiophene hybrid copolymer will be forwarded to apply to the assembling of flexible optoelectronic devices.

1. Introduction

Carbon nanotubes (CNTs) classified as multiwalled nanotubes (MWNTs) and single-walled nanotubes (SWNTs), upon the wrapped amount of a graphite sheet, have been used in multiple fields, such as composites, optoelectronic devices, field emission display, and energy storage, due to their unique physical, chemical, and structural properties [1–3]. However, the poor solubility and dispersibility of CNTs in both aqueous and organic media are major barriers for CNT applications, especially for SWNTs, as a result of the strong Van der Waals interaction between CNTs [4–8].

In order to obtain fine dispersion of CNTs in aqueous solution, various approaches that primarily paid attention on dispersion and dissolution properties have been developed, including covalent surface and noncovalent surface functionalization strategies [9–14]. Noncovalent modification has received considerable attraction for the modification of surface properties with no damage to the sp2 structure of the nanotube surface, involving π-π interaction, hydrogen bonds, and ionic interaction by employing micromolecule surfactants or amphiphilic copolymers as modifiers.

In previously published works [15–17], copolymeric structures have the advantages of promoting CNTs' dispersibility in a wide range of solvents depending on the great affinity of hydrophobicity of the copolymers for the nanotube, and it has been demonstrated in several literatures that various polymers have effectively enhanced the long-term dispersion stability of CNTs through different types of interactions. Furthermore, the versatile chemistry of copolymer modifiers allows for tailoring and functionalizing polymer/nanotube composites with finely various properties, enhancing the application of CNTs, especially in fabricating carbon-based flexible transparent electrodes [18–21].

Herein, a novel star-shaped copolymer is reported to stabilize single-walled carbon nanotubes (SWNTs) in aqueous solution through noncovalent interactions. In the previous work of our team [4], we had adequately demonstrated that an octopus-shaped amphiphilic copolymer could generate a stable and uniform physical adsorption layer on a nanotube,

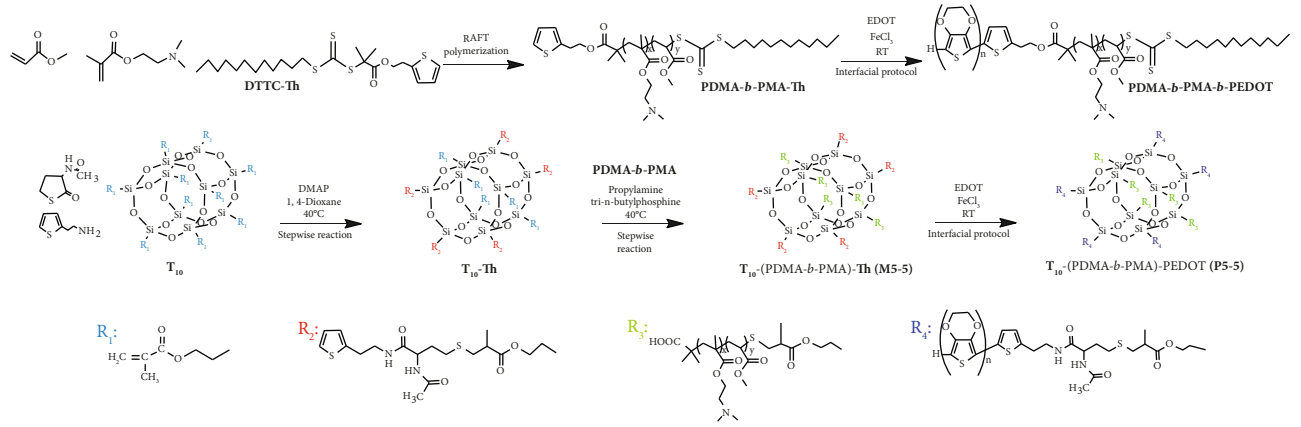

Scheme 1: Synthesis route to linear copolymers and star-shaped copolymers.

yielding much better efficiencies toward functionalization and dispersion, and multiple binding sites could assemble larger polymer aggregation that locally anchored onto the nanotube surface compared to its linear analogs that sequentially reduced the hydrophobicity of the sidewall surface for minimizing the connection with water and other tubes.

Therefore, we were motivated to extend SWNT modification to a silsesquioxane- (SQ-) cored star-like conjugated copolymer. Firstly, SQ would be convenient to constitute the core of star polymers. Secondly, the hydrophobic silsesquioxane cage could impart to amphiphilic copolymers' hydrophobic-hydrophobic interactions with CNTs [4]. Finally, the conjugated segments could generate π-π interaction between conjugated chains and the hybridized CNT surface [22–24].

Herein, we report a star-like conjugated copolymer $\mathbf{T_{10}}$-(PDMA-*b*-PMA)-PEDOT (**P5-5**) standing on hydrophobic cage-like decakis(methacryloxypropyl) silsesquioxane ($\mathbf{T_{10}}$) and the linear analog PDMA-*b*-PMA-*b*-PEDOT, to explore the mechanism of SQ-based star configuration and conjugated system generating the efficient dispersion of SWNTs.

2. Experimental Section

2.1. Materials. N,N-(Dimethylamine)ethyl methacrylate (DMA, Aladdin, 99%) and methyl acrylate (MA, Aladdin, 99%) were purified through passing over the basic aluminum oxide column. 2,2-Azobisisobutyronitrile (AIBN, Aladdin, 98%) was recrystallized twice in ethanol before use. Cage-like decakis(methacryloxypropyl) silsesquioxane ($\mathbf{T_{10}}$) was prepared in our laboratory [25]. Single-walled carbon nanotubes (SWNTs) were purchased from Aladdin (carbon content > 95%, OD × *L*: 1-2 nm × 5-30 μm).

2.2. Synthesis Processes. As described in Scheme 1, the experiments began from the precise synthesis of a $\mathbf{T_{10}}$-(PDMA-*b*-PMA)-Th polymer precursor (**M5-5**) that contained five thiophene groups. The polymer precursor was subsequently copolymerized with the EDOT monomer to form PEDOT branches grafted from the hydrophobic $\mathbf{T_{10}}$ core, and the extension of the conjugated system was realized at the interface between the immiscible organic and aqueous phases by a modified interfacial synthesis protocol (MIP) [24]. For comparative purposes and to further explore the dispersing efficiency, the linear analog was prepared by the RAFT method and subsequently grafted the EDOT monomer from the thiophene group (denoted as PDMA-*b*-PMA-*b*-PEDOT) in the MIP process.

The specific experimental procedures were described in supporting information with structural characterization information for all polymers and reaction intermediates.

2.3. Characterization. Size exclusion chromatography (SEC) was conducted at 35°C by a Waters 1515 series system equipped with Styragel HR4 and HR3 columns and a Waters 2414 refractive index detector. The system was calibrated by narrowly dispersed polystyrene standards, and HPLC-grade DMF was used for the mobile phase at 0.60 mL/min. Nuclear Magnetic Resonance (^{1}H NMR) spectra were characterized in deuterated chloroform by using a Bruker DMX-400 spectrometer with a Varian probe. Infrared spectra were obtained with a Fourier transform infrared spectrometer using the KBr method (FTIR, Bruker Tensor 27, Germany). The UV-vis spectra of samples were measured in THF solution (UV-1800, Shimadzu Co., Japan). Weight loss temperatures of the products were determined by using a thermogravimetric analyzer (TGA, Netzsch TG209F3) at 10°C/min under the nitrogen flow rate of 40 mL/min from 50–700°C. Transmission electron microscopy was performed on a high-resolution transmission electron microscope (HR-TEM, Tecnai G2 F20 S-TWIN). The electrochemical performance was determined with CHI660E employing a standard three-electrode electrochemical cell that consisted of a glassy carbon electrode as the working electrode, a saturated calomel electrode (SCE) as the reference electrode, and a platinum wire as the counter electrode. Cyclic voltammetry was carried out relative to an SCE reference electrode at different scan rates (20–100 mV/s), and the potential window of cycling was confined between -1 and 1 V. The electrochemical impedance spectroscopy (EIS) was performed in the frequency range of 10^5 to 10^{-2} Hz with the signal amplitude of 5 mV against the open-circuit potential. The electrical conductivity was subjected to the standard four-point probe method at ambient temperature (RTS-8, Four Probes Tech).

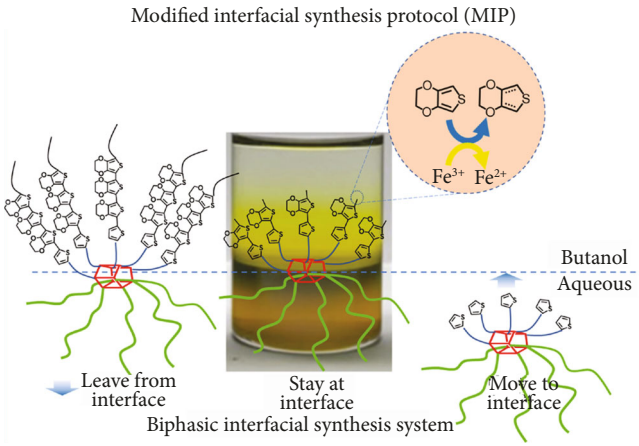

Scheme 2: Synthesis protocol of P5-5 through water/butanol interface.

3. Results and Discussion

3.1. Chemical Structural Characterization. Decafunctionalized SQ (T_{10}) was selected to construct the star-shaped copolymer because this viscous amorphous liquid cluster compound was synthesized with high yield, which could be afforded in large-scale use. In addition, T_{10} offers more available functionalities for multiple grafting of the polymer chains to the core, and it also effectively interferes in strong π-π interactions between neighboring conjugated chains, resulting in solution processability for the hybrid polymer [24].

In order to form the star-shaped copolymer precursor M5-5, a one-pot continuous reaction sequence was used to prepare the asymmetric T_{10} with five thiophene groups (T_{10}(5-5)), including a nucleophilic opening of the thiolactone by aminolysis and then a radical thiol-ene conjugation. Due to the extremely high reactivity of thiyl radical addition toward the carbon-carbon double bond, excess thiolactone could promote the conversion rate of amine and ensure complete conversion [26]; PDMA-*b*-PMA obtained by reversible addition-fragmentation transfer (RAFT) polymerization was linked to T_{10}(5-5) by thiol-ene conjugation after nucleophilic cleavage of the thiocarbonyl group.

The linear copolymer precursor was obtained by a typical RAFT polymerization procedure under the regulation of DTTC-Th as an efficient RAFT agent with an end-capped thiophene group.

Our particular synthetic approach (MIP) for the growth of conjugated chains relied on the reaction of the precursors and monomer by multicomponent oxidative coupling at the interface, which suppresses the interdiffusion of a monomer and an oxidant in the confined region to avoid uncontrolled homopolymerization, and also on the diffusion of the resulting copolymer down to the bottom phase due to the highly hydrophilic nature of the flexible arms and instability enhancement at the interface as the extension of the conjugated system, while being convenient for the rearrangement of unreacted precursors at the interface (Scheme 2).

^{1}H NMR, FTIR, UV-vis, and GPC analyses confirmed that the star-shaped conjugated copolymer and linear analogs were obtained with precise structure and low narrow molecular weight distribution, and the supporting information described the detailed experimental process and results (Figures S1–S8). All chemical structures are illustrated in Scheme 1, and the structural data are listed in Table 1.

3.2. Functionalized CNTs with the Silsesquioxane-Polythiophene Hybrid Copolymer and Its Linear Analog. Multiple modifier-functionalized SWNTs were obtained while avoiding inclusion of dissociative copolymers through multiple centrifugation and washing steps, yielding PDMA-*b*-PMA-Th with SWNTs (M1) and PDMA-*b*-PMA-*b*-PEDOT with SWNTs (M2) and P5-5 with SWNTs. As we know, π-π stacking interactions are strong interfacial noncovalent interactions between modifiers and CNTs, as it was indicated that conjugation groups located at the flexible chains of the copolymer resulted in higher adhesion [8]. For the copolymer/CNT composites, the employed thiophene moieties in the flexible PDMAEMA could endow the copolymer strong π-π interactions with CNT, functioning as interfacial linkers between the modifiers and SWNTs. Thus, the anchor groups at the flexible chains of modifiers could be adhered tightly along the CNT surface to form stronger interfacial interaction in the modifier-CNT complex.

3.2.1. Transmission Electron Microscopy (TEM). For the purpose to confirm the strong and stable interfacial interactions between SWNTs and modifiers, we conducted transmission electron microscopy (TEM) analysis. As observed in Figure 1, all nanotubes retained their structural integrity, revealing that no damage was evident to the nanotube walls in the experiment; the modified SWNTs apparently tended to exist as individuals or small bundles, especially for P5-5/SWNTs, despite well-known property that the pristine SWNTs would aggregate and be entangled to form large ropes without any modification. In addition, these star-shaped copolymer-modified SWNTs had more individually dispersed nanotubes and less bundles, compared to linear copolymer-modified SWNTs; moreover, the star-shaped copolymer aggregates homogeneously adhered to the surface of the nanotube without large agglomeration. From the figures of individual SWNTs (Figure 1, insets), many arc-like bulges were observed on the surface of P5-5 modified nanotubes, attributed commonly to regions of irregular copolymer coating along the lengths; however, many linear copolymer-modified nanotubes were still bounded together, which might be due to the disorderly stacking of a large copolymer and resulting in the lack of relatively strong noncovalent forces to stabilize individual tubes. Of the two linear copolymer-modified nanotubes, PDMA-*b*-PMA-*b*-PEDOT-modified SWNTs had less entanglement (Figure 1(b)).

3.2.2. Fourier Transform Infrared Spectroscopy (FTIR). Direct evidences of modifier-nanotube interactions could also be obtained using Fourier transform infrared spectroscopy (FTIR) after dispersion and centrifugation. As displayed in FTIR spectra of pristine SWNTs and modified SWNTs (Figure 2), the IR absorption bands occurred with maxima around 3450 cm^{-1}, which correspond to the –OH stretching

Table 1: Structural characterization of all copolymers.

Polymer	Yield (%)	M_w [a] (kg/mol)	M_w/M_n [a]	M_n [b] (kg/mol)	M_n [c] (kg/mol)	$N_{(thiophene)}$ [f]	$N_{(M_n)}$ [d]	$N_{(M_w)}$ [e]	DP_{EDOT} [b]	DP_{EDOT} [a]
PDMA-*b*-PMA	65	17	1.2	15	15	—	—	—	—	—
PDMA-*b*-PMA-Th	65	21	1.3	20	20	1	—	—	—	—
PDMA-*b*-PMA-*b*-PEDOT	70	22	1.3	21	21	1	—	—	6/6	6/6
M5-5	75	81	2.2	78	80	5	5.1	4.6	—	—
P5-5	50	91	2.2	92	—	—	—		85/17	70/14

[a]Molecular weights and polydispersity indexes determined by SEC in DMF on the basis of polystyrene calibration. The number of grafted EDOT and the approximate polymerization degree of EDOT in each PEDOT chain were calculated on SEC results. [b]M_n, the number of grafted EDOT, and the approximate polymerization degree of EDOT in each PEDOT chain were calculated on ^{1}H NMR results. [c]M_n was calculated on speculative structure construction. [d]The grafting number of PDMA-*b*-PMA in macromonomer precursors was calculated by the equation $N_{(M_n)} = M_n$(macromonomer precursor)$/M_n$(PDMA-*b*-PMA). [e]The grafting number of PDMA-*b*-PMA in macromonomer precursors was calculated by the equation $N_{(M_w)} = M_w$(macromonomer precursor)$/M_W$(PDMA-*b*-PMA). [f]The number of thiophene rings of macromonomer precursors was calculated on ^{1}H NMR results.

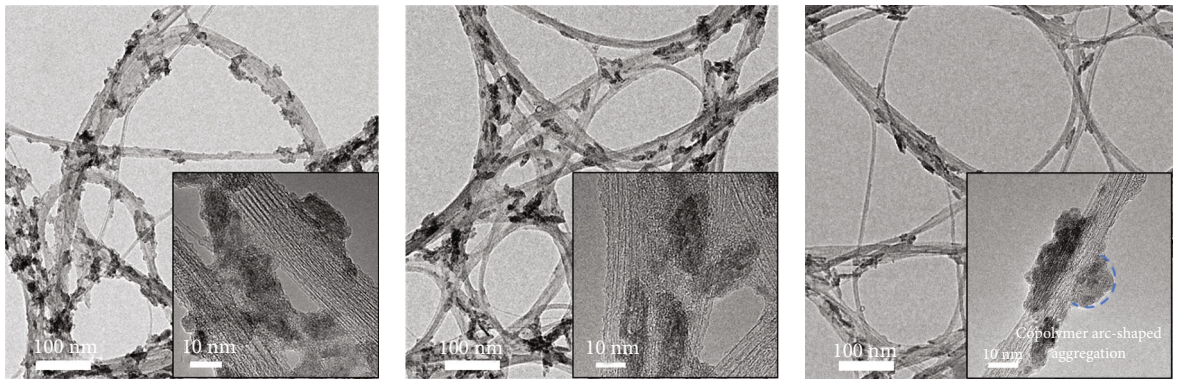

(a) (b) (c)

Figure 1: HR-TEM images of the modified SWNTs: PDMA-*b*-PMA-Th/SWNTs (a), PDMA-*b*-PMA-*b*-PEDOT/SWNTs (b), and P5-5/SWNTs (c). The insets show the morphology of PDMA-*b*-PMA-Th, PDMA-*b*-PMA-*b*-PEDOT, and P5-5 surrounding the surface of the CNTs in (a), (b), and (c), respectively.

vibration of surface hydroxyl groups on CNTs and the adsorbed water molecules. An intense band at 1636 cm^{-1} appeared in all samples was assigned to the stretching vibration of carbonyl groups (C=O) present in carboxylic acids and conjugated C=C groups on the nanotubes. Besides, in the spectra of modified SWNTs, an obvious C=O stretching vibration of ester groups in polymer chains (ca. 1718 cm^{-1}) and C–O stretching vibrations (ca. 1233 and 1149 cm^{-1}) were observed; the observation suggested that the modifiers were still effectively wrapped onto the nanotube surface by noncovalent interactions after rinsing. Compared to the spectra of modifiers (Figure S9), the characteristic peak of PEDOT chains (ca. 850 and 988 cm^{-1}) shifted toward higher wavenumbers due to the electron-deficient defects of the nanotube surface and might confirm the π-conjugated stacking between the PEDOT segment and the nanotube surface, revealing the adherence of copolymers to the nanotube surface.

3.3. Dispersion Properties

3.3.1. UV-vis Spectrogram. For the assessment of the variation of dispersion efficiency of SWNTs modified by the star-like copolymer and its linear analogs in aqueous solution, three modified-SWNT (m-SWNT) dispersions (M1, M2, and M3) were prepared and investigated by using a UV-vis spectrogram. Figure S10 shows the absorption profiles of SWNT dispersions in a modifier THF/water solution; nearly no obvious signal peaks could be detected for SWNT dispersion modified by linear copolymers (M1, M2) in the UV-vis region. Moreover, there were no evident changes in the absorption spectra with or without the modifiers, causing us to tentatively suppose that the nanotube structure had not been destroyed in the solubilization process. In the absorption profiles for PDMA-*b*-PMA-*b*-PEDOT solution and P5-5 solution (Figure 3), a wide absorption band from 450 to 550 nm was observed in the spectra, which could be attributed to the characteristic π-π^* transition in conjugated polythiophene backbones [27].

Furthermore, we presumed that the amount of the nanotube stabilized by modifiers in dispersion would be reduced after centrifugal separation, and the UV absorption intensity of supernatants could represent the amount of well-stable nanotube suspension. As indicated from Figure 3, the absorption intensity of the supernatants for both PEDOT-

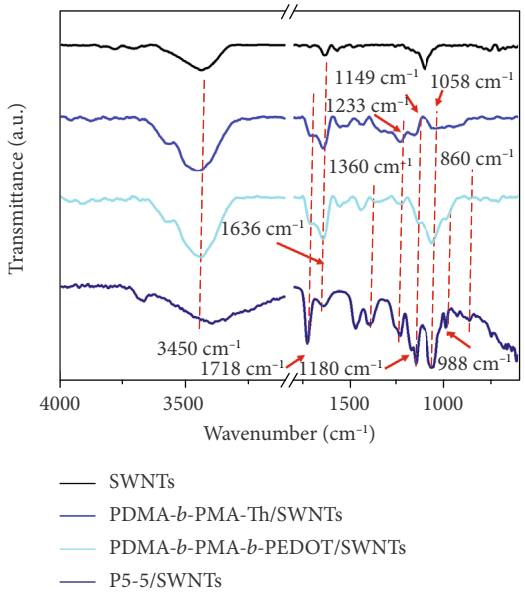

Figure 2: Infrared spectrogram of pristine SWNTs and modified nanotubes.

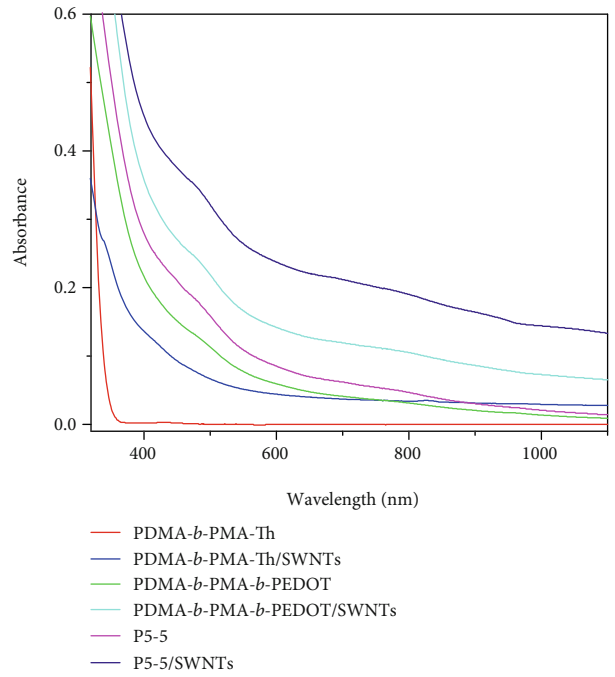

Figure 3: Absorption profiles for the modifier solution and supernatant of SWNT dispersion. The supernatant was obtained by merging the centrifugal supernatant and the washing liquid (the total volume of washing liquid was four times as much as the volume of dispersion), and all copolymer solutions were diluted to 1/5 of their original concentration [4].

grafted modifiers (M2 and M3) was enhanced significantly in comparison with the original polymer solutions diluted in the same ratio, despite the fact that it was not obvious in comparison with the M1 supernatant with PDMA-*b*-PMA-Th solution; in addition, the M3 supernatant had the maximum enhancement of absorption intensity. The variation of dispersion efficiency resulted from the noncovalent modification, which was probably relevant to the configuration, the silsesquioxane cage, and the PEDOT segments.

3.3.2. Visual Sedimentation. It was well known that pristine SWNTs could not be stabilized in aqueous solution without the help of a modifier, despite the vigorous ultrasonication, due to the highly specific surface area and hydrophobic sidewall surface. For the modified SWNTs, the modification ability of polymers on SWNTs could be visually assessed by conducting a sedimentation experiment to compare the stability of modified-SWNT dispersions (Figure S11). All modifiers had the ability to enhance the dispersity of SWNTs, especially PEDOT-grafted copolymers. In particular, it seemed that the star-shaped copolymer/SWNT dispersion had more stability than linear ones, which was observed in a vial over 10 days without any precipitation. Therefore, we inferred that the SQ cage and PEDOT segments played key roles for noncovalent functionalization of nanotubes: Firstly, due to the hydrophobic nature of SQ cores and PEDOT segments, they should be gathered close to the surface of the carbon tube. Secondly, the poor solubility and conjugated nature of PEDOT imparted effective physisorption between the stabilizer and the conjugated structure of the nanotube. Thirdly, thanks to the tentacles of multiarm SQ-based copolymers with rigid arms, the solvation segments would produce more opportunities to generate a great affinity for solvent, which primarily decreased the interfacial tension of nanotubes by minimizing their contacts with water [28], and more hydrophobic segments could provide more opportunities to interact with the nanotube surface. This speculation can be strongly supported by the fact that the SQ-based star copolymer employing multi-PEDOT chains compared to its linear analogs resulted in an improved functional capability to stabilize SWNTs.

3.3.3. Thermogravimetric Analysis (TGA). For the purpose of obtaining a more quantitative picture of the extent of nanotube functionalization, thermogravimetric analysis (TGA) was conducted to evaluate the thermodynamic property of copolymer/SWNT complexes and further estimate the well-adhered polymers on the nanotube surface under an N_2 atmosphere after centrifugation; all thermal property data are listed in Table 2. The copolymers (PDMA-*b*-PMA-Th, PDMA-*b*-PMA-*b*-PEDOT, and P5-5) and copolymer/SWNTs complexes (M1 residue, M2 residue, and M3 residue) (Figure 4) both indicated a distinct two-step thermal degradation, which might be caused by the loss of ester bonds and the decomposition of the backbone in the temperature range of 200–500°C, while no mass loss of the SWNTs was observed in the same temperature range.

The highest decomposition temperature at the maximum degradation rate in the second stage for thermal degradation of the framework structure of P5-5 indicated that the star-shaped configuration and the presence of T_{10} contributed to the increase in thermostability (Figure S12) [29].

Table 2: Thermogravimetric analysis data of various copolymers and modified-SWNT residues.

	$T_{max,1}$ (°C)	$T_{max,2}$ (°C)	C_{700}[a] (%)
T_{10}	418	—	43.7
PDMA-*b*-PMA-*b*-Th	325	421	5.5
PDMA-*b*-PMA-*b*-PEDOT	320	406	5.1
P5-5	307	430	12.2
PEDOT	325	375	30.4
M1 residue	281	398	72.2
M2 residue	280	402	60.4
M3 residue	295	412	56.1

[a]C_{700} represented the percentage residue of various samples at 700°C.

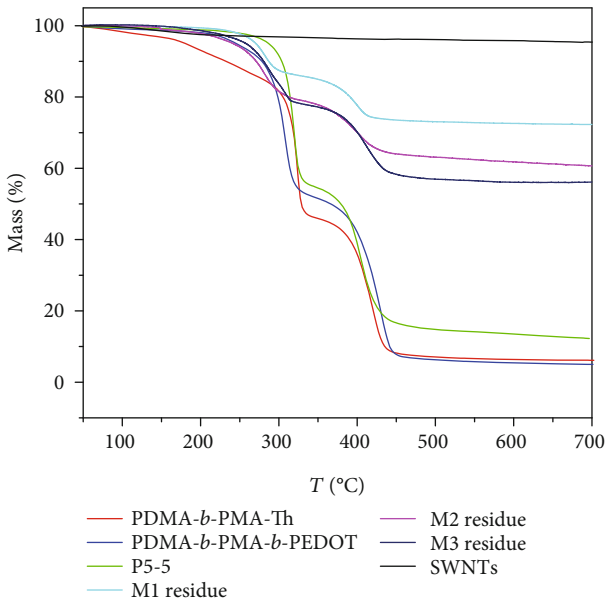

Figure 4: TGA curves of the modifiers, modified-SWNT residues, and pristine SWNTs.

The lower decomposition temperature of the PEDOT homopolymer might result in the lower decomposition temperature in the second stage of the PDMA-*b*-PMA-*b*-PEDOT trace (Figure S13), and the successful grafting of PEDOT segments from the thiophene group of PDMA-*b*-PMA-Th was further verified.

In addition, the C_{700} values of PDMA-*b*-PMA-Th, PDMA-*b*-PMA-*b*-PEDOT, and P5-5 were 5.5, 5.1, and 12.6%, and the C_{700} values of M1 residue, M2 residue, and M3 residue were 72.2, 60.4, and 56.1, respectively. As indicated in Figure 3 (TGA traces), the copolymers would be completely decomposed over 500°C; the mass loss from the residues of copolymer/SWNT complexes during thermal degradation could be used to estimate the amount of well-wrapped copolymers on the nanotubes in dispersion, and it was, respectively, about 25%, 35%, and 44% corresponding to the loss of PDMA-*b*-PMA-Th, PDMA-*b*-PMA-*b*-PEDOT, and P5-5 between 200°C and 500°C deducing that the mass loss of SWNTs, further combined with UV spectra, could be used to evaluate the functional capability of modifiers to stabilize SWNTs.

M1 residue had the least mass loss with the lowest dispersion efficiency of M1; that is, most of PDMA-*b*-PMA-Th was washed out due to the unstable physisorption on SWNTs; it implied that the grafting of PEDOT segments played an important role to form stable interactions with nanotubes in solution, which endowed more stacking interaction and hydrophobicity between modifiers and the surface of the nanotube. As expected, M3 residue had the largest mass loss compared with the linear ones with the best dispersion efficiency of M3, indicating that more P5-5 was well wrapped on the surface of nanotubes resulting in the largest polymer content in residue, thus providing strong support for the previous proposal: more possibilities would be obtained by introducing more solvation segments to generate a great affinity for solvent, and more hydrophobic segments and conjugated segments could provide more opportunities and π-stacking to interact with the nanotube, which powerfully enhanced adhesion on the surface to avoid dissolving even during several washing steps.

3.3.4. Mechanism. On the basis of the above results, the possible mechanism for elucidating the interaction between SWNTs and copolymers in Figure 5 was put forward. Thanks to the hydrophobic interaction and π-π stacking system between star-shaped copolymers and the sidewall, originating from the hydrophobic CSQ cores and conjugated PEDOT segments, the modifiers were readily adsorbed onto the surface of nanotubes by forming relatively strong noncovalent forces, and the other flexible solvable tentacles on the opposite side of the carbon tube had to stretch to the solvent as linear "buoys" due to the steric hindrance endowed by silsesquioxane cages. Thereby, a mass of spherical modifiers was inclined to absorb onto the sidewall to form arc-shaped copolymer aggregation which could decrease the hydrophobicity of the sidewall for minimizing the direct contact with water and other tubes. Meanwhile, these "buoys" tremendously enhanced the solubility of SWNTs in aqueous solution, thus causing well-dispersed SWNTs. In contrast, linear modifiers would be irregularly distributed in solvent due to lack of restrictions from the CSQ cage; therefore, the solvable copolymer chains would wrap the nanotube by generating hydrogen bond interactions. Although the PEDOT chains in PDMA-*b*-PMA-*b*-PEDOT could provide some π-π stacking effect to enhance adhesive force with the graphite structure of the surface, but the linear copolymers were difficult to form well-organized aggregations to prevent bundling of tubes.

3.4. Electrochemical Property. The electrochemical characteristics of thin films prepared by spin coating from copolymer solutions and the supernatant of modified-SWNT dispersions were determined to provide information about the structure of copolymers and dispersion efficiency. The quasi-rectangle-shaped cyclic voltammetry (CV) curves of PDMA-PMA-*b*-PEDOT P5-5 in Figure S14 were similar to those of soluble PEDOT analogs [30], the curves indicated similar chemically reversible signals during the process of positive and negative scans, and low potentials of the current onsets verified the highly electron-rich

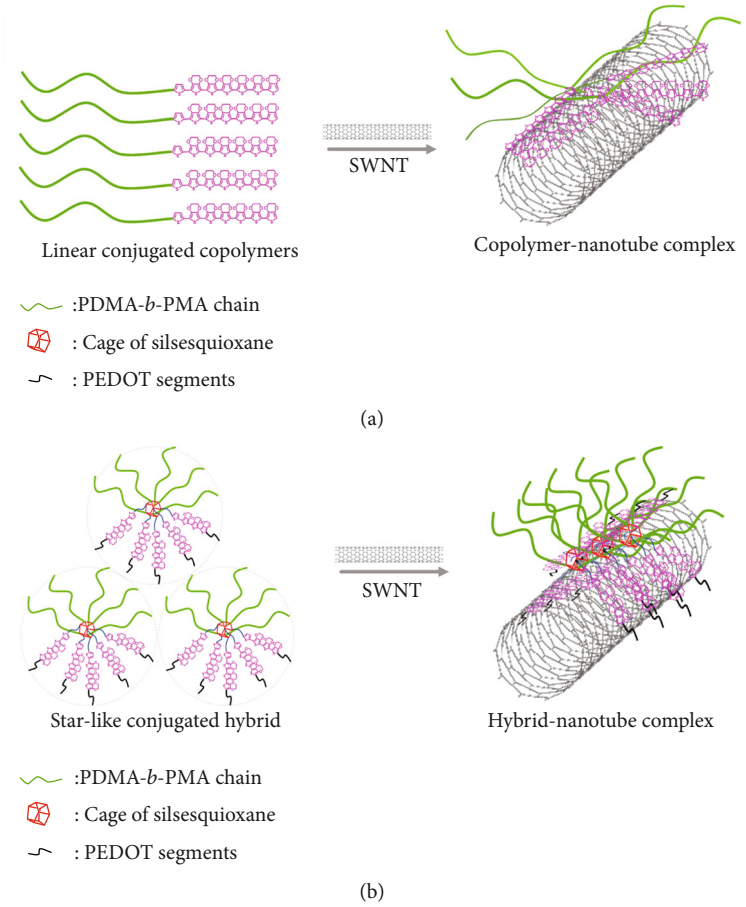

Figure 5: Mechanism between SWNTs with modifiers.

nature of the polymer films. As shown in the CV curves, a negative shift was observed in the oxidation potential (E_{ox}) values for PDMA-*b*-PMA-*b*-PEDOT (0.84 V) and P5-5 (0.75 V), possibly due to the larger conjugation system in P5-5. In addition, the larger curve area in the P5-5 film indicated that it had a higher specific capacitance that was imparted by the more PEDOT chains for facilitating ion motion.

In order to further study the stabilizing effect endowed by the conjugation and configuration of modifiers, which could be reflected by the electrochemical variation of modified-SWNT composite films, cyclic voltammetry (CV) and electrochemical impedance spectroscopy (EIS) measurements were conducted on the composite films. From Figure 6(a), CV curves of the P5-5/SWNT composite film and PDMA-*b*-PMA-*b*-PEDOT/SWNT composite film showed a quasirectangle shape with a couple of peaks, indicating an electrical double-layer capacitance originated from the redox reactions of PEDOT chains [31]. As we know, a large surface area and good electrical conductivity may enhance capacity properties, and the curve area of the P5-5/SWNT composite film was greater than that of the PDMA-*b*-PMA-*b*-PEDOT/SWNT composite film and PDMA-*b*-PMA-Th/SWNT composite film; it was clearly indicated that the hybrid copolymer, P5-5, possesses maximum PEDOT segments and star configuration, which was beneficial to facilitating ion motion to increase the specific capacitance of the composite film.

Furthermore, the internal resistance of modified-SWNT films, arising from the physical contact between components and the electron transfer resistance between the active materials and the substrate, could reflect the adhesion and π-π stacking system between copolymers and the nanotube [32–34]. Therefore, electrochemical impedance spectroscopy (EIS) measurements were performed from 10^5 Hz to 0.01 Hz. As shown in Figure 6(b), the resistance of the electrolyte (R_{sol}) corresponded to the intercept of the Nyquist diagrams on the Z real axis; the charge transfer resistance (R_{ct}) on the electrode was represented on the diameter of the semicircle in the Nyquist plots; the Warburg resistance (R_w) was associated with the slope of the straight line portion in the Nyquist plots at low frequency, correlating with the frequency dependence of ion diffusion to the electrode interface in the electrolyte. Obviously, R_{sol} values for the P5-5/SWNT composite film (12.7 Ω), PDMA-*b*-PMA-*b*-PEDOT/SWNT composite film (12.9 Ω), and PDMA-*b*-PMA-Th/SWNT composite film (13.4 Ω) were quite similar for the same electrochemical system. Predictable results, in which R_{ct} values were in the order of the P5-5/SWNT composite film (76 Ω) < PDMA-*b*-PMA-*b*-PEDOT/SWNT composite film (116 Ω) < PDMA-*b*-PMA-Th/SWNT composite film (>186 Ω), indicated that PEDOT chains and silsesquioxane cages tended to assist the charge migration, while further implying that the star-shaped copolymer could stabilize more nanotubes via more π-π interaction and hydrophobic-

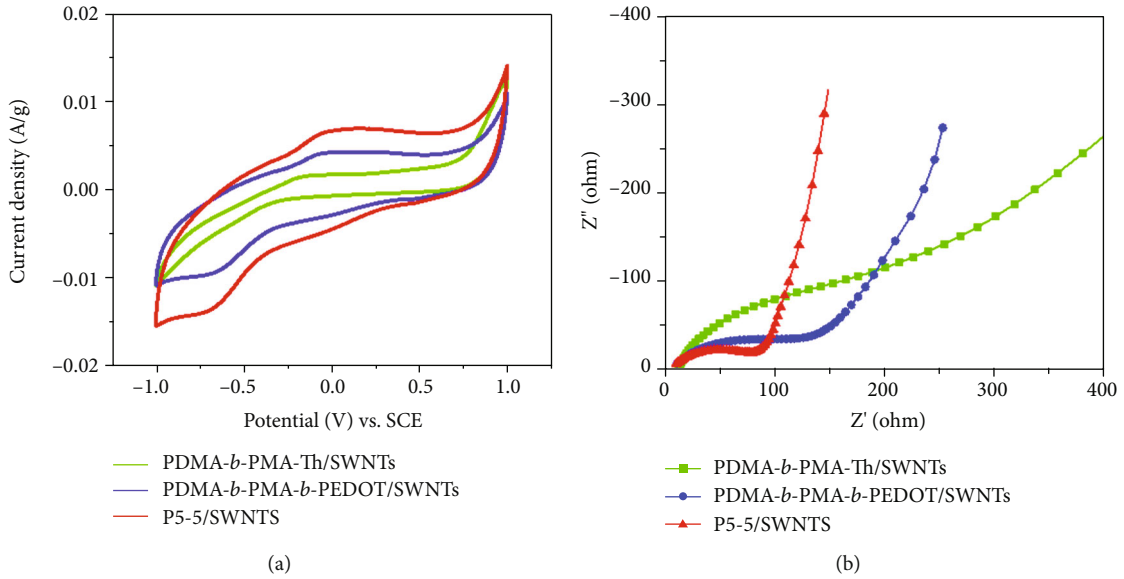

Figure 6: Cyclic voltammograms of the copolymer/SWNT composite at 50 mV/s (a) and electrochemical impedance spectroscopy of the copolymer/SWNT composite (b).

hydrophobic interaction. The R_w value for the P5-5/SWNT composite film was larger than that of PDMA-*b*-PMA-*b*-PEDOT/SWNTs and PDMA-*b*-PMA-Th/SWNTs, which demonstrated good accessibility of the electrolyte ions to the P5-5/SWNT electrode in the participation of robust silsesquioxane cages on the surface. These EIS results supported the CV analyses of the enhanced electrochemical performance of the P5-5/SWNT composite film and also echoed the analyses of UV spectra and TEM; that is, the SQ-based star-shaped copolymer with PEDOT segments could tightly adhere on the surface to stabilize more nanotubes in aqueous solution.

4. Conclusion

In summary, one star-shaped silsesquioxane-polythiophene hybrid modifier (P5-5) for SWNTs was successfully synthesized via a modified interfacial synthesis protocol. The visual sedimentation indicated that the P5-5 showed excellent ability to stabilize SWNTs in aqueous solution, and direct evidences of modifier/SWNT interactions were verified by UV-vis, FTIR, TEM, and TGA, which demonstrated that the amphiphilic hybrid copolymer was much more efficient at modifying SWNTs than its linear analogs. The possible mechanism for elucidating the noncovalent interaction between SWNTs and the star-shaped copolymer was that the silsesquioxane core and conjugated PEDOT chains locally anchored onto the nanotube surface due to their hydrophobicity nature, while the flexible copolymer chains stretched into aqueous solution; in addition, the formation of amphiphilic copolymer aggregations, which is convex over the sidewall surface, sequentially reduced the hydrophobic area for minimizing their contact with water and other tubes and thus provided hydrophilic "buoys" to enhance the solubility of SWNTs in aqueous solution. The electrochemical properties indicated that PEDOT chains and silsesquioxane cages tended to facilitate the charge migration due to the electrochemical activity and functional capability of P5-5.

Data Availability

The data used to support the findings of this study are included within the article.

Conflicts of Interest

The authors declare that they have no conflicts of interest.

Authors' Contributions

Shuxi Gao and Xiaoyong Hu contributed equally to this work.

Acknowledgments

The authors gratefully acknowledge the financial support from the China Postdoctoral Science Foundation (2019M662819) and the Guangdong Academy of Sciences Project of Science and Technology Development (2018GDASCX-1011) and the material support from Professor Kai Xu's group (Guangzhou Institute of Chemistry, Chinese Academy of Sciences).

Supplementary Materials

The only supplied supporting information consists of 14 pages (single column) including 14 figures. It contained the detailed description of the experimental process and some additional results for accurate argument. *(Supplementary Materials)*

References

[1] S. Iijima, "Helical microtubules of graphitic carbon," *Nature*, vol. 354, no. 6348, pp. 56–58, 1991.

[2] R. H. Baughman, A. A. Zakhidov, and W. A. de Heer, "Carbon nanotubes–the route toward applications," *Science*, vol. 297, no. 5582, pp. 787–792, 2002.

[3] M. Yang, V. Koutsos, and M. Zaiser, "Interactions between polymers and carbon nanotubes: a molecular dynamics study," *The Journal of Physical Chemistry B*, vol. 109, no. 20, pp. 10009–10014, 2005.

[4] S. Gao, Z. Yu, K. Xu et al., "Silsesquioxane-cored star amphiphilic polymer as an efficient dispersant for multi-walled carbon nanotubes," *RSC Advances*, vol. 6, no. 36, pp. 30401–30404, 2016.

[5] A. Di Crescenzo, M. Aschi, and A. Fontana, "Toward a better understanding of steric stabilization when using block copolymers as stabilizers of single-walled carbon nanotubes (SWCNTs) aqueous dispersions," *Macromolecules*, vol. 45, no. 19, pp. 8043–8050, 2012.

[6] N. A. Rice and A. Adronov, "Supramolecular interactions of high molecular weight poly (2,7-carbazole) s with single-walled carbon nanotubes," *Macromolecules*, vol. 46, no. 10, pp. 3850–3860, 2013.

[7] A. Habibnejad Korayem, M. R. Barati, G. P. Simon et al., "Transition and stability of copolymer adsorption morphologies on the surface of carbon nanotubes and implications on their dispersion," *Langmuir*, vol. 30, no. 33, pp. 10035–10042, 2014.

[8] K. Y. Cho, Y. S. Yeom, H. Y. Seo et al., "Rational design of multiamphiphilic polymer compatibilizers: versatile solubility and hybridization of noncovalently functionalized CNT nanocomposites," *ACS Applied Materials & Interfaces*, vol. 7, no. 18, pp. 9841–9850, 2015.

[9] P.-C. Ma, N. A. Siddiqui, G. Marom, and J.-K. Kim, "Dispersion and functionalization of carbon nanotubes for polymer-based nanocomposites: a review," *Composites Part A: Applied Science and Manufacturing*, vol. 41, no. 10, pp. 1345–1367, 2010.

[10] H. Abbasi, M. Antunes, and J. I. Velasco, "Recent advances in carbon-based polymer nanocomposites for electromagnetic interference shielding," *Progress in Materials Science*, vol. 103, pp. 319–373, 2019.

[11] A. S. R. Bati, L. Yu, M. Batmunkh, and J. G. Shapter, "Recent Advances in Applications of Sorted Single-Walled Carbon Nanotubes," *Advanced Functional Materials*, vol. 29, no. 30, p. 1902273, 2019.

[12] M. W. Chik, Z. Hussain, M. Zulkefeli et al., "Polymer-wrapped single-walled carbon nanotubes: a transformation toward better applications in healthcare," *Drug Delivery and Translational Research*, vol. 9, no. 2, pp. 578–594, 2019.

[13] K.-t. Lau, C. Gu, and D. Hui, "A critical review on nanotube and nanotube/nanoclay related polymer composite materials," *Composites Part B: Engineering*, vol. 37, no. 6, pp. 425–436, 2006.

[14] A. S. Christensen, T. Kubař, Q. Cui, and M. Elstner, "Semiempirical quantum mechanical methods for noncovalent interactions for chemical and biochemical applications," *Chemical Reviews*, vol. 116, no. 9, pp. 5301–5337, 2016.

[15] Y. Zhou, R. Azumi, and S. Shimada, "A highly durable, stretchable, transparent and conductive carbon nanotube–polymeric acid hybrid film," *Nanoscale*, vol. 11, no. 9, pp. 3804–3813, 2019.

[16] Y.-L. Zhao, N. Ullah, S. Chen, and R.-Q. Zhang, "n $\rightarrow \pi^*$ interaction promoted charge carrier transfer between helical SWNTs and a 4-(1-pyrenyl) phenyl group," *The Journal of Physical Chemistry C*, vol. 123, no. 22, pp. 13976–13982, 2019.

[17] P. Bilalis, D. Katsigiannopoulos, A. Avgeropoulos, and G. Sakellariou, "Non-covalent functionalization of carbon nanotubes with polymers," *RSC Advances*, vol. 4, no. 6, pp. 2911–2934, 2014.

[18] L. V. Sigolaeva, T. V. Bulko, M. S. Kozin et al., "Long-term stable poly(ionic liquid)/MWCNTs inks enable enhanced surface modification for electrooxidative detection and quantification of dsDNA," *Polymer*, vol. 168, pp. 95–103, 2019.

[19] G. Zhang, M. McBride, N. Persson et al., "Versatile interpenetrating polymer network approach to robust stretchable electronic devices," *Chemistry of Materials*, vol. 29, no. 18, pp. 7645–7652, 2017.

[20] Z.-H. Jin, Y.-L. Liu, J.-J. Chen, S.-L. Cai, J.-Q. Xu, and W.-H. Huang, "Conductive polymer-coated carbon nanotubes to construct stretchable and transparent electrochemical sensors," *Analytical Chemistry*, vol. 89, no. 3, pp. 2032–2038, 2017.

[21] Y. Huang, Y. Wang, L. Gao, X. He, P. Liu, and C. Liu, "Characterization of stretchable SWCNTs/Lycra fabric electrode with dyeing process," *Journal of Materials Science: Materials in Electronics*, vol. 28, no. 5, pp. 4279–4287, 2017.

[22] L. Yu, C. Shearer, and J. Shapter, "Recent development of carbon nanotube transparent conductive films," *Chemical Reviews*, vol. 116, no. 22, pp. 13413–13453, 2016.

[23] I. A. Kinloch, J. Suhr, J. Lou, R. J. Young, and P. M. Ajayan, "Composites with carbon nanotubes and graphene: an outlook," *Science*, vol. 362, no. 6414, pp. 547–553, 2018.

[24] S. Gao, K. Xu, X. Gui, L. Sun, and L. Liu, "Synthesis of soluble silsesquioxane–polythiophene hybrid copolymers with a controlled morphology," *ACS Applied Polymer Materials*, vol. 1, no. 3, pp. 437–451, 2019.

[25] J. Peng, K. Xu, H. Cai et al., "Can an intact and crystalline octakis(methacryloxypropyl) silsesquioxane be prepared by hydrolysis-condensation of a trimethoxysilane precursor?," *RSC Advances*, vol. 4, no. 14, pp. 7124–7131, 2014.

[26] H. Willcock and R. K. O'Reilly, "End group removal and modification of RAFT polymers," *Polymer Chemistry*, vol. 1, no. 2, pp. 149–157, 2010.

[27] J. F. Ponder Jr., A. M. Österholm, and J. R. Reynolds, "Designing a soluble PEDOT analogue without surfactants or dispersants," *Macromolecules*, vol. 49, no. 6, pp. 2106–2111, 2016.

[28] Z. Iatridi and C. Tsitsilianis, "pH responsive MWCNT–star terpolymer nanohybrids," *Soft Matter*, vol. 9, no. 1, pp. 185–193, 2013.

[29] S. Majeed, V. Filiz, S. Shishatskiy, J. Wind, C. Abetz, and V. Abetz, "Pyrene-POSS nanohybrid as a dispersant for carbon nanotubes in solvents of various polarities: its synthesis and application in the preparation of a composite membrane," *Nanoscale Research Letters*, vol. 7, no. 1, p. 296, 2012.

[30] H. Zhang, T.-T. Lu, W.-Y. Lai et al., "Pyrene-cored starburst oligofluorenes with diphenylamine end-cappers: design, synthesis, stabilized optical gain, and lasing properties," *The Journal of Physical Chemistry C*, vol. 121, no. 49, pp. 27569–27579, 2017.

[31] T. Goda, M. Toya, A. Matsumoto, and Y. Miyahara, "Poly(3,4-ethylenedioxythiophene) bearing phosphorylcholine groups for metal-free, antibody-free, and low-impedance biosensors specific for C-reactive protein," *ACS Applied Materials & Interfaces*, vol. 7, no. 49, pp. 27440–27448, 2015.

[32] C. Wei, W. Zhang, Y. Zhou et al., "High-performance ternary π-conjugated copolymers containing diarylethylene units: synthesis, properties, and study of substituent effects on molecular aggregation and charge transport characteristics," *Journal of Materials Chemistry C*, vol. 7, no. 2, pp. 362–370, 2019.

[33] Z. Zhou, C. Gu, C. Chen, P. Zhao, Y. Xie, and J. Fei, "An ultrasensitive electrochemical sensor for quercetin based on 1-pyrenebutyrate functionalized reduced oxide graphene /mercapto-β- cyclodextrin /Au nanoparticles composite film," *Sensors and Actuators B: Chemical*, vol. 288, pp. 88–95, 2019.

[34] P. Zhao, M. Ni, C. Chen et al., "Stimuli-enabled switch-like paracetamol electrochemical sensor based on thermosensitive polymer and MWCNTs-GQDs composite nanomaterial," *Nanoscale*, vol. 11, no. 15, pp. 7394–7403, 2019.

Hindawi
International Journal of Polymer Science
Volume 2020, Article ID 4953652, 8 pages
https://doi.org/10.1155/2020/4953652

Research Article

Morphological Evolvement of Carbon Nanotubes Synthesized by Using Conducting Polymer Nanofibers

Yang Liu[1], **John H. Xin**[2], **Xinyu Zhang**[3] **and Chao Zhang**[1]

[1]*Department of Biomedical Engineering, Sun Yat-sen University, Guangzhou, China 510006*
[2]*Institute of Textiles and Clothing, The Hong Kong Polytechnic University, Hung Hom, Hong Kong, China*
[3]*Department of Chemical Engineering, Auburn University, Auburn, Alabama, USA 36849*

Correspondence should be addressed to Yang Liu; liuyang56@mail.sysu.edu.cn

Received 20 September 2019; Revised 12 December 2019; Accepted 18 February 2020; Published 2 March 2020

Academic Editor: Christopher Batich

Carbon nanotubes were synthesized by using a nanostructured conducting polymer—the polypyrrole nanofiber via microwave radiation. The radiation time was set to be 30, 60, and 90 seconds, respectively. The morphological evolvements of the as-synthesized carbon nanotubes with increased radiation time (e.g., shape, diameter, wall structure, and catalyst size) were carefully investigated, and the possible growth mode was discussed in detail. It was found that the growth mode of the carbon nanotubes synthesized from the conducting polymer substrate under microwave radiation was complex and cannot be simply interpreted by either a "tip" or "base" growth model. A new growth mode of the "liquifying cascade growth" was observed for the as-synthesized carbon nanotubes, as their growth was directed by a series of liquified iron nanoparticles with sequentially decreasing sizes, similar to the cascade of liquid droplets. And it could provide useful insights for the morphological and structural designs of the carbon nanotubes prepared by related microwave-based methods.

1. Introduction

Carbon nanotubes (CNTs) represent a special one-dimensional allotrope of graphite with distinct thermal, electrical, mechanical, and chemical properties [1]. Currently, CNTs are majorly synthesized by thermal techniques such as chemical vapor deposition (CVD), arc discharge (AC), and laser ablation (LA) [2]. However, the CVD techniques majorly use the gasified hydrocarbons as the precursor while AC and LA use the decomposed carbonaceous species generated from high-energy sources as precursors. Recently, extensive research efforts have been made to develop the synthesis technique of CNTs based on conducting polymers [3–10]. Due to their excellent microwave absorption properties, conducting polymers, e.g., polypyrrole (Ppy), can be used as the substrate to grow CNTs in a domestic microwave oven. Upon microwave radiation, the conducting polymer quickly absorbs the electromagnetic waves and elevates the reaction temperature to several hundreds of degrees Celsius. This triggers the decomposition of ferrocene to generate iron (Fe) nanoparticles as the catalyst and gaseous hydrocarbons as the carbon source to initiate the CNT growth. Due to the highly efficient heating of the conducting polymer, the whole CNT growth process can be completed within tens of seconds [3, 6, 9, 10]. Compared to CVD, AC, and LA techniques, the conducting polymer-based microwave technique may attain the characteristics of simple instrumentation, easy-processing, and very fast growth. It can also be used to grow CNT brushes on the surface of different materials, e.g., carbon fiber fabrics, MXene, Kevlar fibers, and poly(lactic-co-glycolic acid) particles to obtain CNT-based hierarchical composites with enhanced electrochemical, mechanical, and bioimaging properties [3, 9, 11, 12]. Even though the growth of CNTs by using the conducting polymer-based microwave technique is simple and fast, currently, there are very few reports on the morphological study of the as-obtained CNTs. And the mechanisms involved in the microwave growth process have not been comprehensively studied and are still unclear.

The morphological control of CNTs is very important because the size and shape of CNTs can significantly affect their properties and functions [13]. For example, the bamboo-shaped CNTs were reported to have high energy-

storage performance such as high-discharge capacities, high rate capabilities, and low potential gaps, as they were used as the electrode catalysts of the Li-CO_2 batteries [14]. On the other hand, it was also reported that the bamboo-shaped CNTs showed exponential decrease of scission length and low tensile strengths during ultrasonication [15]. Coiled CNT forests also showed strongly nonlinear dependence on displacement which was found to be fundamentally different from the response of a straight CNT forest, under high-strain rate deformation of a drop-ball test [16]. The morphology of the as-synthesized CNTs is intrinsically clung to the growth modes. Currently, either a "tip growth" or "base growth" model has been proposed to the CNTs synthesized by using the conducting polymer-based microwave techniques, deducing from the location of the catalyst nanoparticles (NPs) [3, 6]. However, these assumptions are rather empirical and insufficient to describe the internal growth modes of CNTs synthesized by the conducting polymer microwave technique according to our experimental observations.

Herein, we carefully investigate the growth mode of the CNTs synthesized by using conducting polymer, i.e., polypyrrole nanofibers (Ppy NFs), under the microwave radiation of a domestic microwave oven. The radiation time was gradually increased to study the morphological evolvement of the CNTs in the process. Compared to the nonnanostructured conducting polymers that are widely used to grow CNTs, the Ppy NFs would have stronger microwave absorbing properties due to their one-dimensional (1D) nanostructure and high surface area [17]. The correlation between the CNT morphology and the morphology of the catalyst NPs is also discussed in detail. And a new possible growth mode of the CNTs synthesized by conducting polymer-based microwave techniques is proposed.

2. Experimental

2.1. Synthesis of CNTs by Using Ppy NFs and Ferrocene. Ppy NFs were synthesized by a modified "seeding approach" [17]. Briefly speaking, 1 mL pyrrole (Alfa Aesar, 98%) was added into 60 mL 1 M HCl and magnetically stirred for 20 minutes (min). Subsequently, 1 mL vanadium pentoxide (V_2O_5) nanofiber sol-gel was injected into the dispersion quickly by using a 1 mL syringe. The transparent dispersion turned light green immediately, and Ppy NFs were starting to precipitate out of the dispersion as V_2O_5 was added. After 30 seconds (s), 1.09 g initiator ammonium persulfate (Alfa Aesar, 98%) was added to trigger the polymerization process. The polymerization was proceeded for another 1 hour under magnetic stirring. After polymerization, the black precipitation was suction filtered and washed with copious amounts of 1 M HCl and acetone to remove the impurities. The as-obtained Ppy NFs were dried in an 80°C oven overnight before further usage.

70 mg of Ppy NFs and 70 mg ferrocene (Alfa Aesar, 99%) were mechanically mixed using an agate mortar and then transferred to a 20 mL quartz-glass vial. The black powder of Ppy NF was thoroughly mixed with the yellowish ferrocene, and the final mixture appeared as homogeneous black powders. The glass vial was then placed into a domestic microwave oven (Panasonic Inverter 1000) and heated at 1000 W power for different durations, i.e., 30 s, 60 s, and 90 s. As the microwave radiation was applied, the black mixture was quickly heated up and turned red, which was similar to the color of hot iron, due to the intensive absorption of microwave by the Ppy NFs. At the same time, the temperature of the mixture was quickly risen to several hundreds of degrees Celsius and triggered the decomposition of ferrocene, generating high density of gaseous carbonaceous species floating inside the glass vial and covering its inner walls. As the microwave process continued, intensive microplasmas were generated near the surface of the mixture, which interacted with the gaseous species to give shining sparks inside the glass vial. Simultaneously, high pressure was generated by the hot gas inside the vial, and the shape of the quartz glass was also slightly deformed. The microwave heating process was automatically stopped when the preset time was depleted. The glass vial was then cooled in ambient condition, and the product was subsequently collected and purified by washing with copious amounts of toluene and water to remove the residues of precursors.

2.2. Characterizations of the as-Synthesized CNTs. The morphologies of the as-synthesized CNTs were characterized by a scanning electron microscope (SEM, JEOL JXA-8600). The tube-wall and graphitic structures of the CNTs were characterized by a transmission electron microscope (TEM, JEOL JEM-2100F) equipped with an energy dispersive X-ray detector (EDX, Oxford Instruments INCA X-Max). The TEM sample was prepared by adding 3 mg of the as-synthesized CNTs in 5 mL de-ionized water, which was subsequently bath-sonicated for 20 min to form a homogeneous dispersion. One or two drops from the dispersion was then casted on a TEM copper grid by using a glass pipette. The elemental composition and crystalline structure of the catalysts were analyzed by EDX and selected area electron diffraction (SAED).

The size distributions of the as-synthesized CNTs were measured by analyzing the corresponding SEM and TEM images using the ImageJ software. For each set of the samples, at least 50 different CNTs were counted and analyzed to calculate the values of average diameter and standard deviation, respectively.

3. Results and Discussion

The representative SEM images of the CNTs synthesized by using Ppy nanofibers and ferrocene under different microwave radiation time are shown in Figure 1. Apparently, thin and curved CNTs are obtained from the time of 30 s, as shown in Figures 1(a) and 1(b). The CNTs are radially grown outward from many granulated micron-sized particulates, resembling the structure of a sea urchin (Figure 1(a)). As the microwave time increases to 60 s, significant changes in the morphology can be observed for the as-obtained CNTs, compared to the 30 s situation. In this case, thicker and straighter CNTs are grown from the granulated substrates, and the radial growth is disturbed (Figures 1(c) and 1(d)). The as-grown CNTs tend to randomly entangle with each

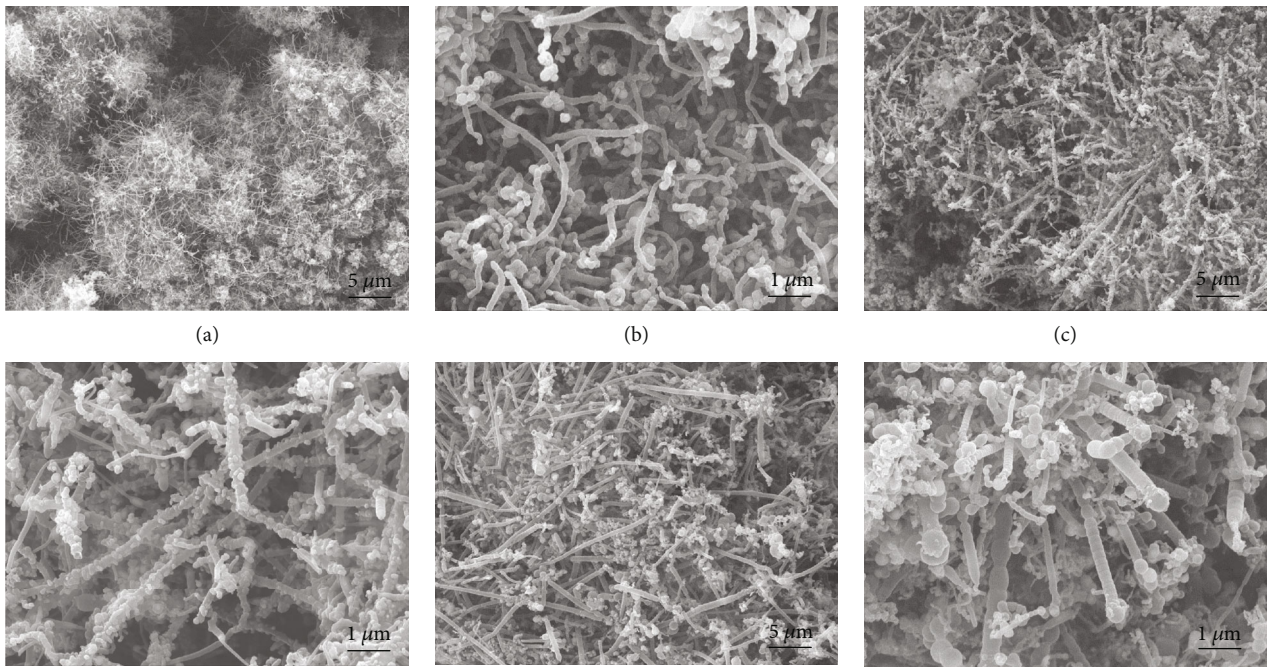

Figure 1: SEM images of CNTs synthesized by Ppy NFs and ferrocene under microwave radiation for 30 s (a, b), 60 s (c, d), and 90 s (e, f).

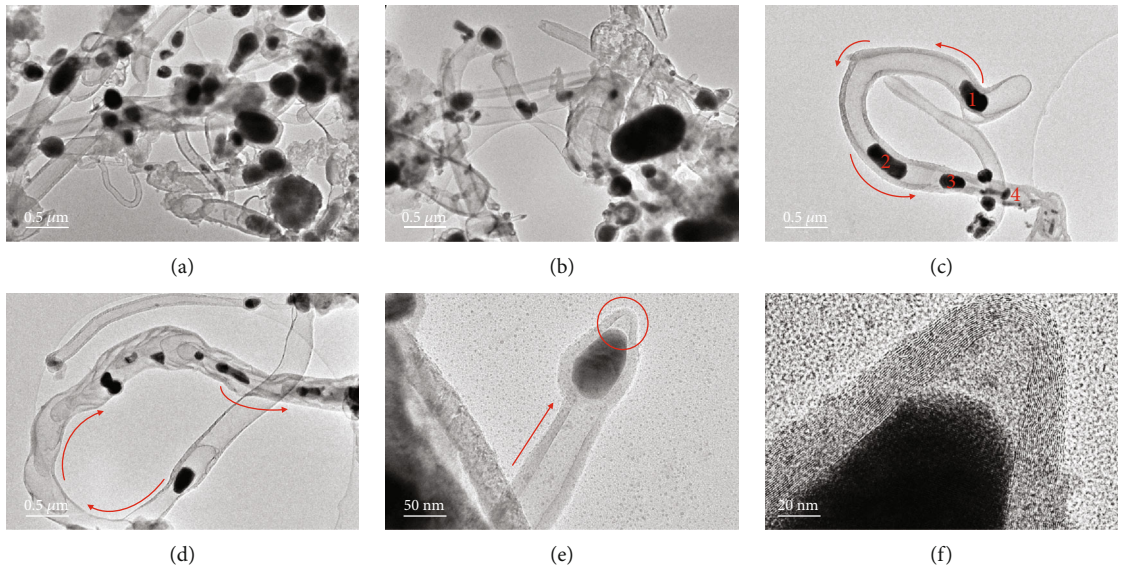

Figure 2: (a, b) TEM images of the CNTs synthesized by 30 s microwave time and protruded catalyst Fe NPs are observed to direct the CNT growth. (c, d) TEM images showing the cascade growth process of the CNTs; the catalyst Fe NPs are protruded towards the growth direction and lifted to direct the growth from the parent NP, forming a discontinuous cascade of NPs. The growth direction is marked with red arrows. (e) TEM image showing a CNT as the growth process is terminated. A catalyst Fe NP encapsulated in carbon shells can be observed at the tip of the CNT. The carbon shells are composed of orderly stacking graphene layers as shown in (f).

other, forming porous networks. Upon further increasing the microwave time to 90 s, thick and straight CNTs are found to grow from the granulated substrates at various angles, while a portion of thin and curved CNTs are also observed to exist alongside with them (Figure 1(e)). The other portion of the thick and straight CNTs obtained from 90 s show a characteristic bamboo-shaped morphology, as the side walls of the CNTs are apparently segmented into periodic nanoscale compartments (Figure 1(f)). The average diameters of the CNTs obtained from 30 s are calculated to be 145.8 nm, with a standard deviation of 18.7 nm. And the calculated average diameters of the CNTs obtained from 60 s and 90 s are 268.8 nm and 356.8 nm, with standard deviations of 56.8 nm and 141.2 nm, respectively.

The TEM images of CNTs obtained from 30 s are shown in Figure 2. From Figure 2(a), it can be observed that the tube

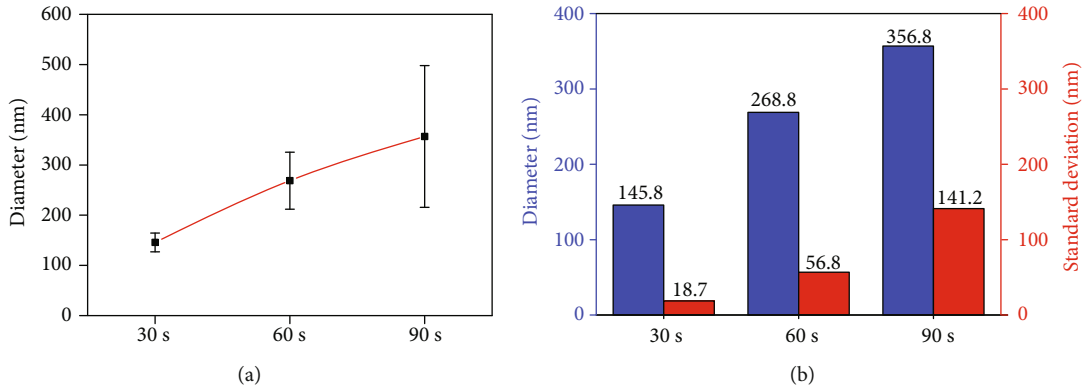

Figure 3: (a) Plotted graph showing the correlation between the average CNT diameters and microwave time; the standard deviations are plotted as the error bars. (b) Columns showing the direct comparison of the average diameters and corresponding standard deviations of the CNTs synthesized from 30 s, 60 s, and 90 s.

walls of the as-obtained CNTs are generally smooth, composing of continuous stacking graphene layers with structural homogeneity. Catalyst NPs can be observed inside the hollow cores of the CNTs, and they are identified to be the polycrystalline Fe NPs according to the EDX (Figure S1) and the SAED analysis (Figure S2). The shapes of the Fe NPs are ellipsoid, spherical, and ellipsoid with one protruded end. The average diameters of the Fe NPs are measured to be 136.6 nm with a standard deviation of 51.9 nm. And the average outer diameters of the corresponding CNTs are measured to be 139.9 nm, indicating a strong correlation between the NP diameter and the CNT diameter. The CNTs are found to preferentially nucleate and grow on smaller Fe NPs at the early stage, while larger NPs (diameters > 200 nm) show a slower CNT growth kinetics in terms of the length and thickness of the forming tube walls. A few large Fe NPs with diameters between 260 and 440 nm also can be observed. These large Fe NPs are partially covered by multiple layers of graphene sheets with one end protrudes and points towards the propagating CNT growth direction (Figures 2(a) and 2(b)). It is speculated that the Fe NPs are partially liquified to form the protruding ends during the growth process. The liquified portion of the NPs then serve as the active catalytic center to direct the CNT growth. As the carbon atoms continuous diffuse and precipitate out from the liquified NPs, the protruding portion of the Fe NPs may detach from the original NP and lift off. The CNTs then continue to grow from the lifting liquified Fe NPs, producing smooth tube walls whose inner diameters are identical to the minor axis of the liquified NPs (Figure 2(c)). At this time, the lifting liquified NPs may act as the active tips to direct the CNT growth. However, the lifted liquified NPs may receive fewer thermal energies as they move away from the heating substrates, and the lifting process as a whole is stopped due to the partial cooling and solidifying of the NPs. In this case, a smaller liquified NP may again protrude from the parent NP and lifted to direct the CNT growth, repeating the previous growth process. The growing of CNTs would be stopped if the lifted NPs become too small or solidified, as shown in Figures 2(c) and 2(d). Either tip or base growth mode has been suggested for the CNTs synthesized from ferrocene under microwave radiation, using conducting polymers or graphite as the heating substrate. This is due to the fact that the Fe NPs can be observed to distribute along the major tube axis of the as-obtained CNTs, e.g., at the tips, at the bottoms, and in the middle. This phenomenon actually reveals the liquifying cascade growth mode of the CNTs under microwave which cannot be simply interpreted as tip or base growth, because the Fe NPs in the liquid state may solidify and split into multiple smaller NPs to direct the tube growth. As the liquified Fe NPs solidify, thick carbon shells with orderly stacking graphene layers are formed along the surface profile of the NPs, as shown in Figures 2(e) and 2(f). The tip of the Fe NP is capped with closed carbon shells, and no further growth can be initiated, indicating the termination of the growth process (Figure 2(f)). Stacking faults and misalignments can be observed in the tube wall structures of the CNTs obtained from 30 s (Figure S3), indicating the reduced degree of graphitization in short microwave time.

The changes in the diameters of the CNTs synthesized by using different microwave time were firstly analyzed through the SEM images. The quasilinear increase in the average diameters with prolonged microwave time of the as-obtained CNTs indicates their growth process is kinetically controlled (Figure 3(a)). The rate determine step is speculated to be the decomposition of ferrocene. The standard deviations to the average diameters significantly increase with prolonged microwave time, indicating the CNTs synthesized from shorter time would have a more uniform diameter distribution and longer microwave time may generate a wide-range diameter distribution for the CNTs that confers significant differences in diameters between the individual CNTs (Figure 3(b)). However, the increase of CNT diameters, significantly widened diameter distributions, and the emerging of CNTs with extremely large diameters as the microwave time is prolonged all in total reflect the change of the growth kinetics as it proceeds. Indeed, the total morphological evolvement of the CNTs is directly controlled by the growth kinetics and can be simply modulated by tuning the microwave time. On the other hand, the growth kinetics, including carbon diffusion, metal-carbon interaction, and carbon wall structure formation, are strongly related to the dynamic crystalline structures of the metal

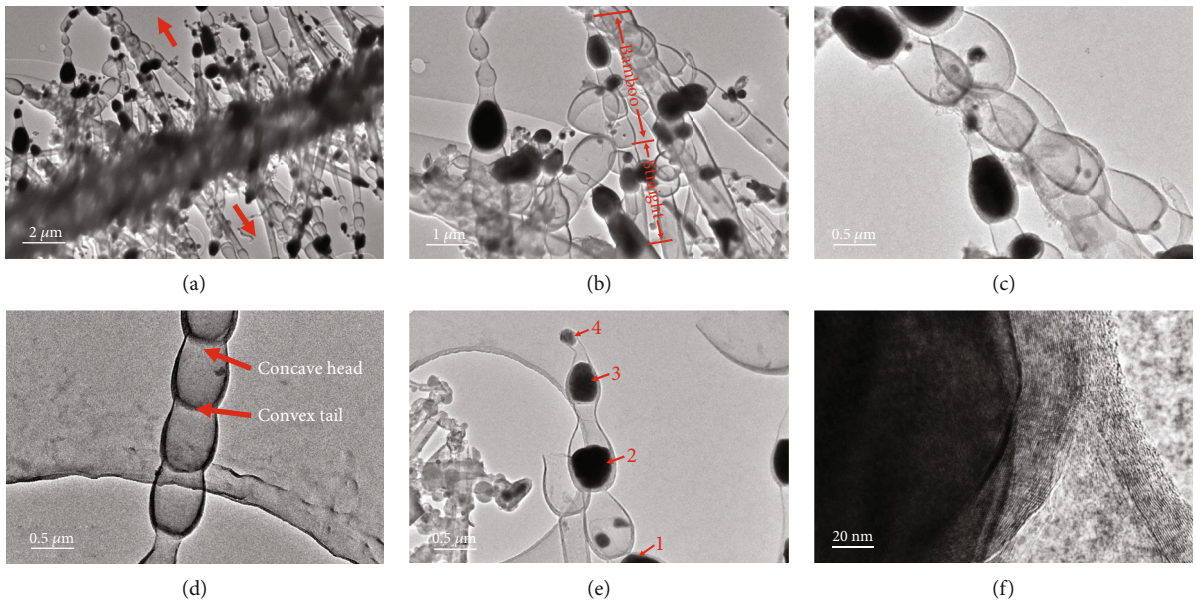

Figure 4: (a, b) TEM images of the bamboo-shaped CNTs synthesized by 60 s microwave time. The bamboo-shaped CNTs are found to grow in opposite directions from the sheet-like substrate in (a), and the growth direction is marked with red arrows. The bamboo-shaped CNTs are found to compose of one straight part with smooth and continuous tube wall and the other part with bamboo-like segmented tube walls, as shown in (b). (c, d) TEM images showing the magnified view of the bamboo-shaped CNTs. The catalyst Fe NPs can be observed at the tips of the CNTs, as shown in (c). And the growth direction of the bamboo-shaped CNTs is identified to be from the convex tails to the concave heads, as shown in (d). (e) Liquifying cascade growth mode similar to the 30 s situation is also observed for the 60 s CNTs. The cascading catalyst NPs with reducing sizes are numbered with arithmetic orders. (f) HRTEM image showing the well-stacking graphitized tube walls of the bamboo-shaped CNTs.

NPs that are acting as the catalysts. By investigating the size and shape changes of the metal NPs during the CNTs' growth and the influences of these changes on the CNTs' morphologies, we can gain useful insights on the detail growth processes, growth modes, and microstructural formation of the as-grown CNTs.

As the microwave time increases to 60 s, significant morphological changes are observed for the as-obtained CNTs. Both CNTs with smooth and continuous tube walls (Figure S4) and CNTs with bamboo-like wall structures (Figure 4(a)) are found to coexist in the products. The average diameters of the CNTs measured from the TEM images are 246 nm, and this value is considered to be consistent with the SEM analysis. The bamboo-like CNTs are observed to grow from the same sheet-like substrate (Figure 4(a)). The CNTs are grown perpendicularly to the substrate in two opposite directions at different angles. The catalyst Fe NPs are found to intensively exist inside the tube cores, lifted towards the tips, forming cascade NPs of decreasing sizes within single bamboo-like CNTs, which are similar to the liquid droplet cascades. By carefully examining the bamboo-like CNTs, it is found that they are generally composed of a smooth and straight tube portion connecting to a bamboo-shaped portion (Figure 4(b)). This abrupt change of the tube structure can be possibly attributed to the phase transition of the catalyst Fe NPs. It has been reported that Ni catalyst NPs underwent a reversible phase change from the liquified state to the solidified state in the temperature range from 800 to 700°C, resulting in a structure change of the CNT tube walls from straight to cup-stack [18]. It has also been reported that the as-grown CNTs would obtain a tube wall structure reproducing the shape of the active catalyst NPs [19]. Therefore, in the first place, the liquified Fe NPs may extrude from the heating substrate and direct the CNT growth. At this stage, CNTs with smooth and continuous tube walls can be formed. Due to the unique heating mechanism of microwave, the heats are generated by the microwave absorbing substrates, i.e., Ppy nanofiber. As the catalyst Fe NPs move away from the substrate, they receive fewer thermal energies and become reluctant to maintain the liquid-like form. The slow cooling of the Fe NPs results in the gradual shrinkage of their shapes from elongated liquified states to solidified spherical states, and it is measured to happen when the NPs are 0.89-3.17 μm distant from the substrate, with an average distance of $1.81 \pm 0.54\,\mu$m, according to the TEM images. During the shrinkage, the NPs may still acquire the partial liquified state and mobile to direct the CNT growth until completely cooling. Therefore, a general trend that can be observed for the growth of bamboo-like CNTs is the length and size of the individual bamboo-like compartments decrease as the tube length increases, coincided with the phase change of the catalyst Fe NPs. The bamboo-like CNTs are formed by the stacking of several cup-shaped compartments with convex tails and concave heads, and the catalyst Fe NPs can be found around the tips of the CNTs (Figure 4(c)). By identifying the locations of the convex tails and the concave heads, the growth direction of the bamboo-like CNTs can be manifested (Figure 4(d)). The CNTs obtained from 60 s share the same growth mode with the 30 s, and the sequence

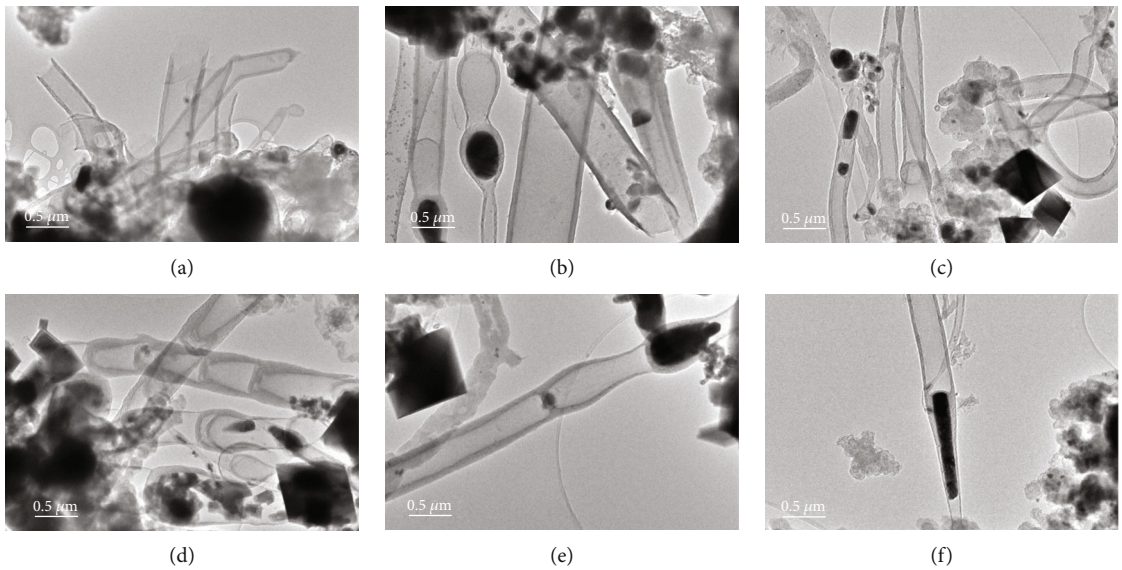

Figure 5: Different morphologies can be observed for the CNTs synthesized by 90 s microwave time, such as straight tubes with continuous tube walls (a), bamboo-shaped tubes with segmented tube walls (b), curved tubes with continuous tube walls (c), and cup-stack tubes (d). A few large rhombohedral and rectangular NPs can be observed in (c), (d), and (e), indicating substantial Ostwald ripening of the catalysts. Protruding (e) and liquid-shaped (f) catalyst Fe NPs can be observed at the tips of the as-obtained CNTs, indicating the same growth mode with the 30 s and 60 s processes.

of the cascading NPs can be clearly observed around their tips (Figure 4(e)). The 60 s CNTs exhibit well-graphitized wall structure with a lattice spacing of 0.34 nm without stacking faults both on and parallel to the catalyst surface, indicating the growth time is sufficient to achieve a higher degree of graphitization (Figure 4(f) and Figure S5).

As the microwave time increases to 90 s, the as-obtained CNTs show diverse morphologies including straight, curved, bamboo-shaped, and cup-stack (Figures 5(a)–5(d)). The average diameter of the CNTs obtained from the TEM analysis is calculated to be 324.9 nm, close to the SEM analysis result. The as-obtained CNTs also showed orderly stacking graphitic shells, with larger shell thickness than the 60 s tubes (Figure S6). However, the substantial inhomogeneity observed in the morphologies for the 90 s CNTs can be possibly attributed to the inhomogeneous nucleation and growth processes of the catalyst Fe NPs which produces NPs with a wide range of size distribution to catalyze the CNT growth. It has been reported that the size of the catalyst NPs would continue growing during the CNT growth process by both surface diffusion and the Ostwald ripening process [20]. The surface diffusion of the catalyst atoms onto the same catalyst NPs may result in the size increment of the NPs and eventually deactivate the catalyst NPs to grow CNTs [21]. On the other hand, the Ostwald ripening process would result in the continuous growth of the large catalyst NPs by consuming the smaller ones. The combination of these two effects may give rise to significant differences in size between the large and small catalyst NPs. Interestingly, remarkable differences in size can be observed for the catalyst Fe NPs during the 90 s growth. The large Fe NPs with sizes from 190 to 513 nm and small NPs with sizes from 74 to 160 nm are found to coexist in the core regions of the CNTs (Figures 5(b)–5(e)). A few large NPs with rhombohedral and rectangular shapes can also be observed around the CNT bundles (Figures 5(c)–5(e)). There are no graphitic shells covered on the surface of these large NPs, indicating that they are inert to catalyze the CNT growth. Interestingly, a rhombohedral NP is observed at the tip end of a bamboo-shaped CNT, and the smaller NPs in the compartment of the CNT are merging towards the rhombohedral NP, which can be taken as an indication for the Ostwald ripening process (Figure 5(d)). Besides the remarkable Ostwald ripening phenomenon on the catalyst NPs, the CNTs obtained from 90 s show a similar growth mode to the 30 s and 60 s situations, as the liquifying catalyst Fe NPs elongated and elevated from the parent NPs to direct the CNT growth and subsequently form a liquifying cascade of smaller NPs to continue the growth process (Figures 5(e) and 5(f)). Eventually, the growth process would be stopped as the small NPs were deactivated by the surface-covered graphitic shells (Figure S7).

4. Conclusions

In this article, we detailedly investigated the morphological evolvement of the CNTs synthesized by using Ppy nanofibers and ferrocene under microwave radiation. The reaction kinetics of the growth process were elaborated by analyzing the morphologies of CNTs and catalyst Fe NPs obtained from increased microwave time, i.e., 30 s, 60 s, and 90 s. The diameters of CNTs and their degrees of graphitization were found to simultaneously increased with prolonged microwave time from 30 s to 90 s. A strong correlation was also found between the diameters of the CNTs and sizes of the catalyst NPs. By carefully analyzing the TEM images of the catalyst NPs inside the tubes, a new liquifying cascade growth mode was proposed for the as-obtained CNTs. Due to the

unique heating mechanism of microwave, the liquified catalyst NPs would receive fewer thermal energies as they were elevating from the substrates (heat source) and became gradually solidified. During this stage, a morphological transformation from smooth and straight tubes to bamboo-shaped tubes can be observed. However, the growth process of CNTs was continued until the cascade liquified NPs became fully covered by the graphitic shells or too small to catalyze the CNT formation. The Ostwald ripening of the catalyst NPs was found to become significant as the microwave time was increased to 90 s. The remarkable difference in size between the large and small NPs and a wide-range size distribution of the catalyst NPs lead to a highly divergent diameter distribution of the as-obtained CNTs, from approximately 180 nm to 740 nm, after the 90 s microwave process. A few rhombohedral NPs with sizes from around 200 nm to 480 nm were discovered near the tips of the CNTs. These NPs were inert for catalyzing the CNT growth, and it was speculated that they were composed of trigonal hematite crystals according to their shapes.

To further improve the morphological homogeneity of the CNTs synthesized by conducting polymers and ferrocene under microwave, a more homogeneous heating mechanism may need to be implemented to eliminate the thermal gradient near the surface of the substrate and help the NPs maintain their liquified states, e.g., additional microwave absorbing materials like carbon fibers can be introduced on the substrate's surface. On the other hand, the Ostwald ripening process may also need to be suppressed during the growth. To achieve this goal, the microwave synthesis process can be conducted in more reducing environment with the addition of reducing agents such as hydrogen gas.

Data Availability

The data used to support the findings of this study are included within the article and the supporting information files.

Conflicts of Interest

The authors declare no conflict of interests.

Acknowledgments

The financial supports from Sun Yat-sen University, National Natural Science Foundation of China (81801851), Guangdong Science and Technology Department (2018A030310075), and China Postdoctoral Science Foundation (2018M633230) were gratefully acknowledged.

Supplementary Materials

The supporting information file contains the experimental results, including the transmission electron microscopy (TEM) images, high-resolution TEM images (HRTEM), energy-dispersive X-ray (EDX) spectrum, and selected-area electron diffraction (SAED) pattern, to support the discussions in the manuscript. Figure S1: EDX spectrum of the catalyst nanoparticle observed inside the core of the as-obtained CNTs; the elemental composition of the nanoparticle was identified to be Fe. Figure S2: SAED pattern of a catalyst Fe NP encapsulated at the tip of a CNT. The interpretation of pattern indicated the NP was polycrystalline. Figure S3: (a, c) TEM and (b, d) HRTEM images of the CNTs synthesized by 30 s microwave time. The representative stacking faults are marked with blue arrows. Figure S4: (a–d) TEM images of the CNTs with smooth and continuous tube walls synthesized by 60 s microwave time. Figure S5: (a, c, e) TEM and (b, d, f) HRTEM images of the CNTs synthesized by 60 s microwave time. A lattice spacing of 0.34 nm can be observed for the graphitic tube walls. Figure S6: (a, c, e) TEM and the corresponding (b, d, f) HRTEM images of the CNTs synthesized by 120 s microwave time. Figure S7: HRTEM image of a Fe catalyst nanoparticle encapsulated by graphitic shells. *(Supplementary Materials)*

References

[1] Y. R. Poudel and W. Li, "Synthesis, properties, and applications of carbon nanotubes filled with foreign materials: a review," *Materials Today Physics*, vol. 7, pp. 7–34, 2018.

[2] G. D. Nessim, "Properties, synthesis, and growth mechanisms of carbon nanotubes with special focus on thermal chemical vapor deposition," *Nanoscale*, vol. 2, no. 8, pp. 1306–1323, 2010.

[3] Z. Liu, J. Wang, V. Kushvaha et al., "Pop-tube approach for ultrafast carbon nanotube growth," *Chemical Communications*, vol. 47, no. 35, pp. 9912–9914, 2011.

[4] S. H. Bae, K. Karthikeyan, Y. S. Lee, and I. K. Oh, "Microwave self-assembly of 3D graphene-carbon nanotube-nickel nanostructure for high capacity anode material in lithium ion battery," *Carbon*, vol. 64, pp. 527–536, 2013.

[5] V. Sridhar, I. Lee, H. H. Chun, and H. Park, "Microwave synthesis of nitrogen-doped carbon nanotubes anchored on graphene substrates," *Carbon*, vol. 87, pp. 186–192, 2015.

[6] R. Bajpai and H. D. Wagner, "Fast growth of carbon nanotubes using a microwave oven," *Carbon*, vol. 82, pp. 327–336, 2015.

[7] S. K. Park, K. Choi, S. H. Lee, I. K. Oh, S. Park, and H. S. Park, "CNT branching of three-dimensional steam-activated graphene hybrid frameworks for excellent rate and cyclic capabilities to store lithium ions," *Carbon*, vol. 116, pp. 500–509, 2017.

[8] R. Kumar, R. K. Singh, D. P. Singh et al., "Synthesis of self-assembled and hierarchical palladium-CNTs-reduced graphene oxide composites for enhanced field emission properties," *Materials & Design*, vol. 122, pp. 110–117, 2017.

[9] W. Zheng, P. Zhang, J. Chen, W. B. Tian, Y. M. Zhang, and Z. M. Sun, "In situsynthesis of CNTs@Ti3C2hybrid structures by microwave irradiation for high-performance anodes in lithium ion batteries," *Journal of Materials Chemistry A*, vol. 6, no. 8, pp. 3543–3551, 2018.

[10] Y. Liu, X. Zhang, S. Poyraz, C. Zhang, and J. H. Xin, "One-step synthesis of multifunctional zinc-iron-oxide hybrid carbon nanowires by chemical fusion for supercapacitors and interfacial water marbles," *ChemNanoMat*, vol. 4, no. 6, pp. 546–556, 2018.

[11] A. Hazarika, B. K. Deka, D. Y. Kim, K. Kong, Y. B. Park, and H. W. Park, "Microwave-synthesized freestanding iron-carbon nanotubes on polyester composites of woven Kevlar fibre and silver nanoparticle-decorated graphene," *Scientific Reports*, vol. 7, no. 1, 2017.

[12] H. Xie, S. Poyraz, M. Thu et al., "Microwave-assisted fabrication of carbon nanotubes decorated polymeric nano-medical platforms for simultaneous drug delivery and magnetic resonance imaging," *RSC Advances*, vol. 4, no. 11, p. 5649, 2014.

[13] M. Zhang and J. Li, "Carbon nanotube in different shapes," *Materials Today*, vol. 12, no. 6, pp. 12–18, 2009.

[14] X. Li, J. Zhou, J. Zhang et al., "Bamboo-like nitrogen-doped carbon nanotube forests as durable metal-free catalysts for self-powered flexible Li–CO2Batteries," *Advanced Materials*, vol. 31, no. 39, article 1903852, 2019.

[15] J. W. Jang, C. E. Lee, and C. J. Lee, "Exponential decrease of scission length and low tensile strength of bamboo- shaped multi-walled carbon nanotubes under ultrasonication," *Current Applied Physics*, vol. 17, no. 4, pp. 507–512, 2017.

[16] C. Daraio, V. F. Nesterenko, S. Jin, W. Wang, and A. M. Rao, "Impact response by a foamlike forest of coiled carbon nanotubes," *Journal of Applied Physics*, vol. 100, no. 6, article 064309, 2006.

[17] X. Zhang and S. K. Manohar, "Bulk synthesis of polypyrrole nanofibers by a seeding approach," *Journal of the American Chemical Society*, vol. 126, no. 40, pp. 12714-12715, 2004.

[18] E. F. Kukovitsky, S. G. L'vov, N. A. Sainov, V. A. Shustov, and L. A. Chernozatonskii, "Correlation between metal catalyst particle size and carbon nanotube growth," *Chemical Physics Letters*, vol. 355, no. 5-6, pp. 497–503, 2002.

[19] N. Q. Zhao, C. N. He, J. Ding et al., "Bamboo-shaped carbon nanotubes produced by catalytic decomposition of methane over nickel nanoparticles supported on aluminum," *Journal of Alloys and Compounds*, vol. 428, no. 1-2, pp. 79–83, 2007.

[20] S. Sakurai, M. Inaguma, D. N. Futaba, M. Yumura, and K. Hata, "Diameter and density control of single-walled carbon nanotube forests by modulating Ostwald ripening through decoupling the catalyst formation and growth processes," *Small*, vol. 9, no. 21, pp. 3584–3592, 2013.

[21] M. J. Bronikowski, P. A. Willis, D. T. Colbert, K. A. Smith, and R. E. Smalley, "Gas-phase production of carbon single-walled nanotubes from carbon monoxide via the HiPco process: a parametric study," *Journal of Vacuum Science and Technology A*, vol. 19, no. 4, pp. 1800–1805, 2001.

Hindawi
International Journal of Polymer Science
Volume 2020, Article ID 5659682, 16 pages
https://doi.org/10.1155/2020/5659682

Review Article

Conducting Polymer-Based Composite Materials for Therapeutic Implantations: From Advanced Drug Delivery System to Minimally Invasive Electronics

Yang Liu,[1] **Pengfei Yin**,[1] **Jiareng Chen**,[1] **Bin Cui**,[1] **Chao Zhang**,[1] **and Feng Wu**[2]

[1]*Department of Biomedical Engineering, Sun Yat-sen University, Guangzhou, China 510006*
[2]*Bioproducts Discovery & Development Center, University of Guelph, Ontario, Canada*

Correspondence should be addressed to Yang Liu; liuyang56@mail.sysu.edu.cn and Feng Wu; fengwu@uoguelph.ca

Received 20 September 2019; Revised 8 December 2019; Accepted 24 December 2019; Published 6 February 2020

Academic Editor: Victor H. Perez

Conducting polymer-based composites have recently becoming popular in both academic research and industrial practices due to their high conductivity, ease of process, and tunable electrical properties. The multifunctional conducting polymer-based composites demonstrated great application potential for in vivo therapeutics and implantable electronics, including drug delivery, neural interfacing, and minimally invasive electronics. In this review article, the state-of-the-art conducting polymer-based composites in the mentioned biological fields are discussed and summarized. The recent progress on the synthesis, structure, properties, and application of the conducting polymer-based composites is presented, aimed at revealing the structure-property relationship and the corresponding functional applications of the conducting polymer-based composites. Furthermore, key issues and challenges regarding the implantation performance of these composites are highlighted in this paper.

1. Introduction

Conducting polymers (CPs) can be referred to the composite materials comprising polymeric components and conductive components. The polymeric components and the conductive components of the CPs can be arranged in different structures and configurations, e.g., mixing, coating, and hierarchical, to gain the designed functionality. Different from the CPs, the intrinsically conducting polymers (ICPs) can transport the electrons and holes through their unique alternating single-and-double-bond structure in the main chains, and the addition of another conductive phase is not necessary. The discovery of the ICPs dates back to the 1850s with the introduction of polyaniline [1] by Henry Letheby, but only in the 1970s did polyaniline (PANI) and other conducting polymers such as polypyrrole (PPy), polythiophene, and polyacetylene receive intense attention from the scientific and industrial communities due to the breakthrough work done by Heeger, MacDiarmid, and Shirakawa [2]. Conducting polymers are organic polymers that can conduct electricity, which are different from the conventional polymers such as polyethylene and natural rubber, and due to their unusual electrochemical and optical properties, the ICPs have greatly benefitted our society in applications such as energy storage [3], supercapacitors [4, 5], field emission [6], biosensors [7], gas sensors [8], and tissue engineering [9]. Chemical synthesis and electrochemical synthesis are generally two main methods to synthesize ICPs; in particular, electrochemistry has played a key role in the synthesis of ICPs for its fine-tuning in the polymer structures, compositions, and electrochemical properties. Several articles and reviews have been published on the synthesis, properties, and applications of ICPs [10, 11]. However, to achieve a wide range of applicability, excellent mechanical properties, easy processability, and high-performance electrical, sensing, and energy-storage capabilities are required for the next-generation conducting polymer-based composites.

Compared to the bulk polymers, the conducting polymer-based composites which are formed by blending or mixing ICPs with other materials have drawn more attention, and the properties of each individual component can be efficiently integrated to achieve multifunctionality [12]. Various

strategies have been developed to synthesize the conducting polymer-based composites, such as electrosynthesis in the presence of an insulating polymer [8], encapsulation of fibers [13], incorporation of other secondary nanoparticles to form conducting polymer nanocomposites [14], electropolymerization of different monomers (e.g., aniline and 3,4-ethylenedioxythiophene) [15], and the utilization of dopants with multiple functions (e.g., disulfide biotin) [16], and the in situ integration of noble metal nanoclusters during oxidative polymerization (e.g., platinum nanoclusters) [17]. Resulting from the synergistic effect of different components, the conducting polymer-based composites show multifunctionalized properties and enhanced mechanical performance and processability. The structure of the composites, interfacial adhesion between the conducting polymer and other components, and the synthetic strategies would greatly affect the properties and applications of the as-obtained conducting polymer-based composites.

Although it is widely accepted that the key component of neural communications in the human body is the action potential generated at the synapses, the subsequent generation of the electrical charges plays a vital role in the signal transmission and simulation of the neural cells. The applications of ICPs in bioelectronics are quite attractive, as they are intrinsically biocompatible and mechanically soft to realize conformal matches between the electronics and tissues to reduce the foreign body response (FBR). The biocompatibility of ICPs has been extensively investigated both in vitro and in vivo. The reported results indeed demonstrated that the ICPs, especially PPy and poly(3,4-ethylenedioxythiophene) (PEDOT), possessed good biocompatibilities with cells, tissues, and organs [18–23]. Vaitkuviene et al. showed that the PPy nanoparticles synthesized by oxidative polymerization exhibited almost no cytotoxicity to the primary mouse embryonic fibroblasts, mouse hepatoma cell line, and human T lymphocyte Jurkat cell line at low concentrations (up to $9.7\,\mu g\,mL^{-1}$) [19]. They also demonstrated that the PPy-modified gold surface showed good biocompatibilities to support the adhesion and proliferation of mouse bone marrow-derived stem cells, similar to the bare gold and polystyrene surfaces [20]. Wang et al. reported that the PPy extraction solution showed no trace of acute and subacute toxicity, pyretogen, hemolysis, allergen, and mutagenesis. The Schwann cells in the PPy extraction solution also showed higher survival and proliferation rates compared to the saline solution; they also tested the chronic effect of the implanted PPy-coated silicone tube for bridging the transected sciatic nerve. The result showed that the PPy-coated silicone tube can improve the nerve tissue regeneration and induce only light inflammation after 6 months' implantation [21]. George et al. fabricated PPy implants doped with polystyrene sulfonate (PSS) or sodium dodecylbenzenesulfonate (NaDBS) and surgically inserted the PPy implants into the cerebral cortex of rats. Reduced gliosis and enhanced tissue-implant interactions were found on the PPy implants after either 3 weeks' or 6 weeks' implantation, which in most cases outperformed the Teflon implants as the control [22]. Moreover, Ramanaviciene et al. showed that chemically synthesized PPy nanoparticles neither demonstrated any cytotoxic effects on mouse peritoneum cells nor affected the spleen, kidney, or liver indexes and the immune-related hematological parameters of the mice. According to their observation, the PPy nanoparticles also induced no allergic response and no inflammation can be detected in the peritoneum of mice in the sixth week after the injection of PPy nanoparticles [23]. The relatively good biocompatibility of the chemically and electrochemically synthesized ICPs makes them ideal candidates for medical bionics and implantable electrodes, where high electrical conductivity, low impedance, and seamless integration of biomolecules are required to establish an integrated tissue-electrode interface [24, 25].

However, several drawbacks are associated with ICPs and their composites and hinder their biological applications, such as low mechanical strength, low sensitivity and selectivity, and low stability. To overcome the limitations of the ICPs, different methods and strategies have been employed and the results were carefully investigated, including (i) chemical surface modification of conducting polymers with physiologically active species; [26] (ii) blending with other nonconductive polymers with good mechanical properties, e.g., biomass-derived and biodegradable polymers such as PDLLA [27], chitosan [28], collagen [29], cellulose [13], and polysaccharide [30]; (iii) utilizing nanostructured conducting polymers such as nanoparticles, nanotube, nanowires, and nanofibers; [11] and (iv) usage of the physical and covalent surface coating technologies—the conducting polymers were used either as substrates or as coatings [13]. And the biocompatibility of these polymers in the biological tissues was also evaluated using different methods such as "in vitro" assays [31]. After all, the ICPs and their composites hold a perspective future in biological applications, especially in implantable devices and cyborg tissues.

Several review articles have been published on ICPs used in biomedical [32, 33], tissue engineering [9], and biosensors [34, 35]. In this review, we mainly focus on the conducting polymer-based composites and devoted to summarizing their structures, properties, and applications in the biological fields, including drug delivery, neural interfacing, and tissue engineering.

2. Conducting Polymer-Based Composites for Drug Delivery

An efficient drug delivery system that can deliver the drug to targeted body sites and control the drug release rate precisely is able to improve the therapeutic outcomes and reduce the side effects [36, 37]. Structuring such drug delivery systems has been long dreamed of and became more and more practical with the development of a variety of polymer-based delivery systems. From nonbiodegradable diffusion-controlled membranes [38] to biodegradable systems with a combination of diffusion and polymer matrix degradation [39], the polymer-based delivery system has shown enormous benefits in drug delivery and release. And since the 1980s, an effective and intelligent drug delivery system based on the ICPs has been developed [40, 41]. Resulting from their inherent electrical, magnetic, and optical properties, the ICPs, especially their composites, are

expected to be used as next-generation stimuli-responsive drug delivery systems that are smart enough to adjust the release rates according to the changes of the tissue microenvironment. Various ICPs, including PPy and its derivatives, PANI [42], PEDOT, and its derivatives [43], have been used to construct new polymer-based drug delivery systems. The ICPs also showed promising biocompatibility when interfacing with different biological tissues [44], which further proved their application potential in the fabrication of drug delivery systems.

In drug delivery systems, the use of ICPs is significantly limited by the choice of dopant and the molecular weight of the loaded drug. To remove these barriers, chemical modification or physical coating methods have been used. For example, George et al. modified the surface of PPy through biotin-streptavidin coupling [45]. Due to the ability of attaching any biotin-labeled compound, streptavidin bridges the biotinylated drug and PPy (Figure 1(a)). The modified PPy composites show high stability and well-controlled drug release process. Different from the chemical surface modification, Abidian and his coworkers reported the electrochemical depositions of PPy or PEDOT nanotubes on drug-loaded, electrospun biodegradable poly(L-lactide) (PLLA) or poly(lactide-co-glycolide) (PLGA) (Figure 1(b)). This nanostructured conducting polymer composites can be used for the release of dexamethasone with electrical stimulations [43]. The controlled release of dexamethasone was also reported by Wadhwa et al. [41] In their study, the prodrug of dexamethasone disodium phosphate (Figure 1(c)) was used as a dopant in PPy followed by coating PPy on the gold-coated coverslips (electrodes). The release of the dexamethasone was controlled by the cyclic voltammetry (CV) with alternating positive and negative potentials. In this study, 0.5 μg/cm^2 dexamethasone can be released after each CV cycle and up to a total of nearly 16 μg/cm^2 can be released after 30 CV cycles (Figure 1(d)). To further enhance the drug release performance and drug-loading capacity of the ICPs, Woeppel et al. reported the usage of functionalized negatively charged porous silica nanoparticles as the dopant for PEDOT [46]. The silica nanoparticle-doped PEDOT showed significantly enhanced doxorubicin (DOX) release profiles (up to 7-folds higher than the control) by applying electrical stimulations; different kinds of drugs, e.g., fluorescein and DNQX, have been loaded into the porous silica nanoparticle-doped PEDOT and demonstrated controllable release profiles in vivo. Biologically active dopants, such as neural growth factor and brain-derived neurotrophic factor, can also be directly incorporated into the matrices of PPy and PEDOT to promote the neurite outgrowth in vitro [47, 48]. In summary, chemical modification of conducting polymer substrate, coating conducting polymers on the drug-loaded biodegradable polymeric substrate, or prodrug modification have been proven to be the effective methods in preparing conducting polymer composite-based drug delivery systems.

Conducting polymer-hydrogel blends were also synthesized and applied in electrochemically controlled drug delivery systems. Due to their high swelling capacity, hydrophilicity, and quick responses to external stimuli such as strain, pH, and temperature, the hydrogels have been proposed as suitable materials for drug delivery applications [49, 50]. Integration of conducting polymers into the hydrogel may endow smart functions to the as-prepared composites, e.g., switchable delivery modes (on and off) and controls over the drug-releasing rate. Conducting polymers such as PANI [51, 52] and PPy [53, 54] are electropolymerized to grow inside or on the surface of different hydrogels. Semi-interpenetrating PANI-polyacrylamide hydrogel composites were prepared by Lira and de Torresi, and the electrochemically controlled release of safranin has been demonstrated in this research [52]. It was found that the release of safranin was influenced by not only the physical and chemical properties of the composites, but also the electrochemical processes. In another work, drug-loaded PPy nanoparticles were suspended in a temperature-responsive hydrogel (poly[(D,L-lactic acid)-co-(glycolic acid)]-b-poly(ethylene oxide)-b-poly-[(D,L-lactic acid)-co-(glycolic acid)] (PLGA-PEG-PLGA)), which is a liquid at low temperatures but becomes a gel at body temperature, as shown in Figure 2 [54]. The composites acquire the advantages of both conducting polymers and the sol-gel transition of hydrogels, exhibiting a dual stimulus (temperature and electric field) responsiveness and can be used to trigger sensitive dosage-controlled release of drugs. Other conducting polymer-hydrogel systems such as PANI-polysaccharide hydrogels [30], PPy-alginate hydrogel [53], and chitosan-graft-PANI-oxidized dextran hydrogel [55] have also been evaluated to identify their potential in drug delivery applications. Recently, near-infrared light and pH dual responsive drug delivery composites of PANI-biodegradable poly(ethylene glycol)-poly(ε-caprolactone) (PEG5k-PCL10k) block copolymers and lecithin that are used for the controlled release of cisplatin were reported by You and his coworkers [42].

Nowadays, there is an increasing trend in the fabrication of conducting polymer-based composites for drug delivery. However, most ICPs and their composites are not biodegradable, which is considered a major drawback for the ICP-based drug delivery systems, and a postdelivery process is required to remove the drug-loaded carriers. Although several biodegradable conducting polymer composites have been reported [56], it is still a challenge to achieve both high conductivity and appropriate biodegradability. Meanwhile, conducting polymer composites that can response to dual or more stimuli are expected to find widespread applications in drug delivery for their more precisely controlled release rate.

3. Conducting Polymer-Based Composite Electrodes for Neural Interfacing

The nervous system is of great complexity due to the thousands of networks of neurons and supporting cells, which work synchronously to process external and internal cues that result in movements, emotions, sight, speech, and hearing. It is important for knowing the mechanism of the neural network and treating some neural disorders to understand the nervous system, which has engaged the interests of scientists. The neural interface serves as a medium between electrical devices and neural tissues. In other words, the neural

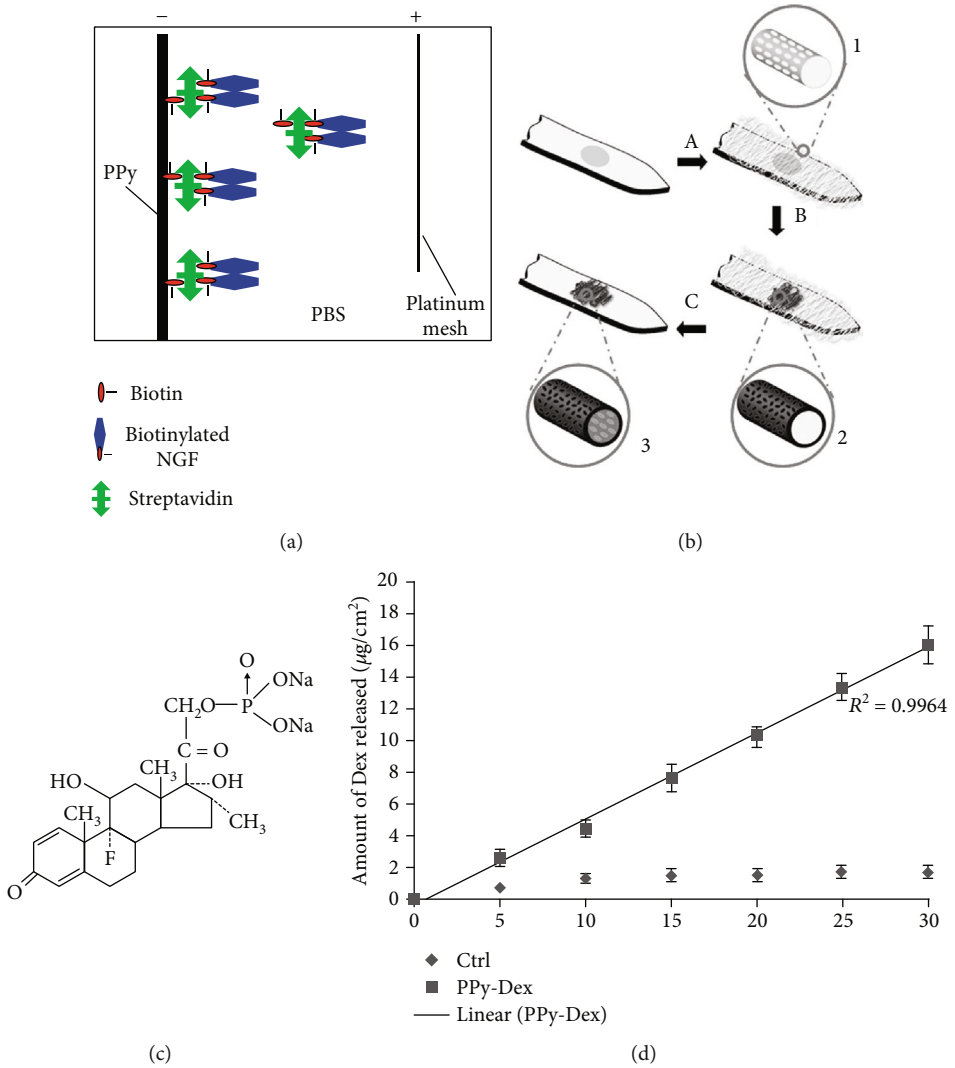

FIGURE 1: Schematic illustrations of the modification of conducting polymers and prodrug for drug delivery systems: (a) release of the biotin from the PPy surface; [45] (b) surface modification of neural microelectrodes to create nanotubular PEDOT; [43] (c) chemical structures of the dexamethasone disodium phosphate (Dex); [41] (d) release profile of Dex from the polymer-drug-coated electrodes [41].

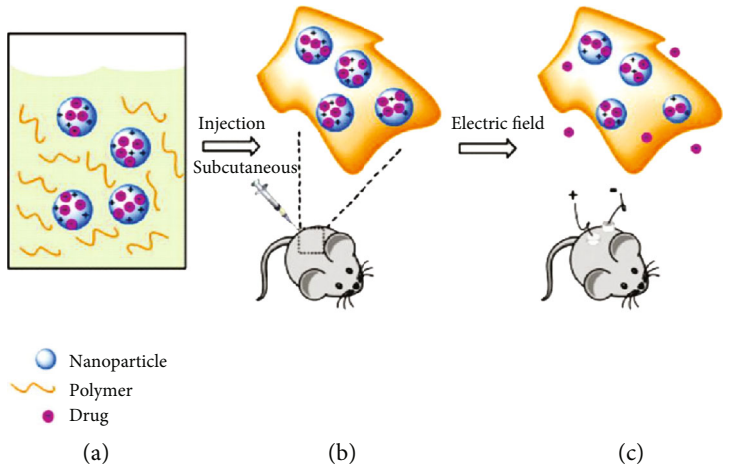

FIGURE 2: General scheme for the application of conducting polymer-hydrogel system. (a) The nanoparticle polymer solution is (b) subcutaneously injected into a mouse, followed by (c) application of a DC electric field to induce release of the drug cargo inside the nanoparticles [54].

interface is a tool to interface between biological and electronic systems, allowing for monitoring and manipulation of neural circuits that underpin both normal and diseased states. The information of nervous networks and their responses to the bioactive materials have been effectively provided by the neural electrodes. When implanted into the brain, neural electrodes can record the signal from the neuron for studying the mechanism of the brain and also can give the degenerated tissues in the brain effective stimulations to heal neurological diseases such as Parkinson's disease, epilepsy, deafness, blindness, and movement disorders. Therefore, it is vital for neural research to have reliable signals taken from the brain for the accurate analysis of the neural system and selective stimulations. For clinical diagnosis, it requires a neural electrode with a high conductivity, low impedance, and good biocompatibility. The traditional neural electrodes are mostly composed of noble metals and may not be competent for long-term implantations and signal recording due to the mechanical mismatch between the stiff metal electrode (E_{metal} = 74-530 GPa [57]) and soft neural tissue (E_{brain} = 2.1-3.7 kPa [58], $E_{\text{spinal cord}}$ = 3-6.3 kPa [59], and $E_{\text{peripheral nerve}}$ = 576-840 kPa [60, 61]). The mechanical mismatch between the electrodes and neural tissues may induce significant FBR at the electrode-neural tissue interface, resulting in the malfunction of both the electrodes and the surrounding tissues. Current research is aimed at producing stable, small, and high-density microelectrodes in order to improve the recording and stimulating selectivity for both in vitro and in vivo applications. To carry out implantation of neural electrodes precisely and selectively and reduce the unwanted damage of neural tissues, the fabrication of neural electrodes with a smaller geometrical size, e.g., microelectrodes, has been widely adapted. However, the small geometrical sizes also limit the electrical functions of the microelectrodes, and increased impedance and reduced charge injection properties are associated with the microelectrodes compared to the bulky ones. To address this issue, the geometric surface of the microelectrodes can be miniaturized to form conductive, porous, and biocompatible nanostructures [62].

Strategies to improve the electrochemical surface area whilst maintaining the desired geometric area include the development of rough microelectrodes and microelectrode coatings onto traditional planar microelectrode materials such as gold and platinum. The metal electrode (gold, platinum, and silver) was coated by conducting materials through chemical and electrochemical deposition. The conducting materials including graphene and graphene oxide (GO) [63], iridium oxide (IrO_x) [64], carbon nanotubes (CNTs) [65], and ICPs [66]. ICPs with high conductivity, excellent charge transport capacity, and good biocompatibility were speculated as promising electrode materials for next-generation neural electronics with reduced neural interfacing impedance. Few researches focused on the way to coat ICPs like PPy [67], PANI [68], and PEDOT [69] on the surface of metallic microelectrodes to enhance their electrochemical properties, which is considered simple but effective. Compared to the bare metal electrodes, the impedance of the modified neural electrodes became smaller due to the increased electrochemical surface area after the deposition of ICPs. For example, Zhou et al. fabricated a PEDOT and multiwall carbon nanotube (MWCNT) composited thin film and coated it onto platinum microelectrodes by different electrochemical deposition methods, i.e., potentiostatic and galvanostatic [70]. Compared to the PEDOT/MWCNT coating formed by the potentiostatic method, the PEDOT/MWCNT film from the galvanostatic method showed a porous morphology composed of tangled rods with a smaller average diameter (~50 nm). The impedances of the PEDOT/MWCNT-coated microelectrodes from the two methods exhibited almost two orders of magnitude lower than the bare platinum microelectrode at 1 kHz. The impedance at 1 kHz is a typical parameter to evaluate the functions of the neural electrodes, as it correlates to power consumption for the electrical stimulation of the neural tissues and the neuronal action potentials. However, the stability of the ICP coating on the microelectrodes is also critical for achieving chronic monitoring of the neural tissues. Few researches have focused on solving these problems by doping inorganic and organic substances into the ICP coating to enhance the adhesion between the ICP films and the substrates and also to enhance the biocompatibility of the electrodes corresponding to the neural tissues. For example, Bodart et al. polymerized PEDOT:tetrafluoroborate (PEDOT:BF_4) onto the platinum neural electrode by using three different solvents, i.e., propylene carbonate (PC), acetonitrile (ACN), and water [71]. The mechanical and electrochemical stabilities of the as-obtained composited electrodes were subsequently analyzed. The result indicated that PEDOT:BF_4 coatings deposited in organic solvents on platinum-iridium (PtIr) microelectrodes remained physically stable after 5 min of sonication and retained more than 80% of their charge storage capacity (CSC), while coatings deposited in deionized water detached from the PtIr microelectrodes after 2-3 min of sonication. After soaking in the PBS (pH = 7.4) solution for two weeks, the impedances of PEDOT-coated microelectrodes obtained in PC and ACN were increased but still considerably lower than the bare PtIr electrode. They concluded that the PtIr electrode coated by the PEDOT:BF_4 film from the organic solvents showed better stability under ultrasonication, PBS soaking, and steam sterilization than the PEDOT:BF_4 coating from water. Cui et al. electrochemically polymerized PPy and a biomolecule (a silk-like polymer having fibronectin fragments (SLPF) and nonapeptide CDPGYIGSR) onto the gold electrode sites of a neural probe [72]. Apart from better performance in electrical properties than the uncoated electrodes, more cells (1.25 ± 0.6 cells per site) were grown on the PPy/SLPF-coated gold electrodes than on the uncoated ones. They also found that human neuroblastoma cells preferred to seed onto the PPy/CDPGYIGSR-modified electrode selectively compared to the electrode coated with PPy/CH_3-COO^- (Figure 3). It indicated that by doping different biomolecules in the conducting polymer coating deposited on the neural electrode, the cell behaviors on the neural electrodes can be mediated to promote the formation of integrated tissue-electronic interfaces.

To further decrease the mechanical mismatch between the electrodes and tissues, and achieve the so-called conformal

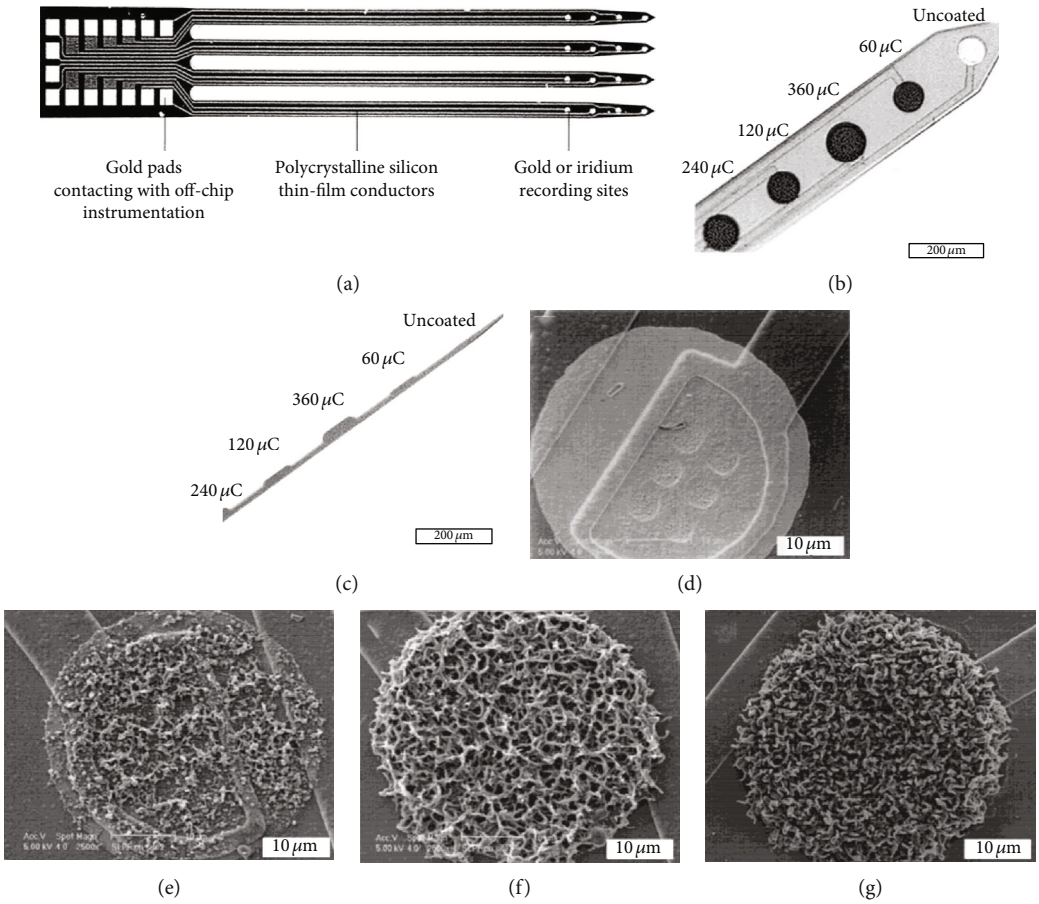

Figure 3: (a) Micromachined metal/silicon-based neural recording probe. (b, c) Optical micrographs of a PPy/PSS-coated 5-channel neural probe. (b) is the top view of the probe, and (c) is the side view from which the thickness of the film can be estimated. The area of each metal electrode is 3900 μm^2, and the thickness of the probe is 15 μm. By varying the deposition charge, the amount of material deposited can be precisely controlled. (d–g) SEM images of PPy/SLPF-coated electrode sites. From (d) to (g), the deposition time increased, corresponding to a total charge passed of (d) 0 μC, (e) 1 μC, (f) 4 μC, and (g) 10 μC. The area of the uncoated electrode site is 1250 μm^2 [72].

electronic-tissue interface, soft substrates such as Parylene C [73], polydimethylsiloxane (PDMS) [74], SU-8 [75], polyimide (PI) [76], and silk fibroin [77] can be introduced to fabricate flexible and highly conductive neural electrodes. Compared to the metal substrate, PI, SU-8, Parylene C, and PDMS acquire much smaller Young's moduli of 8.45 GPa, 5.6 GPa, 4.0 GPa, and 1.0 MPa, respectively. These materials could be utilized to fabricate flexible neural electrodes of different shapes and sizes with improved conformal matching for minimally invasive implantation. For example, Heo et al. fabricated a PI nanofiber- (NF-) based neural interface with a high flexibility and permeability for stable neural signal recording [78]. The neural interface they designed consisted of a PI NF substrate, electronic connection pads composed of silver nanoparticles, and PEDOT: poly(styrenesulfonate) (PEDOT:PSS) as the advanced conductive layer (Figure 4). They demonstrated that the as-obtained NF-based nerve electrode showed electrochemical properties superior to those of conventional cuff electrodes. And it was able to record neural signals for a long period of time, i.e., after implantation for 12 weeks.

4. Conductive Polymer-Based Electronics for Minimally Invasive Electronics

The ICPs, such as PPy [79] and PEDOT [80], can be used as the electrode materials for flexible and stretchable electronics. Their major advantages include biocompatibility and large surface area, resulting in higher in vivo charge transfer capacities [81]. Various biomolecules, such as enzyme, DNA, growth factor, and antibody, can be readily incorporated into the ICPs through electrochemical polymerization as the stimuli to enhance the acquisition of biological cues [82–85]. On the other hand, the CP-based stretchable electrodes for engineered tissues can also be realized by incorporating metal-based or carbon-based nanoparticles into elastomers, such as PDMS or styrene-butadiene-styrene (SBS) [86]. Another way to make CP-based flexible and stretchable electronics is to infuse liquid metal alloys inside microfluidic channels, e.g., filling the eutectic gallium-indium in the PDMS channels.

Bioresorbable macromolecules and polymers can be used as the substrates for the fabrication of CP-based

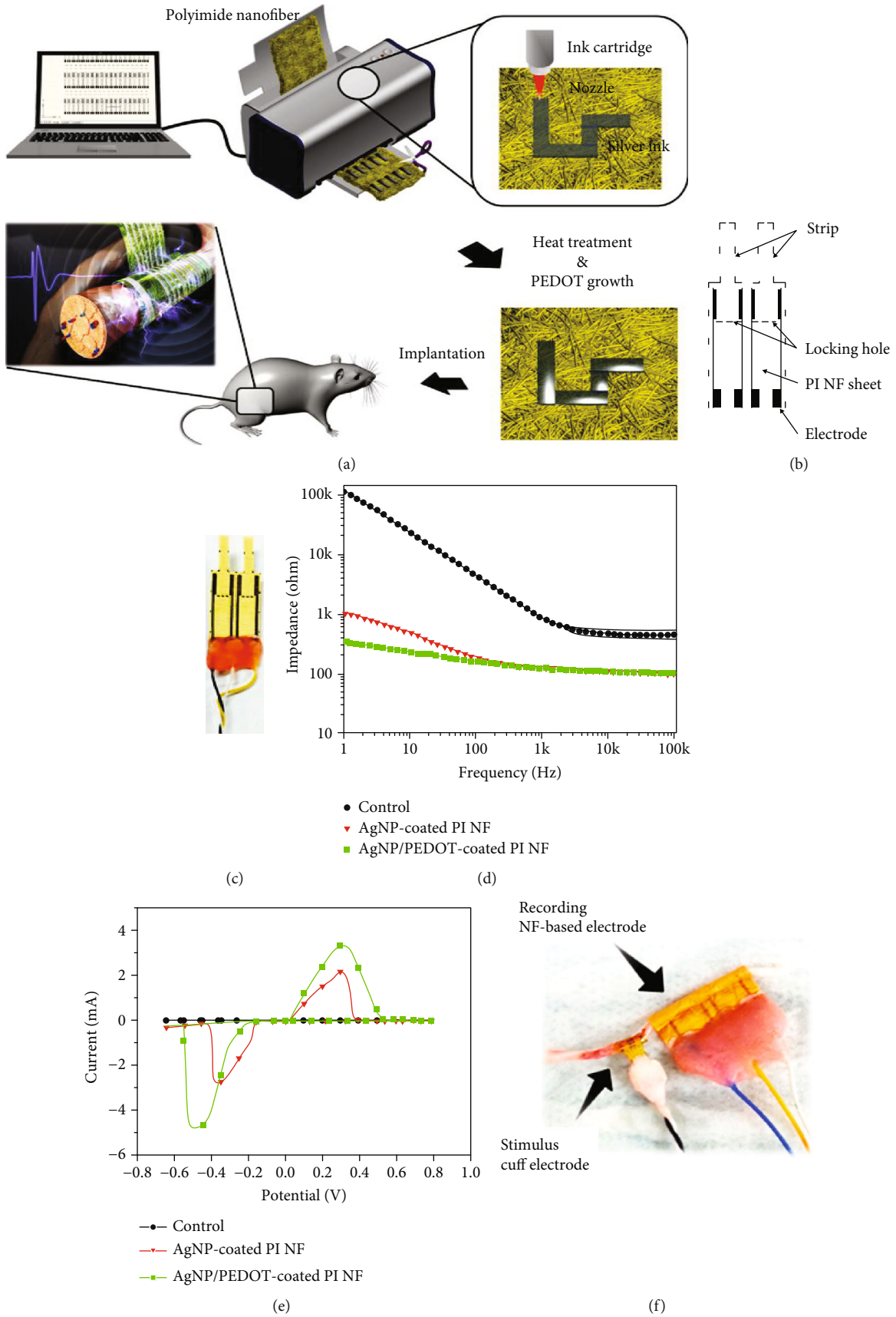

Figure 4: Continued.

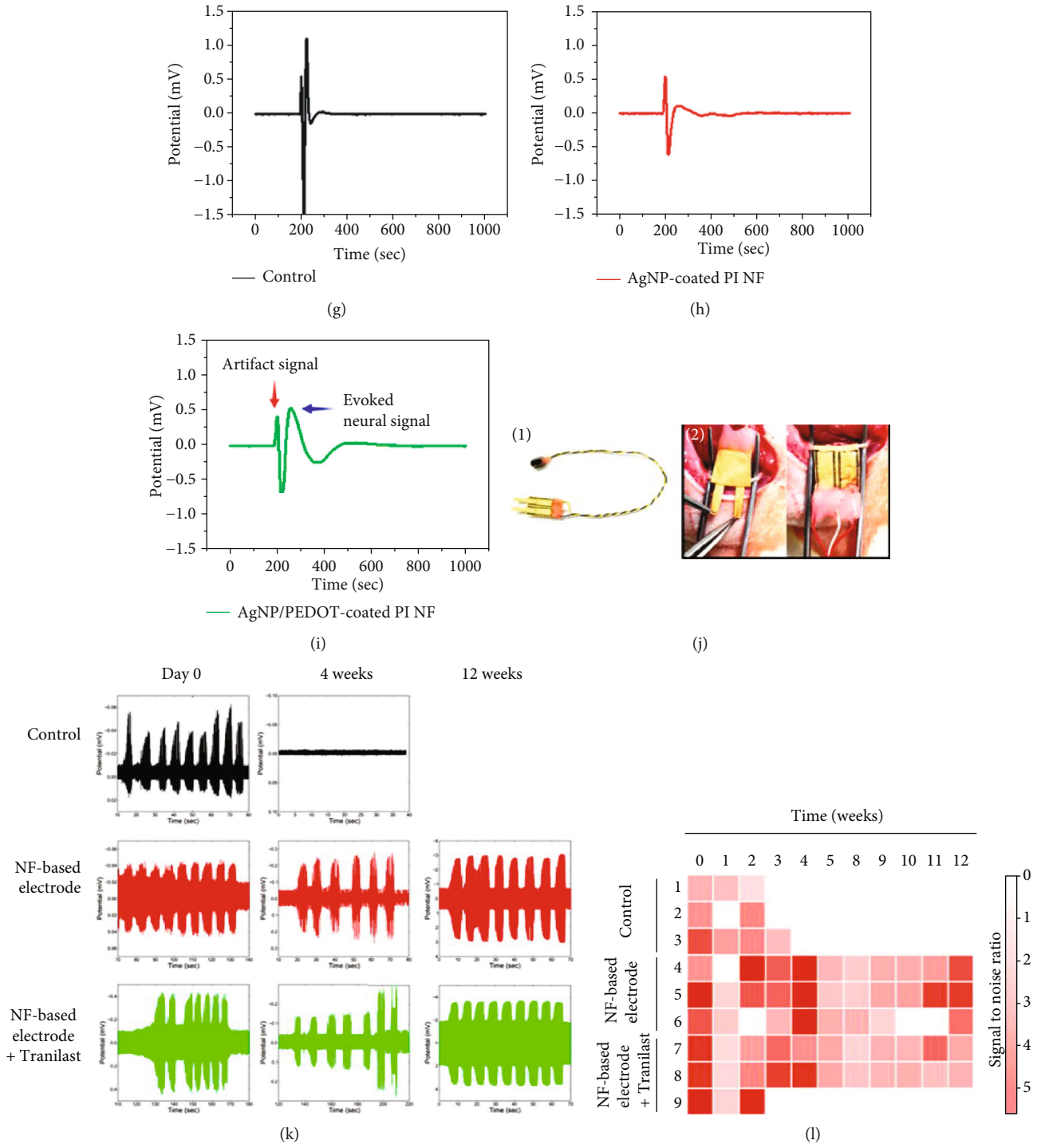

Figure 4: (a) Scheme of the fabrication process using an inkjet printing system. (b) Concept of preproduction design and (c) image of the fabricated NF-based neural electrode. Electric wire cables were bonded to the end of the electrode pads using conductive silver epoxy and were covered with bone cement. (d) Electrochemical impedance spectrum over a frequency range of 1–105 Hz. (e) Cyclic voltammograms with a scan range of −0.7 to +0.8 V at a scan rate of 100 mV/s. (f) Image of a wrapped stimulus cuff electrode and a recording NF-based electrode. Acute ex vivo recordings obtained using (g) a control electrode, (h) AgNP-coated PI NF electrode, and (i) AgNP/PEDOT-coated PI NF electrode. (j) Electrical packaging electrode (1) and implanted electrode (2). The NF-based electrode is wrapped around the sciatic nerve of a rat. (k) Representative neural signal recording obtained from sciatic nerve tissue over a period of 12 weeks using a control electrode, an NF-based electrode, and an NF-based electrode soaked with Tranilast. (l) Simultaneous mapping of the SNR of an NF-based electrode with and without Tranilast [78].

bioelectronics. The utilization of bioresorbable materials to construct the bioresorbable electronics can effectively eliminate the adverse effects of long-term implantation such as the FRB and unfavorable biofilm formation [87]. The substrate layer of bioresorbable electronics can be fabricated by natural or synthetic polymers with tunable degradation properties. For example, the natural protein silk fibroin [88] which can be degraded into natural amino acids by enzymes in vivo. Alternatively, bioresorbable synthetic polymers, such as PLGA, can also be used. The advantages of the natural polymers include higher biocompatibility, reduced FBR, and higher mechanical strengths. Disadvantages include higher cost and lower processability. Compared with natural polymers, the synthetic polymers show the advantages including controllable degradation rate and low cost [89].

The conductive components of the CP-based bioelectronics, such as semiconductors and dielectrics, can be made of silicon and silicon dioxide, which would degrade into nontoxic $Si(OH)_4$ in physiological solutions, and the dissolution rate is dependent on the thickness. For the metallic conductors, the biocompatibilities of gold and platinum are good, but they are not degradable. Magnesium and zinc can dissolve rapidly, and the degradation products are magnesium hydroxide and zinc oxide, which can be easily removed by the human body [90]. Tungsten, molybdenum, and iron can also be dissolved, but the dissolution rates are slower, and the degradation products are iron oxides or hydroxides and tungsten and molybdenum oxides [88]. Therefore, the metal conductors may need to be selected according to the life expectancy of the bioresorbable electronics. Zinc and magnesium are suitable for short-term implantation, while tungsten, molybdenum, and iron are suitable for long-term implantation [91].

The flexible polymeric substrates and conductive materials can be integrated to fabricate CP-based bioresorbable electronics in various structures and configurations to achieve minimally invasive implantations, e.g., the injectable bioelectronics. Typical structures of the injectable bioelectronics are cylindrical, consisting of a microchip and integrated electronic components such as semiconducting electronic components, solenoid microcoils, and hybrid charge storage capacitors. All the electronic components of the injectable bioelectronics are combined in a thin film of an integrated circuit chip. Metal electrodes are extended from both ends of the device, acting as the stimulation electrodes to activate the nearby nerves or muscle motions [92]. With the development of injectable bioelectronics, reticular electronic implants were found to have excellent mechanical and structural properties and were widely used in the neural research, e.g., the single-neuron chronic recording for the retina in awake mice [93] and seamless syringe-injectable mesh electronics with minimal chronic immune response for brain monitoring [94]. Mesh-shape flexible bioelectronics provide new solutions for the signal recording and stimulation of brain tissues during implantation, and they can avoid problems associated with traditional rigid wire-shape electrodes such as mechanical mismatch and FBR [93–99]. The unique macroporous morphology with submicrometer thickness and cell-scale-wide mesh elements may realize the stable and seamless tissue integration by virtue of their unique mechanical and structural properties [94, 95, 97]. Previous studies on the mesh-shape electronics also demonstrated stable chronic recording at the single-neuron level for at least eight months [91].

Key points related to the structural design of standard mesh electronics are highlighted in Figures 5(a) and 5(b) [100]. Periodic unit structures are constructed for the standard mesh electronic probes (Figures 5(a) and 5(b)). The unit cell of the mesh consists of longitudinal elements parallel to the injection direction and transverse elements oriented at an angle α of 45° relative to the longitudinal direction (Figure 5(b)) [94, 96–99]. The longitudinal elements may have composite structures, consisting of gold interconnects sandwiched between two layers of the biocompatible photoresist SU-8 [101]. One end of the longitudinal element is connected to a sensor or stimulator such as a metal electrode [94–98, 102] or nanowire transistor [95, 102, 103], and the other end is connected to an input/output (I/O) pad. The transverse elements may consist of two SU-8 layers with a total thickness of approximately 800 nm and a width of 20 μm [95]. The transverse elements determine the transverse bending stiffness of the overall mesh structure, and correspondingly, it also determines the rolling degree of grid probes when they are loaded into the needle. After all, both longitudinal and transverse elements contribute to the longitudinal bending stiffness of the mesh probe, and a sufficient longitudinal bending stiffness may maintain the overall linear structure of the mesh electronics during injection [95, 96].

Besides the mesh-like structure, biomimetic neuron-like structures for implantable bioelectronics were also proposed by Yang et al. [104] The neuron-like electronic unit (NeuE) is structurally and mechanically mimicking a neuron at the subcellular level. The photoresists of SU-8 and S1805 were used as the polymeric phase while chromium, gold, and platinum were used as the conductive phase of the NeuE. The sizes of the metal recording blocks of NeuE also match those of the targeted neural cells. The interconnects of the neuron-like structure have similar flexibility to the axons. And the thin polymer insulating layer of the structure is also analogous to the myelin sheath. Both of these features promote in the propagation of electrical signals from the neural cells to the electrodes. The NeuE can also be assembled into an open three-dimensional neuron-like electronic network with structures and morphologies mimicking the natural neural network. However, the properties and functions of the implantable bioelectronics are closely related to their designed structures. In recent studies, mesh-like minimally invasive electronics are often reported to have ultraflexible structures so that they can on the one hand be delivered by capillary needles and on the other hand be perfectly adapted to the nonplanar surface of the brain tissues. The ultraflexible mesh electronics comprising the SU-8 polymeric layer and metallic electrodes can minimize the accumulation of astrocytes and glial cells [94, 95]. In the meantime, it can also reduce the glial scarring (Figure 6(a)), resulting in little or no chronic immune responses in the brain [94, 105].

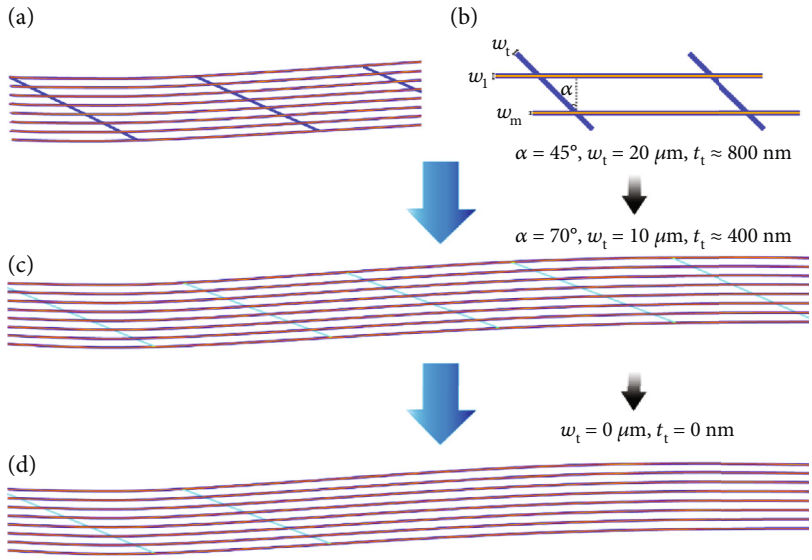

Figure 5: Structural design of ultraflexible syringe-injectable mesh electronics. (a) Schematic of a conventional mesh electronic probe. (b) Schematic of the mesh electronic unit cell, highlighting key probe design parameters, including the angle between longitudinal and transverse elements (α), the longitudinal element width (w_l), the transverse element width (w_t), the longitudinal interconnect metal width (w_m), and the transverse element thickness (t_t). For the standard mesh ($\alpha = 45°$, $w_l = 20\ \mu$m, $w_t = 20\ \mu$m, $w_m = 10\ \mu$m, and $t_t \approx 800$ nm). (c) Schematic of ultraflexible 2D mesh electronics to facilitate loading and injection using reduced diameter needles and injection volumes, where $\alpha = 70°$, $w_t = 10\ \mu$m, and $t_t \approx 400$ nm; parameters for the longitudinal elements are the same as in the standard design highlighted in panel (b). (d) Schematic of ultraflexible 1D mesh electronics with transverse element removal in the implantation site, i.e., w_t and t_t equal to zero, and the parameters for the longitudinal elements and transverse elements external to the implantation region are the same as the 2D probes highlighted in panel (c). Orange lines represent the gold interconnects, dark blue lines represent two SU-8 layers for interconnect insulation, and the cyan line represents a single SU-8 layer [100].

The implant process was conducted by ultra-small-size needles; therefore, minimal damage was induced at the implant site [93, 94]. To inject the device into targeted tissues, the ultraflexible mesh-shape electronics are preloaded in a glass capillary needle, then are injected to the targeted site, and the mesh electronics are unfolded (Figure 6(b)) [93, 95]. The match between the injection rate of the mesh electronics and the retraction rate of the needle after injection has been proven to be the key factor to deliver the mesh electrons to the targeted tissue with an unfolded conformation (Figure 6(c)) [96]. On the other hand, the use of needles and probes with smaller sizes can further reduce the damage applied to the tissues and maintain the original vascular and cellular structures during the injection process. Several methods have been reported to reduce the probe size, e.g., the utilizations of ultraflexible two-dimensional (2D) and one-dimensional (1D) probes have been proven to be effective in reducing the transverse bending stiffness of the electronics, and they can be injected through the glass needles with an inner diameter as small as 100 μm and an outer diameter of 170 μm [100]. In another study, the devices made by the nanoelectronic thread (NET) were reported to obtain a minuscule size [105]. The epoxy-based SU-8 was used as the polymeric phase while gold and platinum were used as the conductive interconnects and electrodes for NET. The NET-50 showed a total thickness of 1 μm and an average width of 50 μm, and the NET-10 showed a cross-sectional area of 10 μm × 1.5 μm. Due to the extremely small thickness, the bending stiffness of NET-50 and NET-10 is much lower than those of the typical silicon, carbon fiber, PI, and Parylene C probes (Figure 6(d)). Recently, Liu et al. showed that the longitudinal and transverse bending stiffness of the mesh-shape electronics, D_L and D_T, was dependent on the angle between the longitudinal and transverse elements (α shown in Figure 5(b)) [95]. When $\alpha = 45°$, D_L and D_T were $\sim 2.5 \times 10^{-3}$ nN · m and $\sim 10^{-2}$ nN·m, respectively. And the bending stiffness of the injected mesh electronics can be reduced to 0.087 nN·m. The bending stiffness was further reduced to 10^{-15} N·m^2 by utilizing the NET structures which realized the glial scar-free neural integration [105]. Moreover, the bending stiffness of the biomimetic neuron-like electronics decreased 5-20 times as compared to the other state-of-the-art mesh electronic designs, and both a structurally and functionally stable tissue-electronic interface can be formed after implantation [104].

The electronic properties such as stable impedance and large signal-to-noise ratio (SNR) are also critical to achieve a highly integrated tissue-electronic interface for chronic and real-time monitoring. For the NET probes, the impedance was around 750 kΩ after implantation and decreased to around 600 kΩ in the first 1.5 months. The impedance was then observed to remain stable for the next 2.5 months accompanied with low noise levels (Figure 6(e)) [105]. Sortable single-unit action potentials (APs) with stable average amplitude and SNR can also be obtained by the NET probes throughout the experimental period of 4 months (Figure 6(f)). On the other hand, the mesh electronics showed higher biocompatibilities as compared to the flexible

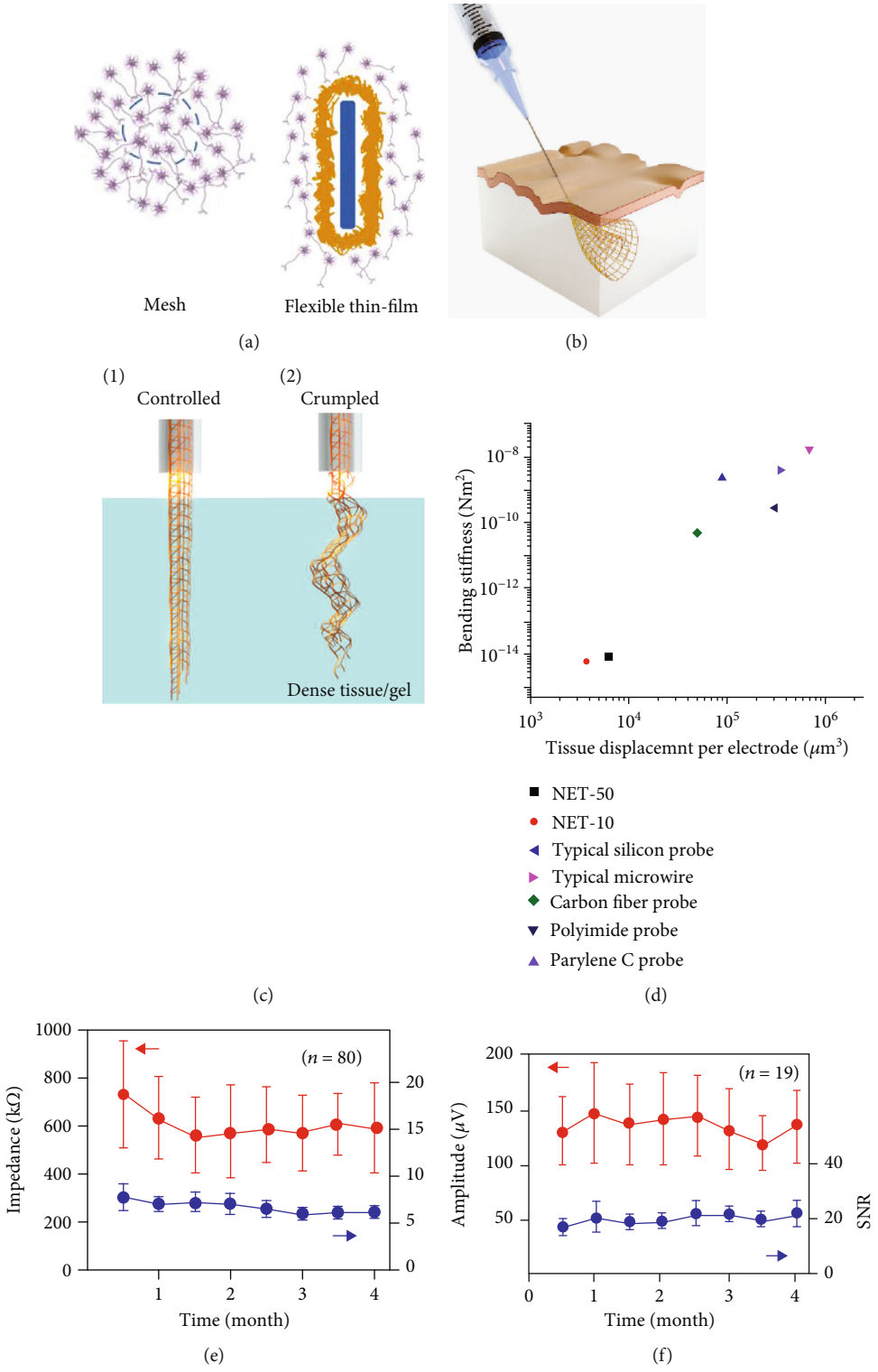

Figure 6: Continued.

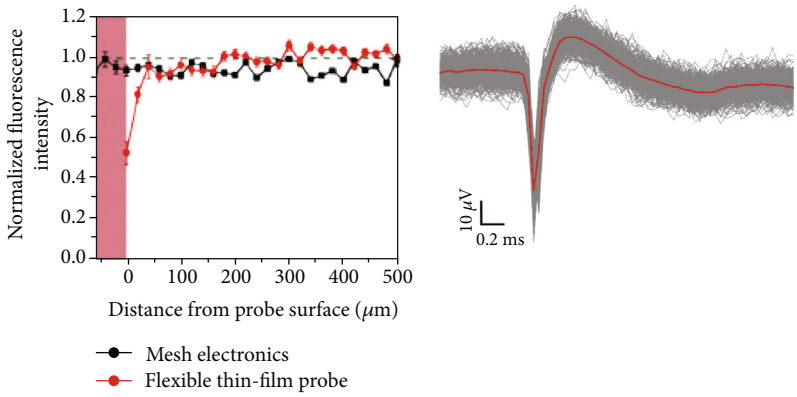

Figure 6: (a) Thin-film electronics may induce the glial scar formation while the mesh electronics may not. The blue lines represent different types of electronics (mesh and thin film), the neurons are in purple, and the glial scars are in yellow [94]. (b) Schematic showing a mesh electronic that is injected into the tissue and extended [95]. (c) Mesh electronics injected by the balanced FoV approach was extended (1). And a mismatched injection may result in a wrinkled mesh (2) [96]. (d) A comparison between the bending stiffness of the NET-structured probes and other typical fiber-based probes [105]. (e) Stable impedance (red) and low noise level (blue) were demonstrated by the NET-structured probes during a long-term recording process (~4 months) [105]. (f) Stable average amplitude (red) and large SNR (blue) for the chronic recording of single-unit APs were also observed on the NET probes [105]. (g) Stable fluorescence intensity of neuron somata can be obtained near the surface of the mesh electronics as compared to the flexible thin-film probes [94]. (h) Single-unit neural recording from one channel of the mesh electronics; the average potential waveform (red) showed characteristic average duration of 2 ms and peak-to-peak amplitude of 70 μV of the single-unit APs [95].

thin-film probes according to the immunohistochemical characterization, as the fluorescence intensity corresponding to the neuron somata was much higher near the surface of the mesh electronics (Figure 6(g)), and the intensities of astrocytes and microglia were much lower [94, 97, 104]. Controlled injection of the mesh electronics has also been realized by a stereotaxic surgery station equipped with a syringe pump, and a spatial precision of ca. 20 μm has been achieved. And subsequently, 100% multichannel input/output (I/O) connectivity between the mesh electronics and a flexible cable device can be achieved by using a computer-controlled conductive ink printing technique [96].

The CP-based injectable electronics with minimal invasiveness have great potential for neural study and brain recording such as single-unit neural AP recording [95], brain mapping [97, 106], and biochemical sensing [107] which may promote the establishment of a next-generation brain-machine interface for both fundamental neuroscience and therapies [108]. By maximally reducing the tissue damage during implantation and minimizing the chronic immunoresponses, the CP-based injectable electronics can serve as a long-term monitoring platform in vivo [109] and can retrieve the physiological signals from the deep brain regions [110]. The CP-based injectable electronics can also integrate with the wireless devices for the applications of wireless optogenetics [111].

5. Conclusions and Future Work

Upon integrating the flexibilities of polymers and conductivities of metals, the CP-based composites show promising applications for the in vivo therapeutics and implantable electronics, including drug delivery, neural interfacing, and injectable electronics. The ICPs can be utilized as the biocompatible, tunable, and controllable advanced delivery platforms for the in vivo targeted transport of the negatively charged drug molecules. And they can also be integrated with other functional materials such as metallic electrodes and hydrogels to form multifunctional composites for tissue monitoring, stimulation, and drug delivery. High-performance neural recording electrodes with significantly enhanced biocompatibility and sensitivity can be fabricated by coating the nanostructured ICPs onto the metallic electrodes. Flexible electronics which conformally comply with the epidermal layer of tissues can also be obtained by coating the ICPs on polymeric substrates using various techniques, such as photolithography, inkjet printing, and electrodeposition. On the other hand, ultraflexible CP-based composites can be obtained by integrating the polymeric photoresists with metallic electrodes in various structures and configurations, such as the mesh- and thread-like shapes. The ultraflexible CP-based composites can be further utilized as the injectable electronics for minimally invasive implantation and show high performance in chronic recording, neural monitoring, and single-neuron-level brain mapping. To further transform the lab-based technique into therapeutic applications, the mechanical property and chemical stability of the ICPs may need to be improved for drug delivery. The chronic performance of the ICPs and the patterning precision of the printing electronics may need to be further improved for the flexible electronics. Finally, concerns over the biocompatibility of the CP-based injectable electronics also arise since highly cross-linked nondegradable SU-8 and metallic chromium with biological toxicity are used.

Conflicts of Interest

The authors declare no conflict of interests.

Acknowledgments

The authors gratefully acknowledge the financial supports from Sun Yat-sen University, the China Postdoctoral Foundation (2018M633230), the National Natural Science Foundation of China (81801851), and the Guangdong Science and Technology Department (2018A030310075).

References

[1] G. Inzelt, *Conducting polymers: a new era in electrochemistry*, Springer Science & Business Media, 2012.

[2] S. S. Shinde and J. A. Kher, "A review on polyaniline and its noble metal composites," *International Journal of Innovative Research in Science, Engineering and Technology*, vol. 3, no. 10, pp. 16570–16576, 2014.

[3] L. Pan, H. Qiu, C. Dou et al., "Conducting polymer nanostructures: template synthesis and applications in energy storage," *International Journal of Molecular Sciences*, vol. 11, no. 7, pp. 2636–2657, 2010.

[4] C. Peng, S. Zhang, D. Jewell, and G. Z. Chen, "Carbon nanotube and conducting polymer composites for supercapacitors," *Progress in Natural Science*, vol. 18, no. 7, pp. 777–788, 2008.

[5] E. Frackowiak, V. Khomenko, K. Jurewicz, K. Lota, and F. Beguin, "Supercapacitors based on conducting polymers/-nanotubes composites," *Journal of Power Sources*, vol. 153, no. 2, pp. 413–418, 2006.

[6] B. H. Kim, D. H. Park, J. Joo, S. G. Yu, and S. H. Lee, "Synthesis, characteristics, and field emission of doped and de-doped polypyrrole, polyaniline, poly(3,4-ethylenedioxythiophene) nanotubes and nanowires," *Synthetic Metals*, vol. 150, no. 3, pp. 279–284, 2005.

[7] T. Ahuja, I. A. Mir, D. Kumar, and Rajesh, "Biomolecular immobilization on conducting polymers for biosensing applications," *Biomaterials*, vol. 28, no. 5, pp. 791–805, 2007.

[8] R. Gangopadhyay and A. De, "Conducting polymer composites: novel materials for gas sensing," *Sensors and Actuators B: Chemical*, vol. 77, no. 1-2, pp. 326–329, 2001.

[9] A. D. Bendrea, L. Cianga, and I. Cianga, "Review paper: progress in the field of conducting polymers for tissue engineering applications," *Journal of Biomaterials Applications*, vol. 26, no. 1, pp. 3–84, 2011.

[10] T. K. Das and S. Prusty, "Review on conducting polymers and their applications," *Polymer - Plastics Technology and Engineering*, vol. 51, no. 14, pp. 1487–1500, 2012.

[11] H. D. Tran, D. Li, and R. B. Kaner, "One-dimensional conducting polymer nanostructures: bulk synthesis and applications," *Advanced Materials*, vol. 21, no. 14-15, pp. 1487–1499, 2009.

[12] J. Yang, Y. Liu, S. Liu, L. Li, C. Zhang, and T. Liu, "Conducting polymer composites: material synthesis and applications in electrochemical capacitive energy storage," *Materials Chemistry Frontiers*, vol. 1, no. 2, pp. 251–268, 2017.

[13] J. H. Johnston, F. M. Kelly, J. Moraes, T. Borrmann, and D. Flynn, "Conducting polymer composites with cellulose and protein fibres," *Current Applied Physics*, vol. 6, no. 3, pp. 587–590, 2006.

[14] X. Lu, W. Zhang, C. Wang, T. C. Wen, and Y. Wei, "One-dimensional conducting polymer nanocomposites: synthesis, properties and applications," *Progress in Polymer Science*, vol. 36, no. 5, pp. 671–712, 2011.

[15] S. Kulandaivalu, Z. Zainal, and Y. Sulaiman, "Influence of monomer concentration on the morphologies and electrochemical properties of PEDOT, PANI, and PPy prepared from aqueous solution," *International Journal of Polymer Science*, vol. 2016, Article ID 8518293, 12 pages, 2016.

[16] W. Y. Hong, S. H. Jeon, E. S. Lee, and Y. Cho, "An integrated multifunctional platform based on biotin-doped conducting polymer nanowires for cell capture, release, and electrochemical sensing," *Biomaterials*, vol. 35, no. 36, pp. 9573–9580, 2014.

[17] Y. Liu, N. Lu, S. Poyraz et al., "One-pot formation of multifunctional Pt-conducting polymer intercalated nanostructures," *Nanoscale*, vol. 5, no. 9, pp. 3872–3879, 2013.

[18] B. Guo and P. X. Ma, "Conducting polymers for tissue engineering," *Biomacromolecules*, vol. 19, no. 6, pp. 1764–1782, 2018.

[19] A. Vaitkuviene, V. Kaseta, J. Voronovic et al., "Evaluation of cytotoxicity of polypyrrole nanoparticles synthesized by oxidative polymerization," *Journal of Hazardous Materials*, vol. 250-251, pp. 167–174, 2013.

[20] A. Vaitkuviene, V. Ratautaite, L. Mikoliunaite et al., "Some biocompatibility aspects of conducting polymer polypyrrole evaluated with bone marrow-derived stem cells," *Colloids and Surfaces A: Physicochemical and Engineering Aspects*, vol. 442, pp. 152–156, 2014.

[21] X. Wang, X. Gu, C. Yuan et al., "Evaluation of biocompatibility of polypyrrole in vitro and in vivo," *Journal of Biomedical Materials Research Part A*, vol. 68, no. 3, pp. 411–422, 2004.

[22] P. M. George, A. W. Lyckman, D. A. LaVan et al., "Fabrication and biocompatibility of polypyrrole implants suitable for neural prosthetics," *Biomaterials*, vol. 26, no. 17, pp. 3511–3519, 2005.

[23] A. Ramanaviciene, A. Kausaite, S. Tautkus, and A. Ramanavicius, "Biocompatibility of polypyrrole particles: an in-vivo study in mice," *The Journal of Pharmacy and Pharmacology*, vol. 59, no. 2, pp. 311–315, 2007.

[24] S. E. Moulton, M. J. Higgins, R. M. I. Kapsa, and G. G. Wallace, "Organic bionics: a new dimension in neural communications," *Advanced Functional Materials*, vol. 22, no. 10, pp. 2003–2014, 2012.

[25] R. Jalili, A. Kanneganti, M. I. Romero-Ortega, and G. G. Wallace, "Implantable electrodes," *Current Opinion in Electrochemistry*, vol. 3, no. 1, pp. 68–74, 2017.

[26] J. W. Lee, F. Serna, J. Nickels, and C. E. Schmidt, "Carboxylic acid-functionalized conductive polypyrrole as a bioactive platform for cell adhesion," *Biomacromolecules*, vol. 7, no. 6, pp. 1692–1695, 2006.

[27] H. Xu, J. M. Holzwarth, Y. Yan et al., "Conductive PPY/PDLLA conduit for peripheral nerve regeneration," *Biomaterials*, vol. 35, no. 1, pp. 225–235, 2014.

[28] Y. A. Ismail, S. R. Shin, K. M. Shin et al., "Electrochemical actuation in chitosan/polyaniline microfibers for artificial muscles fabricated using an in situ polymerization," *Sensors and Actuators B: Chemical*, vol. 129, no. 2, pp. 834–840, 2008.

[29] H. S. Kim, H. L. Hobbs, L. Wang, M. J. Rutten, and C. C. Wamser, "Biocompatible composites of polyaniline nanofibers and collagen," *Synthetic Metals*, vol. 159, no. 13, pp. 1313–1318, 2009.

[30] B. Guo, A. Finne-Wistrand, and A. C. Albertsson, "Facile synthesis of degradable and electrically conductive polysaccharide hydrogels," *Biomacromolecules*, vol. 12, no. 7, pp. 2601–2609, 2011.

[31] R. A. Green, N. H. Lovell, and L. A. Poole-Warren, "Cell attachment functionality of bioactive conducting polymers for neural interfaces," *Biomaterials*, vol. 30, no. 22, pp. 3637–3644, 2009.

[32] G. Kaur, R. Adhikari, P. Cass, M. Bown, and P. Gunatillake, "Electrically conductive polymers and composites for biomedical applications," *RSC Advances*, vol. 5, no. 47, pp. 37553–37567, 2015.

[33] D. Svirskis, J. Travas-Sejdic, A. Rodgers, and S. Garg, "Electrochemically controlled drug delivery based on intrinsically conducting polymers," *Journal of Controlled Release*, vol. 146, no. 1, pp. 6–15, 2010.

[34] M. Gerard, A. Chaubey, and B. D. Malhotra, "Application of conducting polymers to biosensors," *Biosensors & Bioelectronics*, vol. 17, no. 5, pp. 345–359, 2002.

[35] Rajesh, T. Ahuja, and D. Kumar, "Recent progress in the development of nano-structured conducting polymers/nanocomposites for sensor applications," *Sensors and Actuators B: Chemical*, vol. 136, no. 1, pp. 275–286, 2009.

[36] R. Langer, "Drug delivery and targeting," *Nature*, vol. 392, no. 6679, pp. 5–10, 1998.

[37] T. M. Allen and P. R. Cullis, "Drug delivery systems: entering the mainstream," *Science*, vol. 303, no. 5665, pp. 1818–1822, 2004.

[38] J. Folkman and D. M. Long, "The use of silicone rubber as a carrier for prolonged drug therapy," *The Journal of Surgical Research*, vol. 4, no. 3, pp. 139–142, 1964.

[39] K. S. Soppimath, T. M. Aminabhavi, A. R. Kulkarni, and W. E. Rudzinski, "Biodegradable polymeric nanoparticles as drug delivery devices," *Journal of Controlled Release*, vol. 70, no. 1-2, pp. 1–20, 2001.

[40] B. Zinger and L. L. Miller, "Timed release of chemicals from polypyrrole films," *Journal of the American Chemical Society*, vol. 106, no. 22, pp. 6861–6863, 1984.

[41] R. Wadhwa, C. F. Lagenaur, and X. T. Cui, "Electrochemically controlled release of dexamethasone from conducting polymer polypyrrole coated electrode," *Journal of Controlled Release*, vol. 110, no. 3, pp. 531–541, 2006.

[42] C. You, H. Wu, M. Wang et al., "Near-infrared light and pH dual-responsive targeted drug carrier based on core-crosslinked polyaniline nanoparticles for intracellular delivery of cisplatin," *Chemistry - A European Journal*, vol. 23, no. 22, pp. 5352–5360, 2017.

[43] M. R. Abidian, D. H. Kim, and D. C. Martin, "Conducting-polymer nanotubes for controlled drug release," *Advanced Materials*, vol. 18, no. 4, pp. 405–409, 2006.

[44] D. D. Ateh, H. A. Navsaria, and P. Vadgama, "Polypyrrole-based conducting polymers and interactions with biological tissues," *Journal of The Royal Society Interface*, vol. 3, no. 11, pp. 741–752, 2006.

[45] P. M. George, D. A. LaVan, J. A. Burdick, C. Y. Chen, E. Liang, and R. Langer, "Electrically controlled drug delivery from biotin-doped conductive polypyrrole," *Advanced Materials*, vol. 18, no. 5, pp. 577–581, 2006.

[46] K. M. Woeppel, X. S. Zheng, Z. M. Schulte, N. L. Rosi, and X. T. Cui, "Nanoparticle doped PEDOT for enhanced electrode coatings and drug delivery," *Advanced Healthcare Materials*, vol. 8, no. 21, article 1900622, 2019.

[47] D. H. Kim, S. M. Richardson-Burns, J. L. Hendricks, C. Sequera, and D. C. Martin, "Effect of immobilized nerve growth factor on conductive polymers: electrical properties and cellular response," *Advanced Functional Materials*, vol. 17, no. 1, pp. 79–86, 2007.

[48] A. J. Evans, B. C. Thompson, G. G. Wallace et al., "Promoting neurite outgrowth from spiral ganglion neuron explants using polypyrrole/BDNF-coated electrodes," *Journal of Biomedical Materials Research Part A*, vol. 91A, no. 1, pp. 241–250, 2009.

[49] Y. Qiu and K. Park, "Environment-sensitive hydrogels for drug delivery," *Advanced Drug Delivery Reviews*, vol. 53, no. 3, pp. 321–339, 2001.

[50] S. Kalia, *Polymeric hydrogels as smart biomaterials*, Springer International Publishing, Switzerland, 2016.

[51] L. M. Low, S. Seetharaman, K. Q. He, and M. J. Madou, "Microactuators toward microvalves for responsive controlled drug delivery," *Sensors and Actuators B: Chemical*, vol. 67, no. 1-2, pp. 149–160, 2000.

[52] L. M. Lira and S. I. Córdoba de Torresi, "Conducting polymer-hydrogel composites for electrochemical release devices: synthesis and characterization of semi-interpenetrating polyaniline- polyacrylamide networks," *Electrochemistry Communications*, vol. 7, no. 7, pp. 717–723, 2005.

[53] D. H. Kim, M. Abidian, and D. C. Martin, "Conducting polymers grown in hydrogel scaffolds coated on neural prosthetic devices," *Journal of Biomedical Materials Research Part A*, vol. 71, no. 4, pp. 577–585, 2004.

[54] J. Ge, E. Neofytou, T. J. Cahill II, R. E. Beygui, and R. N. Zare, "Drug release from electric-field-responsive nanoparticles," *ACS Nano*, vol. 6, no. 1, pp. 227–233, 2012.

[55] J. Qu, X. Zhao, P. X. Ma, and B. Guo, "Injectable antibacterial conductive hydrogels with dual response to an electric field and pH for localized "smart" drug release," *Acta Biomaterialia*, vol. 72, pp. 55–69, 2018.

[56] B. Guo, L. Glavas, and A. C. Albertsson, "Biodegradable and electrically conducting polymers for biomedical applications," *Progress in Polymer Science*, vol. 38, no. 9, pp. 1263–1286, 2013.

[57] M. A. Mahmoud, P. Szymanski, and M. A. El-Sayed, "Different methods of increasing the mechanical strength of gold nanocages," *Journal of Physical Chemistry Letters*, vol. 3, no. 23, pp. 3527–3531, 2012.

[58] M. A. Green, L. E. Bilston, and R. Sinkus, "In vivo brain viscoelastic properties measured by magnetic resonance elastography," *NMR in Biomedicine*, vol. 21, no. 7, pp. 755–764, 2008.

[59] T. Saxena, J. L. Gilbert, and J. M. Hasenwinkel, "A versatile mesoindentation system to evaluate the micromechanical properties of soft, hydrated substrates on a cellular scale," *Journal of Biomedical Materials Research Part A*, vol. 90A, no. 4, pp. 1206–1217, 2009.

[60] A. Y. Mekaj, A. A. Morina, S. Lajqi, S. Manxhuka-Kerliu, F. M. Kelmendi, and S. B. Duci, "Biomechanical properties

of the sciatic nerve following repair: effects of topical application of hyaluronic acid or tacrolimus," *International Journal of Clinical and Experimental Medicine*, vol. 8, no. 11, pp. 20218–20226, 2015.

[61] G. H. Borschel, K. F. Kia, W. M. Kuzon Jr., and R. G. Dennis, "Mechanical properties of acellular peripheral nerve," *The Journal of Surgical Research*, vol. 114, no. 2, pp. 133–139, 2003.

[62] M. Ganji, A. C. Paulk, J. C. Yang et al., "Selective formation of porous Pt nanorods for highly electrochemically efficient neural electrode interfaces," *Nano Letters*, vol. 19, no. 9, pp. 6244–6254, 2019.

[63] D. Duc, P. R. Stoddart, S. L. McArthur et al., "Fabrication of a biocompatible liquid crystal graphene oxide-gold nanorods electro- and photoactive interface for cell stimulation," *Advanced Healthcare Materials*, vol. 8, no. 9, article 1801321, 2019.

[64] C. Chen, S. Ruan, X. Bai, C. Lin, C. Xie, and I. S. Lee, "Patterned iridium oxide film as neural electrode interface: biocompatibility and improved neurite outgrowth with electrical stimulation," *Materials Science and Engineering: C*, vol. 103, article 109865, 2019.

[65] N. Torres-Martinez, C. Cretallaz, D. Ratel et al., "Evaluation of chronically implanted subdural boron doped diamond/CNT recording electrodes in miniature swine brain," *Bioelectrochemistry*, vol. 129, pp. 79–89, 2019.

[66] G. A. Snook, P. Kao, and A. S. Best, "Conducting-polymer-based supercapacitor devices and electrodes," *Journal of Power Sources*, vol. 196, no. 1, pp. 1–12, 2011.

[67] A. R. Harris, S. Morgan, J. Chen, R. M. I. Kapsa, G. G. Wallace, and A. G. Paolini, "Conducting polymer coated neural recording electrodes," *Journal of Neural Engineering*, vol. 10, no. 1, article 016004, 2013.

[68] P. Zarrintaj, Z. Ahmadi, H. Vahabi, F. Ducos, M. R. Saeb, and M. Mozafari, "Polyaniline in retrospect and prospect," *Materials Today: Proceedings*, vol. 5, no. 7, pp. 15852–15860, 2018.

[69] S. Lee, T. Eom, M. K. Kim, S. G. Yang, and B. S. Shim, "Durable soft neural micro-electrode coating by an electrochemical synthesis of PEDOT:PSS / graphene oxide composites," *Electrochimica Acta*, vol. 313, pp. 79–90, 2019.

[70] H. Zhou, X. Cheng, L. Rao, T. Li, and Y. Y. Duan, "Poly(3,4-ethylenedioxythiophene)/multiwall carbon nanotube composite coatings for improving the stability of microelectrodes in neural prostheses applications," *Acta Biomaterialia*, vol. 9, no. 5, pp. 6439–6449, 2013.

[71] C. Bodart, N. Rossetti, J.'. E. Hagler et al., "Electropolymerized Poly(3,4-ethylenedioxythiophene) (PEDOT) coatings for implantable deep-brain-stimulating microelectrodes," *ACS Applied Materials & Interfaces*, vol. 11, no. 19, pp. 17226–17233, 2019.

[72] X. Cui, V. A. Lee, Y. Raphael et al., "Surface modification of neural recording electrodes with conducting polymer/biomolecule blends," *Journal of Biomedical Materials Research*, vol. 56, no. 2, pp. 261–272, 2001.

[73] A. M. Cobo, C. E. Larson, K. Scholten et al., "Parylene-based cuff electrode with integrated microfluidics for peripheral nerve recording, stimulation, and drug delivery," *Journal of Microelectromechanical Systems*, vol. 28, no. 1, pp. 36–49, 2019.

[74] S. Biswas, D. Sikdar, D. Das, M. Mahadevappa, and S. Das, "PDMS based multielectrode arrays for superior in-vitro retinal stimulation and recording," *Biomedical Microdevices*, vol. 19, no. 4, p. 75, 2017.

[75] M. S. Nahvi, F. A. Boroumand, M. H. Maghami, A. M. Sodagar, A. Shojaei, and J. Mirnajafi-Zadeh, "Design, fabrication, and test of flexible thin-film microelectrode arrays for neural interfaces," in *2017 IEEE 30th Canadian Conference on Electrical and Computer Engineering*, Windsor, Canada, April 2017.

[76] W. F. Gillis, C. A. Lissandrello, J. Shen et al., "Carbon fiber on polyimide ultra-microelectrodes," *Journal of Neural Engineering*, vol. 15, no. 1, article 016010, 2018.

[77] Z. Shi, F. Zheng, Z. Zhou et al., "Silk-enabled conformal multifunctional bioelectronics for investigation of spatiotemporal epileptiform activities and multimodal neural encoding/decoding," *Advancement of Science*, vol. 6, no. 9, article 1801617, 2019.

[78] D. N. Heo, H. J. Kim, Y. J. Lee et al., "Flexible and highly biocompatible nanofiber-based electrodes for neural surface interfacing," *ACS Nano*, vol. 11, no. 3, pp. 2961–2971, 2017.

[79] C. Wang, W. Zheng, Z. Yue, C. O. Too, and G. G. Wallace, "Buckled, stretchable polypyrrole electrodes for battery applications," *Advanced Materials*, vol. 23, no. 31, pp. 3580–3584, 2011.

[80] T. S. Hansen, K. West, O. Hassager, and N. B. Larsen, "Highly stretchable and conductive polymer material made from poly(3,4-ethylenedioxythiophene) and polyurethane elastomers," *Advanced Functional Materials*, vol. 17, no. 16, pp. 3069–3073, 2007.

[81] R. Samba, T. Herrmann, and G. Zeck, "PEDOT-CNT coated electrodes stimulate retinal neurons at low voltage amplitudes and low charge densities," *Journal of Neural Engineering*, vol. 12, no. 1, article 016014, 2015.

[82] N. C. Foulds and C. R. Lowe, "Enzyme entrapment in electrically conducting polymers. Immobilisation of glucose oxidase in polypyrrole and its application in amperometric glucose sensors," *Journal of the Chemical Society, Faraday Transactions 1: Physical Chemistry in Condensed Phases*, vol. 82, no. 4, pp. 1259–1264, 1986.

[83] R. Janmanee, S. Chuekachang, S. Sriwichai, A. Baba, and S. Phanichphant, "Functional conducting polymers in the application of SPR biosensors," *Journal of Nanotechnology*, vol. 2012, Article ID 620309, 7 pages, 2012.

[84] R. A. Green, N. H. Lovell, and L. A. Poole-Warren, "Impact of co-incorporating laminin peptide dopants and neurotrophic growth factors on conducting polymer properties," *Acta Biomaterialia*, vol. 6, no. 1, pp. 63–71, 2010.

[85] C. M. Li, W. Chen, X. Yang et al., "Impedance labelless detection-based polypyrrole protein biosensor," *Frontiers in Bioscience*, vol. 10, no. 1-3, pp. 2518–2526, 2005.

[86] J. Park, S. Choi, A. H. Janardhan et al., "Electromechanical cardioplasty using a wrapped elasto-conductive epicardial mesh," *Science Translational Medicine*, vol. 8, no. 344, p. 344ra86, 2016.

[87] J. W. Costerton, L. Montanaro, and C. R. Arciola, "Biofilm in implant infections: its production and regulation," *The International Journal of Artificial Organs*, vol. 28, no. 11, pp. 1062–1068, 2005.

[88] D. H. Kim, Y. S. Kim, J. Amsden et al., "Silicon electronics on silk as a path to bioresorbable, implantable devices," *Applied Physics Letters*, vol. 95, no. 13, p. 133701, 2009.

[89] H. K. Makadia and S. J. Siegel, "Poly lactic-co-glycolic acid (PLGA) as biodegradable controlled drug delivery carrier," *Polymers*, vol. 3, no. 3, pp. 1377–1397, 2011.

[90] H. Tao, S. W. Hwang, B. Marelli et al., "Silk-based resorbable electronic devices for remotely controlled therapy and in vivo infection abatement," *Proceedings of the National Academy of Sciences of the United States of America*, vol. 111, no. 49, pp. 17385–17389, 2014.

[91] R. Feiner and T. Dvir, "Tissue-electronics interfaces: from implantable devices to engineered tissues," *Nature Reviews Materials*, vol. 3, no. 1, article 317076, 2018.

[92] P. R. Troyk, "Injectable electronic identification, monitoring, and stimulation systems," *Annual Review of Biomedical Engineering*, vol. 1, no. 1, pp. 177–209, 1999.

[93] G. Hong, T. M. Fu, M. Qiao et al., "A method for single-neuron chronic recording from the retina in awake mice," *Science*, vol. 360, no. 6396, pp. 1447–1451, 2018.

[94] T. Zhou, G. Hong, T. M. Fu et al., "Syringe-injectable mesh electronics integrate seamlessly with minimal chronic immune response in the brain," *Proceedings of the National Academy of Sciences of the United States of America*, vol. 114, no. 23, pp. 5894–5899, 2017.

[95] J. Liu, T. M. Fu, Z. Cheng et al., "Syringe-injectable electronics," *Nature Nanotechnology*, vol. 10, no. 7, pp. 629–636, 2015.

[96] G. Hong, T. M. Fu, T. Zhou, T. G. Schuhmann, J. Huang, and C. M. Lieber, "Syringe injectable electronics: precise targeted delivery with quantitative input/output connectivity," *Nano Letters*, vol. 15, no. 10, pp. 6979–6984, 2015.

[97] T. M. Fu, G. Hong, T. Zhou, T. G. Schuhmann, R. D. Viveros, and C. M. Lieber, "Stable long-term chronic brain mapping at the single-neuron level," *Nature Methods*, vol. 13, no. 10, pp. 875–882, 2016.

[98] T. G. Schuhmann Jr., J. Yao, G. Hong, T.-M. Fu, and C. M. Lieber, "Syringe-injectable electronics with a plug-and-play input/output interface," *Nano Letters*, vol. 17, no. 9, pp. 5836–5842, 2017.

[99] T. M. Fu, G. Hong, R. D. Viveros, T. Zhou, and C. M. Lieber, "Highly scalable multichannel mesh electronics for stable chronic brain electrophysiology," *Proceedings of the National Academy of Sciences of the United States of America*, vol. 114, no. 47, pp. E10046–E10055, 2017.

[100] R. D. Viveros, T. Zhou, G. Hong, T. M. Fu, H. Y. G. Lin, and C. M. Lieber, "Advanced one- and two-dimensional mesh designs for injectable electronics," *Nano Letters*, vol. 19, no. 6, pp. 4180–4187, 2019.

[101] K. V. Nemani, K. L. Moodie, J. B. Brennick, A. Su, and B. Gimi, "In vitro and in vivo evaluation of SU-8 biocompatibility," *Materials Science and Engineering: C*, vol. 33, no. 7, pp. 4453–4459, 2013.

[102] X. Dai, G. Hong, T. Gao, and C. M. Lieber, "Mesh nanoelectronics: seamless integration of electronics with tissues," *Accounts of Chemical Research*, vol. 51, no. 2, pp. 309–318, 2018.

[103] B. Tian, J. Liu, T. Dvir et al., "Macroporous nanowire nanoelectronic scaffolds for synthetic tissues," *Nature Materials*, vol. 11, no. 11, pp. 986–994, 2012.

[104] X. Yang, T. Zhou, T. J. Zwang et al., "Bioinspired neuron-like electronics," *Nature Materials*, vol. 18, no. 5, pp. 510–517, 2019.

[105] L. Luan, X. Wei, Z. Zhao et al., "Ultraflexible nanoelectronic probes form reliable, glial scar-free neural integration," *Science Advances*, vol. 3, no. 2, article e1601966, 2017.

[106] A. P. Alivisatos, A. M. Andrews, E. S. Boyden et al., "Nanotools for neuroscience and brain activity mapping," *ACS Nano*, vol. 7, no. 3, pp. 1850–1866, 2013.

[107] J. Rivnay, H. Wang, L. Fenno, K. Deisseroth, and G. G. Malliaras, "Next-generation probes, particles, and proteins for neural interfacing," *Science Advances*, vol. 3, no. 6, article e1601649, 2017.

[108] H. Tong, K. Lou, and W. Wang, "Near-infrared fluorescent probes for imaging of amyloid plaques in Alzheimer's disease," *Acta Pharmaceutica Sinica B*, vol. 5, no. 1, pp. 25–33, 2015.

[109] G. Kook, S. W. Lee, H. C. Lee, I.-J. Cho, and H. J. Lee, "Neural probes for chronic applications," *Micromachines*, vol. 7, no. 10, p. 179, 2016.

[110] H.-Y. Lai, L. D. Liao, C. T. Lin et al., "Design, simulation and experimental validation of a novel flexible neural probe for deep brain stimulation and multichannel recording," *Journal of Neural Engineering*, vol. 9, no. 3, article 036001, 2012.

[111] T. Kim, J. G. McCall, Y. H. Jung et al., "Injectable, cellular-scale optoelectronics with applications for wireless optogenetics," *Science*, vol. 340, no. 6129, pp. 211–216, 2013.

Hindawi
International Journal of Polymer Science
Volume 2019, Article ID 3160732, 14 pages
https://doi.org/10.1155/2019/3160732

Review Article

Functional Hydrogels and Their Application in Drug Delivery, Biosensors, and Tissue Engineering

Ke Wang[1], **Yuting Hao**[2], **Yingna Wang**[3], **Jinyuan Chen**[2], **Lianzhi Mao**[2], **Yudi Deng**[2], **Junlin Chen**[2], **Sijie Yuan**[4], **Tiantian Zhang**[5], **Jiaoyan Ren**[1], **and Wenzhen Liao**[2]

[1]*College of Light Industry and Food Sciences, South China University of Technology, Guangzhou 510640, China*
[2]*Department of Nutrition and Food Hygiene, Guangdong Provincial Key Laboratory of Tropical Disease Research, School of Public Health, Southern Medical University, No. 1023 South Shatai Road, Guangzhou 510515, China*
[3]*Guangzhou Sanxing Biotechnology Co. Ltd., No. 14, Shayuan Shang Street, Sixian Village, Xinzhuang Town, Panyu District, Guangzhou 511436, China*
[4]*Department of Endocrinology, The Third Affiliated Hospital, Southern Medical University, Guangzhou 510630, China*
[5]*College of Food Science and Engineering, Ocean University of China, No.5 Yushan Road, Qingdao 266003, China*

Correspondence should be addressed to Tiantian Zhang; ttzhang89@hotmail.com, Jiaoyan Ren; jyren@scut.edu.cn, and Wenzhen Liao; wenzhenliao@163.com

Received 23 May 2019; Accepted 6 July 2019; Published 7 October 2019

Guest Editor: Lin Zhang

Hydrogel is a new class of functional polymer materials with a promising potential in the biomedical field. The purpose of this article is to review recent advancements in several types of biomedical hydrogels, including conductive hydrogels, injectable hydrogels, double network hydrogels, responsive hydrogels, nanocomposite hydrogels, and sliding hydrogels. In comparison with traditional hydrogels, these advanced hydrogels exhibit significant advantages in structure, mechanical properties, and applications. The article focuses on different methods used to prepare advanced biomedical hydrogels and their diversified applications as drug delivery systems, wound dressings, biosensors, contact lenses, and tissue replacement. These advances are rapidly overcoming current limitations of hydrogels, and we anticipate that further research will lead to the development of advanced hydrogels with ubiquitous roles in biomedicine and tissue replacement and regeneration.

1. Introduction

Hydrogels are a class of polymers having a three-dimensional network structure formed through physical and chemical cross-linking of monomers with a hydrophilic group [1]. Hydrogels swell when they absorb large volumes of water yet maintain their original structures without being dissolved [2, 3] (Figure 1). In the biomedical field, hydrogels are a new class of functional polymer materials with enormous potential in biotechnology. When the polymer network is encased in water, the material absorbs the water and adopts fluidic properties, which is very similar to what occurs with tissues in the human body [4, 5]. In the presence of water, the surfaces of the hydrogels become wet and malleable. And because of these properties, couple with the stable organization of the material significantly reduces irritation to the surrounding tissues and improves biocompatibility [6]. Additionally, hydrogels will not affect the metabolic processes of living organisms and metabolites can pass freely through the hydrogels. Hydrogels are also sensitive to small changes in external stimuli, such as temperature, pH, ionic strength, electric fields, and magnetic fields, and can respond to these stimuli through volume swelling or shrinking [7–11]. Therefore, hydrogels are more similar to living tissues, specifically the outer membrane of the cell matrix, than any other currently known synthetic biomaterials and these properties result in reducing friction and mechanical effects on the surrounding tissues, which significantly improves the biological properties of the material [12].

Hydrogels have been one of the greatest interests to biomaterial scientists since the pioneering work of Wichterle

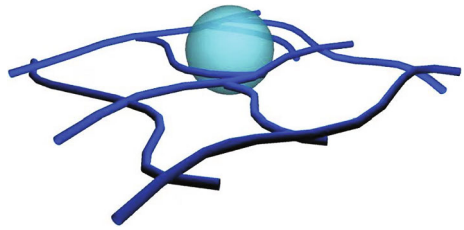

Figure 1: The sketch map of the hydrogel network.

and Lim in 1960 on cross-linked HEMA (hydroxyethyl methacrylate) hydrogels, which has led to the development of materials with excellent water absorption, high water retention, good biocompatibility, biodegradability, limited or minimal toxicity, and simplified synthesis methods. These materials are now widely used in biomedicine, functioning as tissue fillers, drug delivery agents, contact lenses, and tissue engineering scaffold materials [12–14]. Because hydrogels produce huge economic and social benefits, the research, the development, the application, and the production of hydrogels represent an important area of the biomaterial field.

Traditional hydrogels are typically formed by chemical cross-linking. Nonuniform dispersion of a chemical cross-linking agent results in a nonuniform gel network, and the resulting gel is very weak and fragile, greatly limits its application [15]. To overcome mechanical limitations in traditional gels, four major types of novel network structures have been investigated, as follows: (i) the replacement of covalent cross-linking points by active cross-linking sites, which can reduce the stress concentration and the network structural damage caused by the uneven distribution of covalent bonds. Representative studies include "Slide-Ring" hydrogels, in which "8"-shaped polyrotaxane as a crosslinking point, polymer chains pass through the cross-linking agent from its upper and lower cavities [16]. The molecular chains distribute stress more uniformly across the gel network through positional adjustment in the external force. (ii) The introduction of a "sacrifice key" within the structure of certain hydrogels (e.g., double network hydrogels), which is a region designed to break and absorb energy that can improve the strength and resilience of the materials [17]. These hydrogels are mainly composed of two interpenetrating or semi-interpenetrating networks with different properties. Under stress, the first network absorbs energy to burst, endowing hydrogels with high strength and toughness, while the second network is loosely cross-linked and is more difficult to destroy, which maintains the integrity of hydrogels [3]. (iii) Nanoparticles as giant multifunctional cross-linking points, where polymer chains are cross-linked into a three-dimensional network by physical adsorption or chemical bonding [18]. The physical adsorption between the molecular chains and nanoparticles can dissipate energy to improve the mechanical properties of hydrogels, while conversely, the high specific surface area and high modulus of nanoparticles themselves strengthen the hydrogels [19]. (iv) Polymers constructed via noncovalent interactions and supramolecular self-assembling structures, producing hydrogels that are strong, resilient, and responsive to changing stimuli [20]. Consequently, the objective of this review is to evaluate recent research and progress aimed at developing novel high-performance, intelligent hydrogel materials for biomedical applications.

2. Main Types of Hydrogels

2.1. Conductive Hydrogels. Conductive hydrogel (CH) is a new effective material which has the similar unique properties to traditional hydrogels and an additional benefit in electrical conductivity [21–23]. It was first proposed by Gilmore et al. [24], and in recent years, more attention has been given in the exploitation and application of CHs. Depending on the different additives, the CHs are divided into two categories: (i) the CHs-based conducting polymers (CPs) and (ii) the CHs-based metallic nanoparticles. Mostly, the CH is defined as a hybrid network made by cross-linked soft hydrogels and CPs [25]. Although CP is not metallic, it has extraordinary electrical conductivity that can change the final hydrogels in structural and electrical properties to a considerable extent [26–31]. The use of CPs enables hydrogels to stimulate electricity locally and enhance the physical properties of hydrogels to accurately control the extent and duration of external stimulation [32, 33]. The microscopy allows the microstructure magnified, and it always be used to observe the microstructure of the hydrogel, such as atomic force microscopy, which can not only observe the microstructure of objects [34, 35] but also the conductivity of the conductive hydrogel that can be detected by conducting probe atomic force microscopy [36]. Nowadays, the most familiar CPs like polypyrrole (PPY), polythiophene (PT), poly(3,4-ethylene dioxythiophene) (PEDOT), and polyaniline (PAni) are widely used in biomedical science to promote cell growth and proliferation [37, 38]. Besides, the natural polymers such as alginate, starch, chitosan, and their derivatives also have been considered as CPs in different conditions and because of the characteristics of these natural polymers, the final hydrogels are extremely beneficial to biodegradable and biocompatible. Till now, the CPs has gained lots of scientific responsiveness and they have extensively applied in batteries, sensors, semiconductor devices, electronic and optoelectronic devices, and so on [39–43]. Similar to the CPs mentioned before, the metallic nanoparticles give the CH synergistic properties combined with the metal and hydrogel matrix [44, 45]. And since the performance of the hydrogels has improved the homogeneous distribution and long-term cytotoxicity of metallic nanoparticles, more applications of final hydrogels are being developed in the field of biomaterials.

A number of routes have explored to the preparation of CHs, but all of them can be summarized as two types: preparation of single component CHs and preparation of multicomponent CHs. Single-component CHs are defined as a stable conjugate-combined conductive polymer with small hydrophilic molecule through electrostatic interaction or cross-linked by substitutes of small molecular. According to the electrostatic interaction between the positive charges on PAni with the phosphate on phytic acid, the final hydrogel has better characteristics in capacitance (~480 $F \cdot g^{-1}$), higher sensitivity (~16.7 $\mu A \cdot mM^{-1}$), and faster response time (~0.3 s) in the glucose sensing test [46]. The common

methods to prepare multicomponent CHs are electrochemical polymerization and chemical oxidation polymerization; the latter usually includes one-step facile strategy and two-step sequential preparation method. The one-step facile strategy refers to the cross-linked hydrogels obtained by the chemical reaction of CPs and hydrophilic polymer mixture. PPY has poor water solubility, but the PPY/agarose CH can get by this route when PPY is added to aqueous solution of agarose and cupric chloride is added to the solution to oxidize PPY [47, 48]. The two-step sequential preparation method is more complex; the extra step is the monomers of CPs which permeate into hydrophilic polymer hydrogels. The preparation of PPY conductive hydrogel can also use the two-step method, incorporation of pyrrole monomer and silver nanoparticles first, and then oxidation of pyrrole with ferric ion, and it is surprising to find that the final CHs are beneficial to thermostability, uniform mesh structure, and mechanical property (storage modulus 10 kPa) [49]. Generally, because a one-step facile strategy has the advantages of simple operation, energy saving, and environmental protection while the two-step sequential preparation method needs the step of incorporation because the final hydrogels are not uniform, the former will be the main research direction of the CH preparation in the future.

2.2. Injectable Hydrogels. Injectable hydrogels are characterized by an intrinsic fluidity and can be applied by an injection method. In response to external stimuli (e.g., temperature or pH changes), injectable hydrogels exhibit sol-gel phase transitions [50]. Moreover, compared with conventional hydrogels, injectable hydrogels are more effective for minimally invasive applications. This not only expands the scope of its application in the biomedical field but also improves the comfort satisfaction of patients and reduces the cost of application to a certain extent [51, 52]. Based on the methods used for development, injectable hydrogels can be divided into two categories: light irradiation hydrogels and self-assembling hydrogels [53, 54]. Light irradiation hydrogels involve the formation of irreversible covalent bonds through the application of visible or ultraviolet light radiation, while self-assembling hydrogels are formed spontaneously or after directional initiation [52, 55].

Many injectable hydrogels with different properties have been prepared using the above two gelation methods. Injectable hydrogels made of dextran methacrylate (DEX-MA) and scleroglucan (Scl) can be formed by UV irradiation using a photoinitiator, and the resulting gels reportedly exhibited adequate mechanical properties, suitable for biomedical applications [56]. Novel injectable photochemical hydrogels are composed of gellan gum methacrylate (GG-MA) and polyethylene glycol dimethacrylate (PEG-DMA) and have also been synthesized by irradiation with a UV lamp for 30 min [57], and the resulting hydrogels exhibited better mechanical properties than those composed of GG-MA alone. Interestingly, the strength is significantly enhanced by the concentration and the molecular weight of PEG-DMA used to construct the new network [57]. The methods of self-assembling hydrogels include enzyme-induced gelation, chemical cross-linking with complementary groups, and ionic interactions. The injectable porous hydrogels have been widely used in biomedical applications due to their excellent permeability and ease of integration into sites of surgical intervention. For example, Yom-Tov et al. developed a method that enables the *in situ* formation of pores with tailored porosity and pore size, by encapsulating oil droplets in the hydrogel using an emulsion templating technique and then leaching the droplets out of the gel to create the porous structures [58]. The oil-to-water ratios and the surfactant concentrations were adjusted to vary pore size and porosity, and this method produced bioactive hydrogels exhibiting good mechanical strength, water absorbency, and diffusive properties, useful for biomedical applications [58].

2.3. Double Network Hydrogels. Double network (DN) hydrogels comprise two interpenetrating polymer networks; one of which is a highly cross-linked rigid polymer network, while the other is a lightly cross-linked flexible polymer network [59]. While this structure is connected through physical entanglement, no chemical cross-linking occurs between these two mutually independent cross-linked networks [60]. Hydrogels exhibit a certain viscous flow due to the loose cross-linking of the second network, which can effectively absorb the fracture energy through the network deformation and/or the slippage of physical entanglements along the polymer chain. This prevents cracks from propagating across the structure, so DN hydrogels have good mechanical strength [61]. In addition to greater mechanical strength, DN hydrogels have several other advantages over hydrogels with a single network structure, such as the degree of cross-linking is easier to control and increased drug loading capacity [62].

Early DN hydrogels were mainly composed of covalent bonds, but when covalent networks are destroyed by stress, hydrogels become increasingly elastic and will permanently lose their energy dissipation mechanisms [63]. In recent years, a series of DN hydrogels have been developed that introduce noncovalent (*e.g.*, ions or hydrogen bonds) "sacrifice units" [64, 65] that exhibit high strength and durability [66, 67]. The noncovalent interactions are often dynamic and reversible. When they are introduced into the hydrogels, the noncovalent "sacrifice units" may be destroyed from energy dissipation due to stress [68], then reunited to rebuild the network structure once the stressor has been removed, thus restoring the original strength and toughness of the gel [65]. For example, a novel double network hydrogel (IPN hydrogels) was fabricated by combining cellulose and poly(N-isopropyl acrylamide), in which cellulose hydrogels were employed as the first network (Figure 2(a)), while the second network was comprised of monomeric N-isopropylacrylamide, N,N′-methylene bis-acrylamide as a cross-linker, and ammonium persulfate as an initiator (Figure 2(b)) [69]. The two networks were subsequently integrated through a polymerization reaction at 35°C (Figure 2(c)), and the resulting DN hydrogel exhibited uniform porous structure, while its mechanical and swelling properties were strongly dependent on the weight ratio of two networks [69]. In a different study, an extremely stretchable and tough hydrogel was synthesized by mixing ionically cross-linked alginate and covalently cross-linked polyacrylamide [70]. The alginate

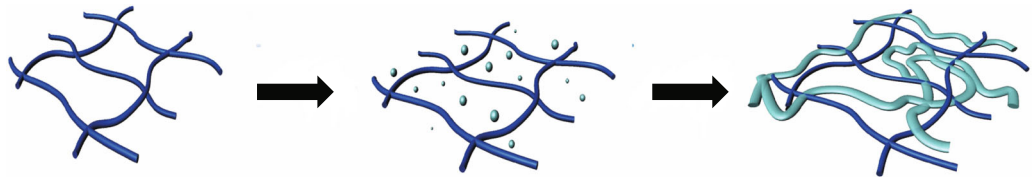

Figure 2: Schematic illustration of the fabrication process of IPN hydrogels.

Table 1: Stimulating and responsive factors of smart hydrogels.

Type	Stimulating factors	Responsive group or substance
Temperature-sensitive	Temperature	N-Isopropylacrylamide
pH-sensitive	pH	-COOH, -HSO_3, -NH_2
Light-sensitive	Light	Cinnamoyl-, azobenzene, O-nitrobenzyl alcohol
Electricity-sensitive	Electricity	Carbonyl-, nitro-, alkyl group

chain was comprised of mannuronic acid (M unit) and guluronic acid (G unit) connected by glycosidic linkages. In an aqueous solution, the G blocks were able to chelate divalent cations (e.g., Ca^{2+}) to form ionic cross-links. These initial Ca^{2+}-cross-linked alginate hydrogels exhibited limited stretching capabilities and could rupture when stretched beyond 1.2 times its original length. However, subsequent research reported that *in situ* polymerization combining the Ca^{2+}-cross-linked alginate hydrogel skeleton with an acrylamide monomer to form an interpenetrating network structure greatly improved the tensile toughness and strength of hydrogels, thus increasing its tensile breaking length up to 23 times the original length [70].

2.4. Responsive Hydrogels. Hydrogels with responsive performance have a broad range of potential applications in biological tissue engineering, including drug delivery and controlled release, artificial muscles, sensors, and enzyme catalysis [71–73]. When environmental changes (*e.g.*, external temperature, pH, light, electric field, and salinity) occur, hydrogels can shrink or swell as needed due to the introduction of hydrogen bonds, ions, complexation, electrostatic interactions, and other noncovalent interactions [74]. These responsive "smart" or intelligent hydrogels were first developed by Katchalsky in 1949, by copolymerizing methacrylic acid with a low percentage of divinyl benzene, producing a gel capable of absorbing hundreds of times its own weight of water at higher pH values, then gradually shrinking with decreasing pH [75]. Significant progress has been made since then, and currently, responsive hydrogels can be classified (Table 1) based on responses to different stimuli as being temperature-sensitive, pH-sensitive, light-sensitive, or electricity-sensitive [76, 77].

The most common intelligent hydrogels are temperature-sensitive, particularly those comprised of N-isopropyl acrylamide [78], where interactions between hydrophilic amide groups and hydrophobic isopropyl groups can produce structural changes in the hydrogel [79]. A novel polymer network was obtained by the introduction of the extracellular glucan salecan into a poly(N-isopropylacrylamide) (PNIPAm) network, resulting in a thermosensitive hydrogel possessing good mechanical properties and high water absorption at room temperature [80]. Moreover, the salecan/PNIPAm hydrogels were nontoxic and exhibited good biocompatibility, making them suitable for biomedical applications [80]. N,N-Diethylacrylamide has also been found to exhibit temperature sensitivity [81]. Hoffman has synthesized a series of thermo- and pH-sensitive poly(vinyl alcohol)/poly(N,N-diethylacrylamide-co-itaconic acid) (PVA/P(DEA-co-IA)) semi-interpenetrating polymer network (semi-IPN) hydrogels by radical polymerization and semi-IPN technology [1]. The obtained semi-IPN hydrogels possessed unconventional thermosensitive properties, such as faster deswelling rates and slower swelling rates in response to an alternation of temperature, and outstanding mutative values in response to pH value change [1].

Smart hydrogels capable of responding to pH changes have also been developed by incorporating ionizable acidic or basic groups (*e.g.*, carboxyl, sulfonic acid, or amino groups) in the preparation process [82–84]. Dissociation or association of these groups is affected by the pH value, which can alter either the internal network structure of the hydrogels or the affinity/hydrophobicity of the molecular chains, thereby altering the water absorption capacity of the gel [85]. A novel pH-sensitive hydrogel with excellent mechanical strength was prepared using oligomonomers of poly(ethylene glycol) methyl ether methacrylate (PEGMA) and poly(acrylic acid) (PAA) [86]. When immersed in solutions with a pH below ~4, the hydrogels exhibited a low swelling ratio with a compression strength of ~8 MPa, while in solutions with a pH > 4, the hydrogels were transparent and exhibited a high swelling ratio with a compression strength of ~1 MPa. The robust nature of these hydrogels over a wide pH range may be useful for applications such as artificial muscles and controlled release devices.

Moreover, dual or multiple smart hydrogels may be prepared by combining two or more responsive hydrogel types using interpenetrating network connection or a graft

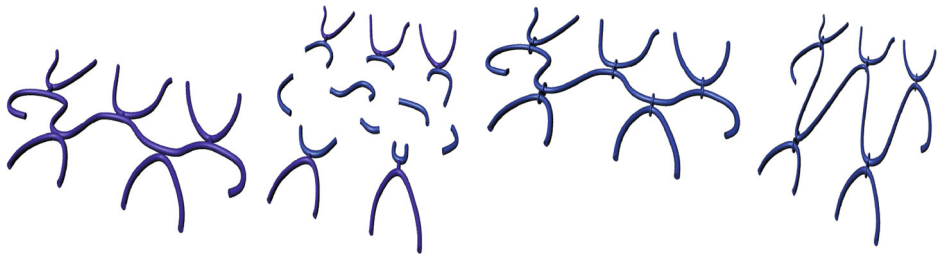

(a) General chemistry hydrogel (b) Sliding hydrogel

Figure 3: General chemistry hydrogel and sliding hydrogel.

copolymerization method, among other approaches. For example, a new kind of multiple stimulus-responsive organic/inorganic hybrid hydrogel was successfully fabricated by combining a dual stimuli-responsive poly(2-(2-methoxyethoxy)ethyl methacrylate-co-oligo(ethylene glycol)methacrylate-co-acrylic acid) (PMOA) hydrogel with magnetic attapulgite/Fe_3O_4 (AT-Fe_3O_4) nanoparticles [87]. The resulting AT-Fe_3O_4/PMOA hydrogels presented temperature/pH sensitivity, good mechanical properties, and magnetic functionality, allowing them to continue to swell under an alternating magnetic field following equilibrium swelling in deionized water [87].

2.5. Nanocomposite Hydrogels. The nanoscale dispersion of different materials in the polymeric matrix form nanocomposite hydrogels, with particle sizes ranging from 1 to 1000 nm, and the molecular chain structure consists of branched polymers and cross-linked network polymers [21]. This uniform dispersion of inorganic components can greatly improve the strength of hydrogels [19]. Nanocomposite hydrogels are also known as hybrid hydrogels, which are formed by physical or chemical covalent cross-linking of the polymer network with raw material particles, including carbon-based nanoparticles, polymeric nanoparticles, inorganic/ceramic nanoparticles, or metal/metal oxides [19, 21, 88–90].

Yadollahi et al. reported the synthesis of carboxymethyl cellulose/ZnO nanocomposite hydrogels by *in situ* formation of ZnO nanoparticles within swollen carboxymethyl cellulose hydrogels [91]. The resulting nanocomposite hydrogels exhibited both pH- and salt-sensitive swelling behaviors. In addition, they exhibited increased swelling in different aqueous solutions compared with neat hydrogels. The presence of the inorganic salt can weaken hydrogen bonding between the polymer chains and water, resulting in a localized dehydration of the polyphosphate ester and thus increasing aggregation. Based on this approach, a novel biodegradable nanoscopic hydrogel was synthesized by photocross-linking salt-induced polymer assemblies [92]. This method was based on the integration of block copolymers containing polyphosphoester (poly(ethyl ethylene phosphate) (PEEP)), which could undergo a salt-induced hydrophobic-to-hydrophilic transition. A triblock copolymer of poly(ethylene glycol) (PEG) combined with PEEP was synthesized, and its end groups were then functionalized with acryloyl chloride to produce an acrylate block copolymer (Acr-PEEP-PEG-PEEP-Acr). Subsequently, a diblock copolymer of PEG and PEEP (Acr-PEEP-PEG-Lac) containing heteroacrylate and lactosyl end functional groups was also synthesized to incorporate targeting moieties into the nanogel. These block copolymers were found to be soluble in water but self-assembled into core-shell structural nanoparticles following the addition of salt. The resulting nanoparticles could become totally hydrophilic after UV cross-linking to anchor the structure and dialysis to remove salt, generating nanogel particles with an inner reservoir for water-soluble drugs. This synthesis method is both facile and biocompatible, which could waive the inconvenient purification requirements typically required following nanogel generation [92].

2.6. Sliding Hydrogels. Sliding hydrogels contain topologically interlocked noncovalent cross-links that can slide along a threaded polymer backbone [93]. A novel sliding hydrogel, pseudopolyrotaxanes of monothiolated beta-cyclodextrin threaded on poly(allyl glycidyl ether)-block-poly(ethylene glycol)-block-poly(allyl glycidyl ether), was previously prepared in water by sonication and subsequently photocross-linked by UV irradiation, resulting in a sliding hydrogel with elasticity comparable to other hydrogels, increased stretchability, and tunable degradability under acidic conditions [16]. The benefit of these hydrogels lies in their more stable mechanical properties, as common hydrogels exhibit greater volatility under a smaller strain range. Research suggests that the mechanical strength of sliding hydrogels can adapt to the strength of mammal skin, blood vessels, and tissues; therefore, the sliding hydrogels could be used as a substitute for a variety of biological materials. Additionally, the stimulation sensitivity of sliding hydrogels may be improved by modifying cyclodextrin rings with the addition of sensitive groups [94, 95]. For example, a novel photosensitive sliding hydrogel was prepared by adding azobenzene units to the mobile α-cyclodextrin units of a poly(ethylene oxide)-based polyrotaxane and its photoresponsive behavior was attributed to the dynamic nature of the cross-linkers [96].

In summary, there are three primary factors that determine the performance of sliding hydrogels: the number of rings on each polymer chain, cross-linking density, and swelling properties of the hydrogels in solvents [97]. In conventional gels, the chain length between cross-linking points is uneven and the shorter chains may break more readily due to unequal chain tension under external force (Figure 3(a)). Conversely, in sliding gels, the chain length between cross-linking points is relatively uniform due to free slide of

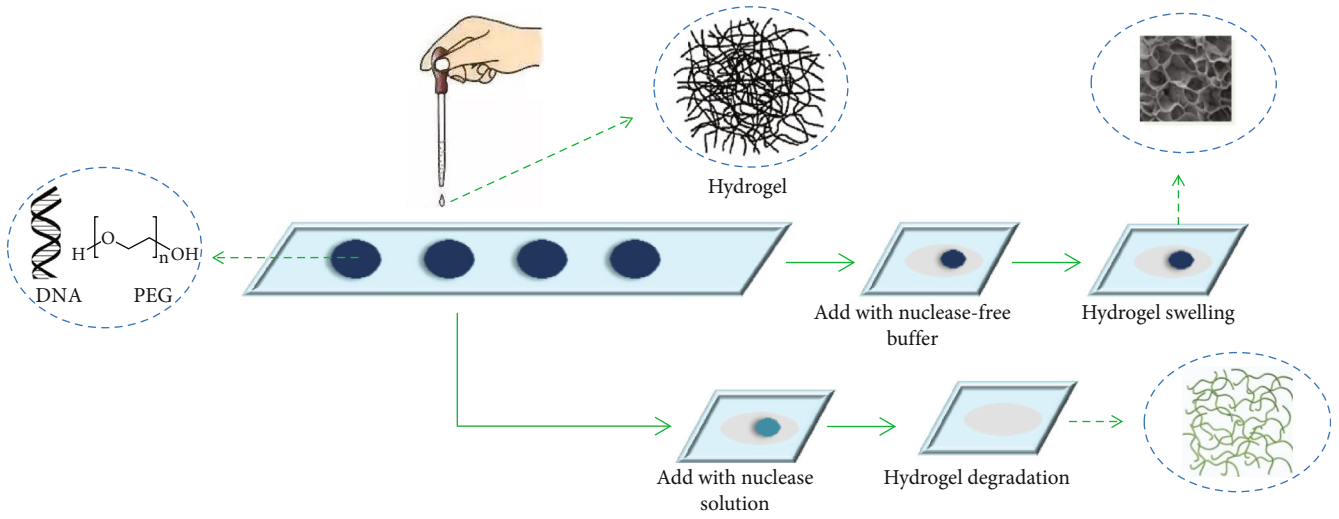

Figure 4: Hydrogel network formation via copper-free click chemistry, followed by hydrogel swelling when immersed in nuclease-free buffer or biodegradation when incubated in the presence of nucleases.

cross-linked rings under external force, so these hydrogels exhibit higher mechanical strength than conventional gels (Figure 3(b)).

2.7. Other Novel Hydrogels. In addition to the five biomedical hydrogels cited above, research has led to the development of a number of other novel hydrogels, including DNA-enabled hydrogels, and magnetic hyaluronate hydrogels [98, 99]. DNA-enabled hydrogels have been synthesized through the reaction of dibenzocyclooctyne-functionalized multiarm poly(ethylene glycol) with azide-functionalized single-stranded DNA in aqueous solutions by copper-free click chemistry (Figure 4) [98]. Besides, the hydrogel contained with the adipose-derived stem cells has been reported that can augment diabetic wound healing [100]. These gels can be degraded by nucleases and may be modified for use in a variety of applications, such as drug delivery and wound healing systems. These research efforts will continue to drive the development of novel hydrogels with increased sensitivity to the area of changing environmental conditions, improving strength, elasticity, and capability of novel hydrogels; all of which can further enhance their critical roles in biomedicine.

3. Applications of Hydrogels

3.1. Applications in Drug Delivery Systems. In recent years, drug delivery systems capable of controlled dosage delivery for extended periods in the affected area have been vigorously developed all over the world [101]. An effective drug delivery system has three critical requirements of the structure: a region for drug storage, a controlled release rate, and a release drive [102]. Hydrogels exhibit these three functions. Moreover, hydrogels can mask the bitter taste and odor of pharmaceuticals. Thus, hydrogels have a great potential for application via oral, nasal, buccal, rectal, vaginal, eye, injection, and other administration routes. When the hydrogel is injected or transplanted into an organism, it can maintain the effective and controlled release of an embedded drug into body fluids [103]. The therapeutic effects of many lipophilic drugs are limited due to a variety of problems including poor solubility, poor dispersion, lack of uniformity, poor dissolution, low bioavailability, and lack of *in vivo* stability. However, when these drugs are uploaded to a hydrogel system, the above defects can be improved to some extent, resulting in solubilization, sustained release or controlled release effects, and enhanced stability and bioactivity. Conversely, small molecule drugs that are highly soluble exhibit more advantages, including improved absorption and high bioavailability, but these properties are incompatible with sustained drug delivery effects. To exploit these more desirable properties, a novel interpenetrating polymer network was synthesized through the modification of silicone elastomers with a poly(2-hydroxyethyl methacrylate) (PHEMA)-based hydrogel characterized by a surface-connected hydrophilic carrier network inside the silicone [104]. These structures were then loaded with the antibiotic ciprofloxacin, and the resulting drug release inhibited bacterial growth when placed on agar, suggesting that these hydrogels have potential for future applications in drug-releasing medical devices [104]. Additionally, floating hydrogels synthesized from kappa carrageenan containing either $CaCO_3$ or $NaHCO_3$ as pore forming agents have been evaluated with amoxicillin trihydrate as a model drug [105]. The hydrogels incorporating $CaCO_3$ exhibited higher drug entrapment efficiency and longer sustained drug release than $NaHCO_3$, indicating that $CaCO_3$ is a viable pore-forming agent for the development of an effective floating drug delivery system [105]. Interestingly, because of the distinctive conductivity of the conducting hydrogel, they are also electrostimulated drug release devices and these devices have great advantages in low-voltage drive and high load capacity [106]. Based on the conductive polymer poly(3-methoxydiphenylamine) and pectin hydrogels, Mongkolkitikul et al. synthesize a drug delivery system to transport ibuprofen. And the study showed that under applied electric potential, the diffusion coefficient of a

drug is much higher than those without electric potential due to the mesh size expansion [107].

Hydrogels can also be used as a carrier for biological macromolecular drugs, mainly due to the controlled release behavior of protein drugs in polymer systems. For example, hydrophilic and hydrolytically degradable poly(ethylene glycol) (PEG) hydrogels were prepared *via* Michael-type addition, which were employed for sustained delivery of a monoclonal antibody against the protective antigen of anthrax. Burst release of the antibody from the matrix was avoided due to the PEG-induced precipitation. These hydrogels were able to release active antibodies in a controlled manner, for up to 56 days *in vitro*, by varying the polymer architectures and molecular weights of the precursors. Analyses of the secondary and tertiary protein structures and the *in vitro* activity of the released antibody indicated that the encapsulation and release of the drug did not affect the protein conformation or functionality, which suggested that this is a promising approach for developing PEG-based carriers capable of sustained release of therapeutic antibodies against toxins in various applications [108]. Similarly, novel disc-shaped hydrogel nanoparticles have been prepared by fragmentation of stearoyl macrogol-32 glycerides (Gelucire 50/13) hydrogels, and the resulting nanoparticles exhibited good physical stability due to their outer coating of PEG [109]. Moreover, these nanoparticles exhibited good loading capacity for hydrophilic macromolecules (such as lysozyme) mainly *via* surface adsorption, indicating their potential as effective nanocarriers for drug delivery (Figure 5).

In addition, several studies have reported the use of hydrogels as carriers for polysaccharide substances and genes. A novel high-strength photosensitive hydrogel was formed by the photoinitiated copolymerization of hydrophilic hydrogen bonding monomer (acrylamide (AAm)), hydrophobic hydrogen bonding monomer (2-vinyl-4,6-diamino-1,3,5-triazine (VDT)), and a spiropyran-containing monomer, in the presence of the cross-linker poly(ethylene glycol) diacrylate. Reverse gene transfection was then successfully accomplished by anchoring the PVDT/pDNA complex nanoparticles on the gel surface through hydrogen bonding between diaminotriazine motifs prior to cell seeding [110]. Interestingly, the gene transfection level could be further increased by fibronectin modification combined with the supplementation of PVDT/pDNA complex nanoparticles after the first cycle of reverse gene transfection (*i.e.*, sandwich gene transfection) [110].

3.2. Applications in Wound Dressings. Hydrogel materials have been used directly in contact with human tissues, absorbing exudate to form a gel, which effectively prevents the loss of body fluids and is not subject to adhesion on the wound after absorption of exudate [111]. Hydrogels can also deliver oxygen to the wound to accelerate the growth of epithelial cells and proliferation of new capillaries [112, 113] and can protect the wound from bacterial violations, inhibiting bacterial growth and thus promoting wound healing in general [114]. There is an unmet clinical need for wound dressings, and currently, hydrogel materials for wound dressings have entered the commercial market. These hydrogel materials can be made of spray, emulsion, or paste, with embedded anti-inflammatory drugs that can be slowly released through the gel to the injured area, which can accelerate wound healing. A class of "smart" peptide hydrogels was prepared by self-assembling of ultrashort aliphatic peptides into helical fibers, and these nanofibrous hydrogels reportedly accelerated wound closure in a rat model for partial thickness burns [115]. The regenerative properties could be further enhanced by incorporation of bioactive moieties such as growth factors and cytokines. Singh et al. reported the development of a novel hydrogel combining silver nanoparticles and polyvinyl pyrrolidone (PVP) blended with carrageenan via gamma irradiation, which could be used as wound dressings to control infection and facilitate the healing process for burns and other skin injuries [116].

3.3. Applications in Biosensors. The biosensor is a fast, accurate, and real-time detection means. Biomolecules generally are fixed either on the surface or the interior of hydrogels, connecting to the physical elements of the biosensors. The hydrogel film is the hub connecting the biomolecules and physical components. Hydrogels prepared for sensors are typically comprised of alginate, alginic acid in complex with chitosan, acrylamide, or N-isopropyl acrylamide [117–121]. A nonenzymatic electrochemical H_2O_2 sensor was prepared by *in situ* fabrication of biocompatible chitosan hydrogels containing a specific recognition molecule for H_2O_2, and this sensor exhibited a fast amperometric response to H_2O_2 within 7 s. The remarkable analytical performance of the nonenzymatic electrochemical sensor represents a promising model for durable monitoring of H_2O_2 in rat brain microdialysates, which will improve our ability to understand the biological effects of H_2O_2 on pathological and physiological processes [122]. Similarly, Devadhasan and Kim introduced a new method to quantify various pH solutions with a complementary metal oxide semiconductor image sensor, which produced high-accuracy analyses based on pH measurement [123]. In this approach, a thin film was fabricated by merging a pH indicator with the hydrogel matrix and the modified gel exhibited color change development across the full spectrum of pH (pH 1–14).The complementary metal oxide semiconductor image sensor then absorbed the color intensity of the hydrogel film, and the hue value was converted into digital data with the help of an analog-to-digital converter to determine the pH ranges of solutions [123]. This gel may be useful for *in situ* pH sensing in the presence of toxic chemicals and chemical vapors.

3.4. Applications in Contact Lenses. Contact lenses are delicate ophthalmic medical tools for correcting vision or changing eye color for aesthetic effects, and their permeability and biocompatibility are key properties to be considered during design. Hydrogel contact lenses must be comfortable to wear, have good oxygen permeability, and potentially have the capacity to assist in the treatment of eye diseases, which is the reason why hydrogels represent important manufacturing materials for contact lenses [124]. The majority of soft contact lenses are comprised of poly(2-hydroxyethyl methacrylate) hydrogels cross-linked with

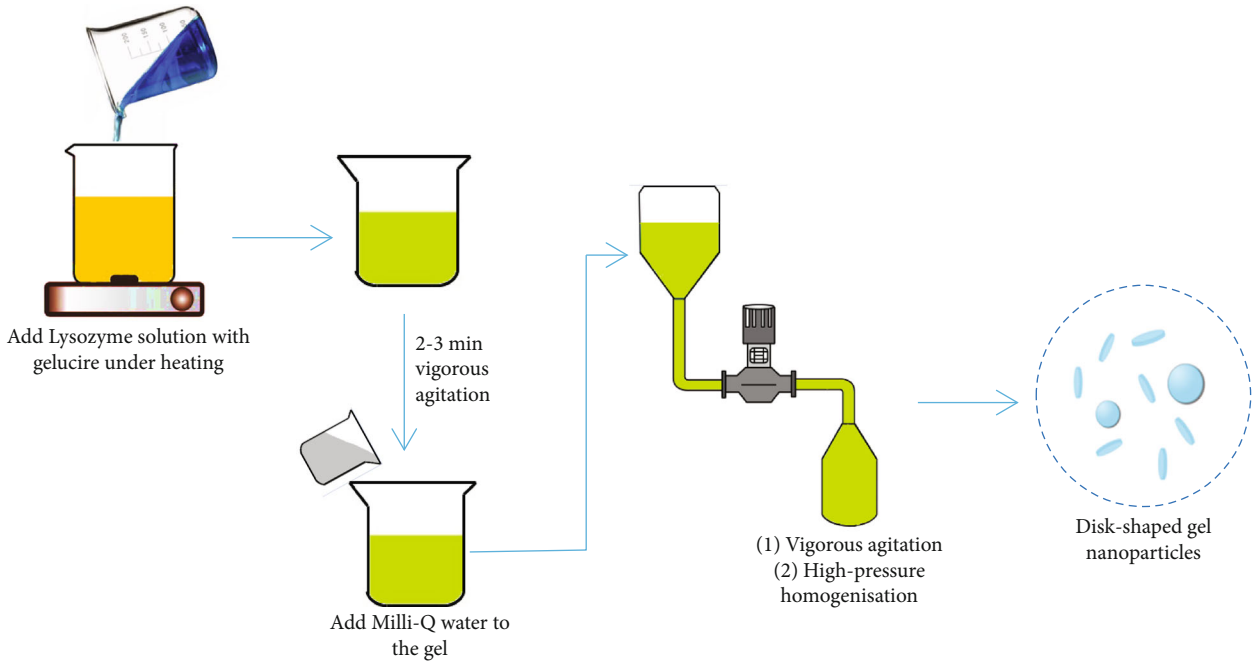

Figure 5: Schematic illustration of the fabrication process of lysozyme-loaded disc-shaped gel nanoparticles.

ethylene glycol dimethacrylate or silicone [125]. Poly(2-hydroxyethyl methacrylate) hydrogels have several advantages: relatively high water content, thermal and chemical stability, tunable mechanical properties, and oxygen permeability, which are very important for safe daily wear [126]. Poly(2-hydroxyethyl methacrylate) (p(HEMA)) soft contact lenses have been prepared by thermal or photopolymerization of HEMA solutions containing ethylene glycol dimethacrylate as the cross-linker and different proportions of N-vinyl-2-pyrrolidone or methacrylic acid as comonomers [127]. The drug loading capacity and release properties of p(HEMA)-based soft contact lenses were improved based on the optimization of the hydrogel composition and microstructural modifications using water during the polymerization process [127].

3.5. Applications in Tissue Engineering. The objective of tissue engineering research and development is to produce biological alternatives to restore, maintain, or improve the morphology and function of damaged tissues and organs, thereby achieving reconstruction by applying principles and methods from both cell biology and engineering [128]. Tissue engineering has also been defined as "regenerative medicine." Specifically, donor cells, after amplification *in vitro*, are seeded for growth onto a biodegradable three-dimensional scaffold. The resulting complex can then be implanted into the body or at targeted sites, where the implanted cells continue to proliferate and secrete an extracellular matrix [129]. As the scaffold degrades, new tissues or organs will form bearing the same shape and function as the damaged tissues or organs. Tissue engineering represents an extraordinarily important, emerging area of research with enormous scientific value and broad application prospects and will be a major focus of life science researches in the 21st century. Organ transplantation will be replaced by the development and manufacturing of synthetic tissues and organs. One of the key technologies of tissue engineering is the preparation of a biocompatible and biodegradable cell scaffold, and hydrogels represent a large class of materials that can function as tissue engineering scaffolds [130]. Hydrogels are a type of three-dimensional scaffolds with chemical or physical cross-linking structures, which can absorb and retain large amounts of water, yet remain insoluble in water. Hydrogels have been widely used as scaffold materials in tissue engineering for several reasons. First, hydrogels are soft and flexible, similar to soft tissues *in vivo*. Second, hydrogels in the liquid state can be implanted in the body by injection, where they can quickly fill tissue defects by forming irregular nonflowing semisolids [52]. This method is simple and also circumvents risks associated with trauma, infection, and scar formation by surgical implantation. Third, the three-dimensional network structure of a hydrogel is similar to a natural extracellular matrix, which will eventually promote cell engraftment, adhesion, and growth by adjusting the porosity and pore size and increasing the internal surface area [131]. Fourth, hydrogels are rich in water (up to 99%), which is beneficial for the transportation of oxygen, nutrients, and cellular metabolites, in addition to reducing friction and mechanical stimulation of the surrounding tissues. Additionally, the inclusion of cells prior to gelation results in a more uniform distribution of cells throughout the scaffold, thus increasing plating efficiency [132].

A variety of potential medical hydrogels have been investigated in recent years, such as poly(lactic-co-glycolic acid) scaffolds and polylactic acid scaffolds combined with osteoblasts in bone tissue engineering, filamentous collagen materials in neural tissue engineering, and cellulose acetate scaffolds combined with chondrocytes in cartilage tissue

engineering [133–135]. Vo et al. reported the osteogenic potential of injectable, dual thermally and chemically gelable composite hydrogels for mesenchymal stem cell delivery *in vitro* and *in vivo* [136]. A novel composite hydrogel containing copolymer macromers of N-isopropylacrylamide was prepared by the incorporation of gelatin microparticles as enzymatically digestible porogens and sites for cellular attachment. Results indicated that these injectable, dual-gelling cell-laden composite hydrogels could facilitate bone ingrowth and integration, ensuring further research for bone tissue engineering [136]. Also, a novel injectable hydrogel based on a glycopolypeptide was prepared by an enzymatic cross-linking reaction in the presence of horseradish peroxidase and hydrogen peroxide, in which the glycopolypeptide was synthesized through conjugation of poly(γ-propargyl-L-glutamate) with azido-modified mannose and 3-(4-hydroxyphenyl) propanamide *via* click chemistry [137]. The resulting hydrogels displayed good cytocompatibility *in vitro* and were rapidly formed *in situ* after subcutaneous injection into rats, exhibiting acceptable biocompatibility desirable biodegradation *in vivo*. Interestingly, the glycopolypeptide hydrogels containing chondrocytes in the subcutaneous model of nude mice were observed to maintain the chondrocyte phenotype and produce the cartilaginous specific matrix, indicating that the biomimetic glycopolypeptide-based hydrogels represent potential three-dimensional scaffolds for cartilage tissue engineering [137]. Due to additional benefit in electrical conductivity, conductive hydrogels play the tremendous role in tissue engineering. Homogenously electrical double network based on conducting polymer poly(3-thiophene acetic acid) (PTAA) has been reported to be used in myocardial tissue engineering. It can support BADSC adhesion, and reduce inflammation *in vivo*, and the PTAA in this hydrogel can significantly enhance the differentiation potency of BADSCs to cardiomyocytes, increase the expression of myocardial specific proteins cTnT and α-actinin, promote intercellular communication ability, and increase the expression of connexin 43. More importantly, electrical stimulation can enhance the effect of PTAA [138].

4. Conclusions and Future Perspectives

Hydrogels are new functional polymer materials experiencing rapid development. New biomedical hydrogels have been observed to exhibit improved degradation and mechanical properties, thereby overcoming deficiencies found in traditional hydrogels and expanding the potential roles of hydrogels in the field of biomedical applications. However, for applications based on particular tissues or organs, much research remains to develop hydrogels capable of functioning as replacements for real tissues. Future studies into biomedical hydrogels will be needed to address the following: (i) the swelling rate of hydrogels should be controlled while improving their mechanical properties, meeting the size requirements of tissues and organs; (ii) their biocompatibility should be enhanced to achieve simulation of the extracellular matrix structure and functions; (iii) the degradation rate of hydrogels should be controllable, conforming to tissue-specific mechanical properties and regeneration needs; and (iv) hydrogels should be combined with other materials to achieve the complex structural and functional components necessary to act as replacements for specific organs. In summary, while technical problems associated with the synthesis and application of hydrogel materials remain to be resolved, it is clear that continuing research will eventually overcome these problems, leading to a revolutionary new model for bioengineering and advances in tissue replacement and regeneration.

Conflicts of Interest

The authors declare that there is no conflict of interest regarding the publication of this paper.

Authors' Contributions

Ke Wang and Yuting Hao contributed equally to this work.

References

[1] A. S. Hoffman, "Hydrogels for biomedical applications," *Advanced drug delivery reviews.*, vol. 64, pp. 18–23, 2012.

[2] E. M. Ahmed, "Hydrogel: Preparation, characterization, and applications: A review," *Journal of Advanced Research*, vol. 6, no. 2, pp. 105–121, 2015.

[3] H. Hosseini, H. Tenhu, and S. Hietala, "Rheological properties of thermoresponsive nanocomposite hydrogels," *Journal of Applied Polymer Science*, vol. 133, no. 11, 2016.

[4] C. Chang and L. Zhang, "Cellulose-based hydrogels: present status and application prospects," *Carbohydrate polymers.*, vol. 84, no. 1, pp. 40–53, 2011.

[5] K. Nielsen, H. Vorum, N. Ehlers, N. Aagaard, J. Hjortdal, and B. Honoré, "Tear film proteins deposited on high water content contact lenses identified with two-dimensional gel electrophoresis and mass spectrometry," *Acta ophthalmologica.*, vol. 93, no. 7, pp. 658–662, 2015.

[6] E. A. Kamoun, X. Chen, M. S. Mohy Eldin, and E.-R. S. Kenawy, "Crosslinked poly (vinyl alcohol) hydrogels for wound dressing applications: a review of remarkably blended polymers," *Arabian Journal of Chemistry.*, vol. 8, no. 1, pp. 1–14, 2015.

[7] C. Yao, Z. Liu, C. Yang et al., "Smart Hydrogels: Poly(N-isopropylacrylamide)-Clay Nanocomposite Hydrogels with Responsive Bending Property as Temperature-Controlled Manipulators (Adv. Funct. Mater. 20/2015)," *Advanced Functional Materials.*, vol. 25, no. 20, p. 3104, 2015.

[8] N. Rodkate, B. Rutnakornpituk, U. Wichai, G. Ross, and M. Rutnakornpituk, "Smart carboxymethylchitosan hydrogels that have thermo-and pH-responsive properties," *Journal of Applied Polymer Science*, vol. 132, no. 8, 2015.

[9] A. Tudor, L. Florea, S. Gallagher, J. Burns, and D. Diamond, "Poly (ionic liquid) semi-interpenetrating network multi-responsive hydrogels," *Sensors*, vol. 16, no. 2, p. 219, 2016.

[10] M. Karimi, P. S. Zangabad, A. Ghasemi, and M. R. Hamblin, "Electrical and mechanical-responsive nanocarriers," in *Smart External Stimulus-Responsive Nanocarriers for Drug and Gene Delivery*, 2015.

[11] M. K. Lima-Tenório, E. T. Tenório-Neto, F. P. Garcia et al., "Hydrogel nanocomposite based on starch and Co-doped

zinc ferrite nanoparticles that shows magnetic field-responsive drug release changes," *Journal of Molecular Liquids.*, vol. 210, pp. 100–105, 2015.

[12] B. V. Sridhar, J. L. Brock, J. S. Silver, J. L. Leight, M. A. Randolph, and K. S. Anseth, "Tissue engineering: development of a cellularly degradable PEG hydrogel to promote articular cartilage extracellular matrix deposition (Adv. Healthcare Mater. 5/2015)," *Advanced healthcare materials*, vol. 4, no. 5, p. 635, 2015.

[13] L. Gritsch, F. L. Motta, and S. Fare, "History and applications of hydrogels," *Journal of Biomedical Science*, vol. 04, no. 02, p. 13, 2015.

[14] M. Alhede, L. H. Christensen, and T. Bjarnsholt, "Microbial biofilms and adverse reactions to gel fillers used in cosmetic surgery," in *Biofilm-based Healthcare-associated Infections*, pp. 45–52, Springer, Cham, 2015.

[15] A. Blumlein and J. J. McManus, "Bigels formed via spinodal decomposition of unfolded protein," *Journal of Materials Chemistry B.*, vol. 3, no. 17, pp. 3429–3435, 2015.

[16] T. Murakami, B. V. K. J. Schmidt, H. R. Brown, and C. J. Hawker, "One-pot "click" fabrication of slide-ring gels," *Macromolecules*, vol. 48, no. 21, pp. 7774–7781, 2015.

[17] L. Cai, R. E. Dewi, and S. C. Heilshorn, "Injectable hydrogels with in situ double network formation enhance retention of transplanted stem cells," *Advanced Functional Materials.*, vol. 25, no. 9, pp. 1344–1351, 2015.

[18] S. Noori, M. Kokabi, and Z. M. Hassan, "Nanoclay enhanced the mechanical properties of poly (vinyl alcohol)/chitosan/-montmorillonite nanocomposite hydrogel as wound dressing," *Procedia Materials Science*, vol. 11, pp. 152–156, 2015.

[19] S. Merino, C. Martín, K. Kostarelos, M. Prato, and E. Vázquez, "Nanocomposite hydrogels: 3D polymer–nanoparticle synergies for on-demand drug delivery," *ACS Nano*, vol. 9, no. 5, pp. 4686–4697, 2015.

[20] Q. Li, D. G. Barrett, P. B. Messersmith, and N. Holten-Andersen, "Controlling Hydrogel MechanicsviaBio-Inspired Polymer–Nanoparticle Bond Dynamics," *ACS nano*, vol. 10, no. 1, pp. 1317–1324, 2015.

[21] A. K. Gaharwar, N. A. Peppas, and A. Khademhosseini, "Nanocomposite hydrogels for biomedical applications," *Biotechnology and Bioengineering*, vol. 111, no. 3, pp. 441–453, 2014.

[22] R. Balint, N. J. Cassidy, and S. H. Cartmell, "Conductive polymers: towards a smart biomaterial for tissue engineering," *Acta Biomaterialia*, vol. 10, no. 6, pp. 2341–2353, 2014.

[23] A. M. Kloxin, C. J. Kloxin, C. N. Bowman, and K. S. Anseth, "Mechanical properties of cellularly responsive hydrogels and their experimental determination," *Advanced Materials*, vol. 22, no. 31, pp. 3484–3494, 2010.

[24] K. Gilmore, A. J. Hodgson, B. Luan, C. J. Small, and G. G. Wallace, "Preparation of hydrogel/conducting polymer composites," *Polymer Gels and Networks*, vol. 2, no. 2, pp. 135–143, 1994.

[25] K. Sharma, V. Kumar, B. S. Kaith, S. Kalia, and H. C. Swart, "Conducting polymer hydrogels and their applications," in *Conducting Polymer Hybrids*, pp. 193–221, Springer, Cham, 2017.

[26] Q. Tang, J. Lin, J. Wu, C. Zhang, and S. Hao, "Two-steps synthesis of a poly(acrylate–aniline) conducting hydrogel with an interpenetrated networks structure," *Carbohydrate Polymers.*, vol. 67, no. 3, pp. 332–336, 2007.

[27] Q. Tang, J. Wu, and J. Lin, "A multifunctional hydrogel with high conductivity, pH-responsive, thermo-responsive and release properties from polyacrylate/polyaniline hybrid," *Carbohydrate Polymers.*, vol. 73, no. 2, pp. 315–321, 2008.

[28] J. Lin, Q. Tang, D. Hu, X. Sun, Q. Li, and J. Wu, "Electric field sensitivity of conducting hydrogels with interpenetrating polymer network structure," *Colloids and Surfaces A: Physicochemical and Engineering Aspects*, vol. 346, no. 1-3, pp. 177–183, 2009.

[29] Q. Tang, J. Wu, H. Sun, S. Fan, D. Hu, and J. Lin, "Superabsorbent conducting hydrogel from poly(acrylamide-aniline) with thermo-sensitivity and release properties," *Carbohydrate Polymers.*, vol. 73, no. 3, pp. 473–481, 2008.

[30] L. Zhang, W. Du, A. Nautiyal, Z. Liu, and X. Zhang, "Recent progress on nanostructured conducting polymers and composites: synthesis, application and future aspects," *Science China Materials*, vol. 61, no. 3, pp. 303–352, 2018.

[31] Z. Liu, Y. Liu, L. Zhang et al., "Controlled synthesis of transition metal/conducting polymer nanocomposites," *Nanotechnology*, vol. 23, no. 33, p. 335603, 2012.

[32] L. Ghasemi-Mobarakeh, M. P. Prabhakaran, M. Morshed et al., "Application of conductive polymers, scaffolds and electrical stimulation for nerve tissue engineering," *Journal of Tissue Engineering and Regenerative Medicine*, vol. 5, no. 4, pp. e17–e35, 2011.

[33] K. M. Sajesh, R. Jayakumar, S. V. Nair, and K. P. Chennazhi, "Biocompatible conducting chitosan/polypyrrole–alginate composite scaffold for bone tissue engineering," *International journal of biological macromolecules.*, vol. 62, pp. 465–471, 2013.

[34] C. Shi, Y. He, M. Ding, Y. Wang, and J. Zhong, "Nanoimaging of food proteins by atomic force microscopy. Part I: components, imaging modes, observation ways, and research types," *Trends in Food Science & Technology*, vol. 87, pp. 3–13, 2019.

[35] C. Shi, Y. He, M. Ding, Y. Wang, and J. Zhong, "Nanoimaging of food proteins by atomic force microscopy. Part II: application for food proteins from different sources," *Trends in Food Science & Technology*, vol. 87, pp. 14–25, 2019.

[36] F. García, J. Buendía, S. Ghosh, A. Ajayaghosh, and L. Sánchez, "Luminescent and conductive supramolecular polymers obtained from an N-annulated perylenedicarboxamide," *Chemical Communications*, vol. 49, no. 81, pp. 9278–9280, 2013.

[37] D. Mawad, E. Stewart, D. L. Officer et al., "Conducting polymer hydrogels: a single component conducting polymer hydrogel as a scaffold for tissue engineering (Adv. Funct. Mater. 13/2012)," *Advanced Functional Materials.*, vol. 22, no. 13, pp. 2691–2691, 2012.

[38] G. Kaur, R. Adhikari, P. Cass, M. Bown, and P. Gunatillake, "Electrically conductive polymers and composites for biomedical applications," *Rsc Advances.*, vol. 5, no. 47, pp. 37553–37567, 2015.

[39] Y. Shi, J. Zhang, A. M. Bruck et al., "A tunable 3D nanostructured conductive gel framework electrode for high-performance lithium ion batteries," *Advanced Materials*, vol. 29, no. 22, p. 1603922, 2017.

[40] G. Cai, J. Wang, K. Qian, J. Chen, S. Li, and P. S. Lee, "Extremely Stretchable Strain Sensors Based on Conductive Self-Healing Dynamic Cross-Links Hydrogels for Human-Motion Detection," *Advanced Science*, vol. 4, no. 2, p. 1600190, 2017.

[41] Q. Rong, W. Lei, and M. Liu, "Conductive hydrogels as smart materials for flexible electronic devices," *Chemistry–A European Journal.*, vol. 24, no. 64, pp. 16930–16943, 2018.

[42] W. Xu, Y. Ding, Y. Yu, S. Jiang, L. Chen, and H. Hou, "Highly foldable PANi@CNTs/PU dielectric composites toward thin-film capacitor application," *Materials Letters.*, vol. 192, pp. 25–28, 2017.

[43] J. Han, K. Lu, Y. Yue et al., "Nanocellulose-templated assembly of polyaniline in natural rubber-based hybrid elastomers toward flexible electronic conductors," *Industrial Crops and Products*, vol. 128, pp. 94–107, 2019.

[44] S. J. Devaki, R. K. Narayanan, and S. Sarojam, "Electrically conducting silver nanoparticle–polyacrylic acid hydrogel by in situ reduction and polymerization approach," *Materials Letters.*, vol. 116, no. 2, pp. 135–138, 2014.

[45] Y. Xiang and D. Chen, "Preparation of a novel pH-responsive silver nanoparticle/poly (HEMA–PEGMA–MAA) composite hydrogel," *European Polymer Journal.*, vol. 43, no. 10, pp. 4178–4187, 2007.

[46] L. Pan, G. Yu, D. Zhai et al., "Hierarchical nanostructured conducting polymer hydrogel with high electrochemical activity," *Proceedings of the National Academy of Sciences of the United States of America.*, vol. 109, no. 24, pp. 9287–9292, 2012.

[47] N. Park, S. C. Chae, I. T. Kim, and J. Hur, "Fabrication of self-healable and patternable polypyrrole/agarose hybrid hydrogels for smart bioelectrodes," *Journal of Nanoscience and Nanotechnology*, vol. 16, no. 2, pp. 1400–1404, 2016.

[48] J. Hur, K. Im, S. W. Kim et al., "Polypyrrole/agarose-based electronically conductive and reversibly restorable hydrogel," *ACS Nano*, vol. 8, no. 10, pp. 10066–10076, 2014.

[49] S. Zhou, M. Wang, X. Chen, and F. Xu, "Facile template synthesis of microfibrillated cellulose/polypyrrole/silver nanoparticles hybrid aerogels with electrical conductive and pressure responsive properties," *Acs Sustainable Chemistry & Engineering.*, vol. 3, no. 12, pp. 3346–3354, 2015.

[50] S. S. Sivan, S. Roberts, J. P. G. Urban et al., "Injectable hydrogels with high fixed charge density and swelling pressure for nucleus pulposus repair: Biomimetic glycosaminoglycan analogues," *Acta Biomaterialia*, vol. 10, no. 3, pp. 1124–1133, 2014.

[51] J.-A. Yang, J. Yeom, B. W. Hwang, A. S. Hoffman, and S. K. Hahn, "In situ-forming injectable hydrogels for regenerative medicine," *Progress in Polymer Science.*, vol. 39, no. 12, pp. 1973–1986, 2014.

[52] H. Park, B. Choi, J. Hu, and M. Lee, "Injectable chitosan hyaluronic acid hydrogels for cartilage tissue engineering," *Acta Biomaterialia*, vol. 9, no. 1, pp. 4779–4786, 2013.

[53] J. Hu, Y. Hou, H. Park et al., "Visible light crosslinkable chitosan hydrogels for tissue engineering," *Acta Biomaterialia*, vol. 8, no. 5, pp. 1730–1738, 2012.

[54] S. Koutsopoulos and S. Zhang, *Multi-layered injectable self-assembling peptide scaffold hydrogels for long-term sustained release of human antibodies*, Google Patents, 9700521B2, Washington, DC, USA, 2014.

[55] S. Koutsopoulos and S. Zhang, "Two-layered injectable self-assembling peptide scaffold hydrogels for long-term sustained release of human antibodies," *Journal of Controlled Release*, vol. 160, no. 3, pp. 451–458, 2012.

[56] F. Corrente, H. M. Abu Amara, S. Pacelli, P. Paolicelli, and M. A. Casadei, "Novel injectable and in situ cross-linkable hydrogels of dextran methacrylate and scleroglucan derivatives: preparation and characterization," *Carbohydrate polymers.*, vol. 92, no. 2, pp. 1033–1039, 2013.

[57] S. Pacelli, P. Paolicelli, I. Dreesen, S. Kobayashi, A. Vitalone, and M. A. Casadei, "Injectable and photocross-linkable gels based on gellan gum methacrylate: a new tool for biomedical application," *International journal of biological macromolecules.*, vol. 72, pp. 1335–1342, 2015.

[58] O. Yom-Tov, L. Neufeld, D. Seliktar, and H. Bianco-Peled, "A novel design of injectable porous hydrogels with in situ pore formation," *Acta Biomaterialia*, vol. 10, no. 10, pp. 4236–4246, 2014.

[59] Q. Chen, L. Zhu, C. Zhao, Q. Wang, and J. Zheng, "A robust, one-pot synthesis of highly mechanical and recoverable double network hydrogels using thermoreversible sol-gel polysaccharide," *Advanced Materials*, vol. 25, no. 30, pp. 4171–4176, 2013.

[60] T. Hattori, K. Ishii, T. Tominaga, Y. Osada, and T. Tahara, "A fluorescence study on the local environment of hydrogels: double-network hydrogels having extraordinarily high mechanical strength and its constituent single-network hydrogels," *Chemical Physics.*, vol. 419, pp. 172–177, 2013.

[61] H. Yin, T. Akasaki, T. Lin Sun et al., "Double network hydrogels from polyzwitterions: high mechanical strength and excellent anti-biofouling properties," *Journal of Materials Chemistry B.*, vol. 1, no. 30, pp. 3685–3693, 2013.

[62] H. Shin, B. D. Olsen, and A. Khademhosseini, "The mechanical properties and cytotoxicity of cell-laden double-network hydrogels based on photocrosslinkable gelatin and gellan gum biomacromolecules," *Biomaterials*, vol. 33, no. 11, pp. 3143–3152, 2012.

[63] S. J. Buwalda, K. W. M. Boere, P. J. Dijkstra, J. Feijen, T. Vermonden, and W. E. Hennink, "Hydrogels in a historical perspective: from simple networks to smart materials," *Journal of Controlled Release*, vol. 190, pp. 254–273, 2014.

[64] T. Kataoka, Y. Ishioka, M. Mizuhata, H. Minami, and T. Maruyama, "Highly conductive ionic-liquid gels prepared with orthogonal double networks of a low-molecular-weight gelator and cross-linked polymer," *ACS applied materials & interfaces.*, vol. 7, no. 41, pp. 23346–23352, 2015.

[65] Y. Zhang, Y. Li, and W. Liu, "Dipole–dipole and H-bonding interactions significantly enhance the multifaceted mechanical properties of thermoresponsive shape memory hydrogels," *Advanced Functional Materials.*, vol. 25, no. 3, pp. 471–480, 2015.

[66] Y. H. Na, "Double network hydrogels with extremely high toughness and their applications," *Korea-Australia Rheology Journal.*, vol. 25, no. 4, pp. 185–196, 2013.

[67] C. Chassenieux and C. Tsitsilianis, "Recent trends in pH/thermo-responsive self-assembling hydrogels: from polyions to peptide-based polymeric gelators," *Soft Matter*, vol. 12, no. 5, pp. 1344–1359, 2016.

[68] M. A. Haque, T. Kurokawa, and J. P. Gong, "Super tough double network hydrogels and their application as biomaterials," *Polymer*, vol. 53, no. 9, pp. 1805–1822, 2012.

[69] C. Chang, K. Han, and L. Zhang, "Structure and properties of cellulose/poly(N-isopropylacrylamide) hydrogels prepared by IPN strategy," *Polymers for Advanced Technologies.*, vol. 22, no. 9, pp. 1329–1334, 2011.

[70] J.-Y. Sun, X. Zhao, W. R. K. Illeperuma et al., "Highly stretchable and tough hydrogels," *Nature*, vol. 489, no. 7414, pp. 133–136, 2012.

[71] A. Döring, W. Birnbaum, and D. Kuckling, "Responsive hydrogels–structurally and dimensionally optimized smart frameworks for applications in catalysis, micro-system technology and material science," *Chemical Society Reviews.*, vol. 42, no. 17, pp. 7391–7420, 2013.

[72] M. C. Koetting, J. T. Peters, S. D. Steichen, and N. A. Peppas, "Stimulus-responsive hydrogels: theory, modern advances, and applications," *Materials Science and Engineering: R: Reports.*, vol. 93, pp. 1–49, 2015.

[73] X. Wang, Y. Zhang, W. Xue, H. Wang, X. Qiu, and Z. Liu, "Thermo-sensitive hydrogel PLGA-PEG-PLGA as a vaccine delivery system for intramuscular immunization," *Journal of Biomaterials Applications.*, vol. 31, no. 6, pp. 923–932, 2016.

[74] M. Krogsgaard, M. A. Behrens, J. S. Pedersen, and H. Birkedal, "Self-healing mussel-inspired multi-pH-responsive hydrogels," *Biomacromolecules*, vol. 14, no. 2, pp. 297–301, 2013.

[75] A. Katchalsky, "Rapid swelling and deswelling of reversible gels of polymeric acids by ionization," *Cellular and Molecular Life Sciences.*, vol. 5, no. 8, pp. 319-320, 1949.

[76] M. P. M. Dicker, I. P. Bond, J. M. Rossiter, C. F. J. Faul, and P. M. Weaver, "Modelling and Analysis of pH Responsive Hydrogels for the Development of Biomimetic Photo-Actuating Structures," *MRS Proceedings*, vol. 1718, pp. 65–70, 2015.

[77] C. Scherzinger, A. Schwarz, A. Bardow, K. Leonhard, and W. Richtering, "Cononsolvency of poly-N-isopropyl acrylamide (PNIPAM): microgels versus linear chains and macrogels," *Current Opinion in Colloid & Interface Science.*, vol. 19, no. 2, pp. 84–94, 2014.

[78] Y. Işikver and D. Saraydin, "Environmentally sensitive hydrogels: N-isopropyl acrylamide/acrylamide/mono-, Di-, tricarboxylic acid crosslinked polymers," *Polymer Engineering & Science.*, vol. 55, no. 4, pp. 843–851, 2015.

[79] J. Wang, Q. Zhong, J. Wu, and T. Chen, "Thermo-responsive textiles," in *Handbook of Smart Textiles*, pp. 1–27, 2014.

[80] W. Wei, X. Hu, X. Qi et al., "A novel thermo-responsive hydrogel based on salecan and poly (N-isopropylacrylamide): synthesis and characterization," *Colloids and Surfaces B: Biointerfaces.*, vol. 125, pp. 1–11, 2015.

[81] C. H. Hofmann, F. A. Plamper, C. Scherzinger, S. Hietala, and W. Richtering, "NEXT Cononsolvency Revisited: Solvent Entrapment by *N*-Isopropylacrylamide and *N,N*-Diethylacrylamide Microgels in Different Water/Methanol Mixtures," *Macromolecules*, vol. 46, no. 2, pp. 523–532, 2012.

[82] P. Mukhopadhyay, K. Sarkar, S. Bhattacharya, A. Bhattacharyya, R. Mishra, and P. P. Kundu, "pH sensitive N-succinyl chitosan grafted polyacrylamide hydrogel for oral insulin delivery," *Carbohydrate polymers.*, vol. 112, pp. 627–637, 2014.

[83] T. Garg, S. Singh, and A. K. Goyal, "Stimuli-sensitive hydrogels: an excellent carrier for drug and cell delivery," *Critical Reviews™ in Therapeutic Drug Carrier Systems*, vol. 30, no. 5, pp. 369–409, 2013.

[84] J. Yang, J. Chen, D. Pan, Y. Wan, and Z. Wang, "pH-sensitive interpenetrating network hydrogels based on chitosan derivatives and alginate for oral drug delivery," *Carbohydrate polymers.*, vol. 92, no. 1, pp. 719–725, 2013.

[85] J. Liu, Y. Huang, A. Kumar et al., "pH-sensitive nano-systems for drug delivery in cancer therapy," *Biotechnology advances.*, vol. 32, no. 4, pp. 693–710, 2014.

[86] S. Naficy, J. M. Razal, P. G. Whitten, G. G. Wallace, and G. M. Spinks, "A pH-sensitive, strong double-network hydrogel: poly (ethylene glycol) methyl ether methacrylates–poly (acrylic acid)," *Journal of Polymer Science Part B: Polymer Physics.*, vol. 50, no. 6, pp. 423–430, 2012.

[87] Y. Wang, A. Dong, Z. Yuan, and D. Chen, "Fabrication and characterization of temperature-, pH- and magnetic-field-sensitive organic/inorganic hybrid poly (ethylene glycol)-based hydrogels," *Colloids and Surfaces A: Physicochemical and Engineering Aspects.*, vol. 415, pp. 68–76, 2012.

[88] S. Roy, A. Baral, and A. Banerjee, "An amino-acid-based self-healing hydrogel: modulation of the self-healing properties by incorporating carbon-based nanomaterials," *Chemistry–A European Journal.*, vol. 19, no. 44, pp. 14950–14957, 2013.

[89] H.-P. Cong, X.-C. Ren, P. Wang, and S.-H. Yu, "Macroscopic multifunctional graphene-based hydrogels and aerogels by a metal ion induced self-assembly process," *ACS Nano*, vol. 6, no. 3, pp. 2693–2703, 2012.

[90] H. Hezaveh and I. I. Muhamad, "Impact of metal oxide nanoparticles on oral release properties of pH-sensitive hydrogel nanocomposites," *International journal of biological macromolecules.*, vol. 50, no. 5, pp. 1334–1340, 2012.

[91] M. Yadollahi, I. Gholamali, H. Namazi, and M. Aghazadeh, "Synthesis and characterization of antibacterial carboxymethyl cellulose/ZnO nanocomposite hydrogels," *International journal of biological macromolecules.*, vol. 74, pp. 136–141, 2015.

[92] Y.-C. Wang, J. Wu, Y. Li, J.-Z. Du, Y.-Y. Yuan, and J. Wang, "Engineering nanoscopic hydrogels via photo-crosslinking salt-induced polymer assembly for targeted drug delivery," *Chemical Communications.*, vol. 46, no. 20, pp. 3520–3522, 2010.

[93] C. W. Peak, J. J. Wilker, and G. Schmidt, "A review on tough and sticky hydrogels," *Colloid and Polymer Science.*, vol. 291, no. 9, pp. 2031–2047, 2013.

[94] Y. Cui, M. Tan, A. Zhu, and M. Guo, "Strain hardening and highly resilient hydrogels crosslinked by chain-extended reactive pseudo-polyrotaxane," *RSC Advances.*, vol. 4, no. 100, pp. 56791–56797, 2014.

[95] M. Du, Y. Zhang, Y. Song, and Q. Zheng, "Negative velocity dependence of friction for poly (2-acrylamido-2-methyl propanesulfonic acid) hydrogel sliding against a glass surface in the low-velocity region," *Journal of Polymer Science Part B: Polymer Physics.*, vol. 52, no. 11, pp. 765–772, 2014.

[96] T. Sakai, H. Murayama, S. Nagano et al., "Photoresponsive slide-ring gel," *Advanced Materials*, vol. 19, no. 15, pp. 2023–2025, 2007.

[97] G. Fleury, G. Schlatter, C. Brochon et al., "Topological polymer networks with sliding cross-link points: the "sliding gels". Relationship between their molecular structure and the viscoelastic as well as the swelling properties," *Macromolecules*, vol. 40, no. 3, pp. 535–543, 2007.

[98] K. Barker, S. K. Rastogi, J. Dominguez et al., "Biodegradable DNA-enabled poly (ethylene glycol) hydrogels prepared by copper-free click chemistry," *Journal of Biomaterials Science, Polymer Edition.*, vol. 27, no. 1, pp. 22–39, 2016.

[99] I. Y. Tóth, G. Veress, M. Szekeres, E. Illés, and E. Tombácz, "Magnetic hyaluronate hydrogels: preparation and

characterization," *Journal of Magnetism and Magnetic Materials.*, vol. 380, pp. 175–180, 2015.

[100] L. Kaisang, W. Siyu, F. Lijun, P. Daoyan, C. J. Xian, and S. Jie, "Adipose-derived stem cells seeded in Pluronic F-127 hydrogel promotes diabetic wound healing," *Journal of Surgical Research.*, vol. 217, pp. 63–74, 2017.

[101] O. Tacar, P. Sriamornsak, and C. R. Dass, "Doxorubicin: an update on anticancer molecular action, toxicity and novel drug delivery systems," *Journal of Pharmacy and Pharmacology.*, vol. 65, no. 2, pp. 157–170, 2013.

[102] C. Gong, T. Qi, X. Wei et al., "Thermosensitive polymeric hydrogels as drug delivery systems," *Current medicinal chemistry.*, vol. 20, no. 1, pp. 79–94, 2013.

[103] G. W. Ashley, J. Henise, R. Reid, and D. V. Santi, "Hydrogel drug delivery system with predictable and tunable drug release and degradation rates," *Proceedings of the National Academy of Sciences.*, vol. 110, no. 6, pp. 2318–2323, 2013.

[104] S. L. Steffensen, M. H. Vestergaard, E. H. Møller et al., "Soft hydrogels interpenetrating silicone—a polymer network for drug-releasing medical devices," *Journal of Biomedical Materials Research Part B: Applied Biomaterials.*, vol. 104, no. 2, pp. 402–410, 2016.

[105] S. Selvakumaran, I. I. Muhamad, and S. I. Abd Razak, "Evaluation of kappa carrageenan as potential carrier for floating drug delivery system: effect of pore forming agents," *Carbohydrate polymers.*, vol. 135, pp. 207–214, 2016.

[106] L. M. Lira and S. I. Córdoba de Torresi, "Conducting polymer–hydrogel composites for electrochemical release devices: synthesis and characterization of semi-interpenetrating polyaniline–polyacrylamide networks," *Electrochemistry Communications*, vol. 7, no. 7, pp. 717–723, 2005.

[107] S. Mongkolkitikul, N. Paradee, and A. Sirivat, "Electrically controlled release of ibuprofen from conductive poly(3-methoxydiphenylamine)/crosslinked pectin hydrogel," *European Journal of Pharmaceutical Sciences.*, vol. 112, pp. 20–27, 2018.

[108] Y. Liang, M. V. Coffin, S. D. Manceva, J. A. Chichester, R. M. Jones, and K. L. Kiick, "Controlled release of an anthrax toxin-neutralizing antibody from hydrolytically degradable polyethylene glycol hydrogels," *Journal of Biomedical Materials Research Part A.*, vol. 104, no. 1, pp. 113–123, 2016.

[109] D. Codoni, J. Cowan, J. Bradley, W. J. McAuley, M. A. O'Connell, and S. Qi, "Disc-shaped polyoxyethylene glycol glycerides gel nanoparticles as novel protein delivery vehicles," *International Journal of Pharmaceutics*, vol. 496, no. 2, pp. 1015–1025, 2015.

[110] N. Wang, Y. Li, Y. Zhang, Y. Liao, and W. Liu, "High-strength photoresponsive hydrogels enable surface-mediated gene delivery and light-induced reversible cell adhesion/detachment," *Langmuir*, vol. 30, no. 39, pp. 11823–11832, 2014.

[111] B. Boonkaew, M. Kempf, R. Kimble, P. Supaphol, and L. Cuttle, "Antimicrobial efficacy of a novel silver hydrogel dressing compared to two common silver burn wound dressings: Acticoat™ and PolyMem Silver®," *Burns*, vol. 40, no. 1, pp. 89–96, 2014.

[112] E. Pinho, M. Grootveld, G. Soares, and M. Henriques, "Cyclodextrin-based hydrogels toward improved wound dressings," *Critical Reviews in Biotechnology*, vol. 34, no. 4, pp. 328–337, 2014.

[113] X. Chen, M. Zhang, S. Chen et al., "Peptide-modified chitosan hydrogels accelerate skin wound healing by promoting fibroblast proliferation, migration, and secretion," *Cell Transplantation.*, vol. 26, no. 8, pp. 1331–1340, 2017.

[114] B. Singh, S. Sharma, and A. Dhiman, "Design of antibiotic containing hydrogel wound dressings: biomedical properties and histological study of wound healing," *International Journal of Pharmaceutics*, vol. 457, no. 1, pp. 82–91, 2013.

[115] Y. Loo, Y.-C. Wong, E. Z. Cai et al., "Ultrashort peptide nanofibrous hydrogels for the acceleration of healing of burn wounds," *Biomaterials*, vol. 35, no. 17, pp. 4805–4814, 2014.

[116] D. Singh, A. Singh, and R. Singh, "Polyvinyl pyrrolidone/-carrageenan blend hydrogels with nanosilver prepared by gamma radiation for use as an antimicrobial wound dressing," *Journal of Biomaterials Science, Polymer Edition.*, vol. 26, no. 17, pp. 1269–1285, 2015.

[117] S.-M. Lee, N. Han, R. Lee et al., "Real-time monitoring of 3D cell culture using a 3D capacitance biosensor," *Biosensors and Bioelectronics.*, vol. 77, pp. 56–61, 2016.

[118] I. Zhitomirsky, "Electrodeposition of organic-inorganic films for biomedical applications," *224th ECS Meeting*, 2013, Hamilton, Ontario, Canada, October 27–November 1, 2013, 2013.

[119] M. S. Belluzo, L. F. Medina, A. M. Cortizo, and M. S. Cortizo, "Ultrasonic compatibilization of polyelectrolyte complex based on polysaccharides for biomedical applications," *Ultrasonics sonochemistry.*, vol. 30, pp. 1–8, 2016.

[120] I. Khimji, E. Y. Kelly, Y. Helwa, M. Hoang, and J. Liu, "Visual optical biosensors based on DNA-functionalized polyacrylamide hydrogels," *Methods*, vol. 64, no. 3, pp. 292–298, 2013.

[121] M. S. Abdelaty and D. Kuckling, "Synthesis and characterization of new functional photo cross-linkable smart polymers containing vanillin derivatives," *Gels.*, vol. 2, no. 1, p. 3, 2016.

[122] Z. Wang, L. Zhang, and Y. Tian, "A durable non-enzymatic electrochemical sensor for monitoring H_2O_2 in rat brain microdialysates based on one-step fabrication of hydrogels," *The Analyst*, vol. 140, no. 11, pp. 3788–3793, 2015.

[123] J. P. Devadhasan and S. Kim, "An ultrasensitive method of real time pH monitoring with complementary metal oxide semiconductor image sensor," *Analytica Chimica Acta*, vol. 858, pp. 55–59, 2015.

[124] J. S. Wolffsohn, S. Mroczkowska, O. A. Hunt, P. Bilkhu, T. Drew, and A. Sheppard, "Crossover evaluation of silicone hydrogel daily disposable contact lenses," *Optometry and Vision Science*, vol. 92, no. 11, pp. 1063–1068, 2015.

[125] G. Su, T. Zhou, Y. Zhang, X. Liu, and A. Zhang, "Microdynamics mechanism of D_2O absorption of the poly (2-hydroxyethyl methacrylate)-based contact lens hydrogel studied by two-dimensional correlation ATR-FTIR spectroscopy," *Soft Matter*, vol. 12, no. 4, pp. 1145–1157, 2016.

[126] S. Mikhalovsky, L. Mikhalovska, W. A. Akande, and S. James, *Poly (2-hydroxyethyl methacrylate) macroporous cryogel for extracorporeal medical devices*, Nazarbayev University, Nur-Sultan city, Republic of Kazakhstan, 2015.

[127] E. García-Millán, S. Koprivnik, and F. J. Otero-Espinar, "Drug loading optimization and extended drug delivery of corticoids from pHEMA based soft contact lenses hydrogels via chemical and microstructural modifications," *International Journal of Pharmaceutics*, vol. 487, no. 1-2, pp. 260–269, 2015.

[128] T. Billiet, M. Vandenhaute, J. Schelfhout, S. Van Vlierberghe, and P. Dubruel, "A review of trends and limitations in

hydrogel-rapid prototyping for tissue engineering," *Biomaterials*, vol. 33, no. 26, pp. 6020–6041, 2012.

[129] L. E. Bertassoni, M. Cecconi, V. Manoharan et al., "Hydrogel bioprinted microchannel networks for vascularization of tissue engineering constructs," *Lab on a Chip.*, vol. 14, no. 13, pp. 2202–2211, 2014.

[130] P. Matricardi, C. Di Meo, T. Coviello, W. E. Hennink, and F. Alhaique, "Interpenetrating polymer networks polysaccharide hydrogels for drug delivery and tissue engineering," *Advanced drug delivery reviews.*, vol. 65, no. 9, pp. 1172–1187, 2013.

[131] H. K. Cheung, T. T. Y. Han, D. M. Marecak, J. F. Watkins, B. G. Amsden, and L. E. Flynn, "Composite hydrogel scaffolds incorporating decellularized adipose tissue for soft tissue engineering with adipose-derived stem cells," *Biomaterials*, vol. 35, no. 6, pp. 1914–1923, 2014.

[132] H. Tan and K. G. Marra, "Injectable, biodegradable hydrogels for tissue engineering applications," *Materials.*, vol. 3, no. 3, pp. 1746–1767, 2010.

[133] P. Gentile, V. Chiono, I. Carmagnola, and P. V. Hatton, "An overview of poly (lactic-co-glycolic) acid (PLGA)-based biomaterials for bone tissue engineering," *International journal of molecular sciences.*, vol. 15, no. 3, pp. 3640–3659, 2014.

[134] J. Van Hoorick, M. Markovic, A. Ovsianikov et al., "Hydrogel-polyester combination scaffolds for tissue engineering purposes," in *Conference on Advanced Materials for Biomedical Applications (AMBA 2014)*, Ghent, Belgium, 2014-11-18.

[135] I. De Marco, L. Baldino, S. Cardea, and E. Reverchon, "Effect of process parameters on cellulose acetate scaffolds morphology obtained by supercritical CO_2 phase inversion," in *Applied Engineering Sciences: Proceedings of the 2014 AASRI International Conference on Applied Engineering Sciences*, CRC Press, p. 135, Hollywood, LA, USA, 2014.

[136] T. N. Vo, S. R. Shah, S. Lu et al., "Injectable dual-gelling cell-laden composite hydrogels for bone tissue engineering," *Biomaterials*, vol. 83, pp. 1–11, 2016.

[137] K. Ren, C. He, C. Xiao, G. Li, and X. Chen, "Injectable glycopolypeptide hydrogels as biomimetic scaffolds for cartilage tissue engineering," *Biomaterials*, vol. 51, pp. 238–249, 2015.

[138] B. Yang, F. Yao, T. Hao et al., "Development of electrically conductive double-network hydrogels via one-step facile strategy for cardiac tissue engineering," *Advanced Healthcare Materials.*, vol. 5, no. 4, pp. 474–488, 2016.

Hindawi
International Journal of Polymer Science
Volume 2019, Article ID 9302803, 12 pages
https://doi.org/10.1155/2019/9302803

Research Article

Functionalized Multiwalled Carbon Nanotube-Reinforced Polyimide Composite Films with Enhanced Mechanical and Thermal Properties

Min Chao,[1] **Yanming Li**,[1] **Guanglei Wu**,[2,3] **Zhenjun Zhou**,[1] **and Luke Yan**[1]

[1]*Polymer Materials & Engineering Department, School of Materials Science & Engineering, Engineering Research Center of Transportation Materials, Ministry of Education, Chang'an University, Xi'an 710064, China*
[2]*Institute of Materials for Energy and Environment, State Key Laboratory of Bio-Fibers and Eco-Textiles, College of Materials Science and Engineering, Qingdao University, Qingdao 266071, China*
[3]*Key Laboratory of Engineering Dielectrics and Its Application, Ministry of Education, Harbin University of Science and Technology, Harbin 150080, China*

Correspondence should be addressed to Luke Yan; yanlk_79@hotmail.com

Received 25 April 2019; Accepted 12 June 2019; Published 14 August 2019

Guest Editor: Chao Zhang

Polyimide- (PI-) based nanocomposites containing the 4,4′-diaminodiphenyl ether- (ODA-) modified multiwalled carbon nanotube (MWCNT) filler were successfully prepared. The PI/MWCNTs-ODA composite films exhibit high thermal conductivity and excellent mechanical property. The optimal value of thermal conductivity of the PI/MWCNTs-ODA composite film is 0.4397 W/mK with 3 wt.% filler loading, increased by 221.89% in comparison with that of the pure PI film. In addition, the tensile strength of the PI/MWCNTs-ODA composite film is 141.48 MPa with 3 wt.% filler loading, increased by 20.74% in comparison with that of the pure PI film. This work develops a new strategy to achieve a good balance between the high thermal conductivity and excellent mechanical properties of polyimide composite films by using functionalized carbon nanotubes as an effective thermal conductive filler.

1. Introduction

Polyimide (PI) has been demonstrated one of the most important high-performance engineering plastics for its excellent mechanical property [1–3], thermal stability [4], and chemical resistance [5] because of its rigid-rod chemical structures, showing appealing potential in the area of electronic applications, membrane, insulating materials, and aerospace industry [6–10]. However, the very low thermal conductivity (0.1 W/mK) of PI can hardly meet the thermal requirements of electronic products, which limits its application in advanced microelectronics and aerospace applications. In order to facilitate the heat dissipation, it is necessary to further improve the thermal conductivity of PI. Therefore, improving the thermal conductivity of PI to endow it with better comprehensive performance has become a research focus. Introducing functional groups or elements into the main chain is an effective way to improve the performance of PI by lengthening the molecular chain and reducing the interaction between molecular chains. In addition, adding high thermal conductive fillers is another facile method to promote the thermal performance of PI [11–17].

Various inorganic fillers owning high thermal conductivity have been added into the PI matrix by in situ polymerization to improve the overall performance of PI, including carbon black [18, 19], alumina (Al_2O_3) [20, 21], aluminum nitride (AlN) [22, 23], silica (SiO_2) [24, 25], titanium dioxide (TiO_2) [26], silicon carbide (SiC) [27, 28], silicon nitride (Si_3N_4) [29, 30], boron nitride (BN) [31, 32], and zinc oxide (ZnO) [33, 34]. Compared with the abovementioned inorganic fillers, carbon nanotubes (CNTs) possess high electrical conductivity (10^5 S·cm^{-1}) and thermal conductivity (3500 W/mK) and extremely high Young modulus (0.9 TPa) and tensile strength (150 GPa), as well as

excellent optical properties [35]. So, CNTs are considered to be the most optimal candidate as ideal enhancing fillers in high tensile, light weight polymer nanocomposites [36–41]. Although CNTs have many merits, there are two major disadvantages that limit their reinforcing efficiency: (1) the bad dispersion of nanoparticles in the polymer matrix and (2) the weak interfacial interaction between nanoparticles and polymer matrix [42–44].

Hence, increasing the dispersion of carbon nanotube nanoparticles in the polymer matrix and enhancing the interfacial interaction between nanoparticles and polymer matrix are critical troubles to make carbon nanotubes fully exert their potential to enhance the performance of the polymer matrix. Wang et al. [45] investigated graphene oxide@carbon nanotube- (GO/CNT-) reinforced PI; by the crosslinking between the amide bonds, the dispersibility of the nanoparticles in the polyimide matrix can be improved and the interfacial interaction between the nanoparticles and the PI matrix can be improved. Li et al. [46] reported that multiwalled carbon nanotubes (MWCNTs) were revised by polyacrylic acid, polyacrylamide, or poly(hydroxyethyl methylacrylate) which is used in the field of biomineralization. The polymer chains were deposited on the MWCNTs by photoinitiated polymerization of the monomers. Chen et al. [47] investigated the amine-treated MWCNTs/epoxy composites in which amine-treated MWCNTs were used as curing agents and are covalently grafted into the epoxy matrix. The tensile strength and impact strength of the composites increase with the content of MWCNTs, and the most significant improvement of the tensile strength is obtained with the addition of 1.5 wt.% amine-treated MWCNTs; the thermal stability of the nanocomposites also distinctly improves. In addition, different amine-treated graphenes, including ethylenediamine, diethylenetriamine, and p-phenylenediamine (EG, DG, and PG, respectively), were employed in synthesizing different contents of PI composites by in situ polymerization [48].

In this work, we prepared carboxylated carbon nanotubes; then, the carboxyl treated MWCNTs (MWCNTs-COOH) were reacted with 4,4′-diaminodiphenyl ether (ODA) to obtain the amino carbon nanotubes (MWCNTs-ODA), which is used to synthesize PI composites by in situ polymerization. The PI composite films prepared by this method can improve the compatibility of CNTs with the PI matrix. The mechanical and thermal properties of PI/MWCNTs-ODA nanocomposite films were studied, while varying different contents in the MWCNTs-ODA.

2. Experimental

2.1. Materials. Multiwalled carbon nanotubes (MWCNTs) were obtained from Chengdu Organic Chemicals Co. Ltd., Chinese Academy of Sciences (China), with the length of 10-30 μm; the outer diameter is 10-20 nm and a purity of >98%. Pyromellitic dianhydride (PMDA) (purity: >98.5%) and 4,4′-diaminodiphenyl ether (ODA) (purity: >98.0%) were purchased from Sinopharm Chemical Reagent Co. Ltd., China. N,N-Dimethylacetamide (DMAc) (purity: >99.5%), N,N-dimethylformamide (DMF) (purity: >99.5%), and ethanol (purity: >99.7%) were purchased from Fuyu Fine Chemical Co. Ltd. (Tianjin, China). N,N′-Dicyclohexylcarbodiimide (DCC) (purity: >99.0%) as a dehydrant and 4-dimethylaminopyridine (DMAP) (purity: >99.0%) as catalysts were purchased from Aladdin Industrial Corporation (Shanghai, China).

2.2. Synthesis of Amino-Functionalized MWCNTs. In a typical process of MWCNTs-COOH, 2 g pristine MWCNTs were mixed with 150 ml acid mixture of concentrated H_2SO_4 and concentrated HNO_3 (volume ratio was 3 : 1). The mixture was treated with ultrasound for 1 hour at ambient temperature (KH-600 KDE, 600 W, 40 kHz) and dispersed evenly. The mixture was then poured into a 250 ml three-neck glass flask, followed by mechanical stirring under 70°C, oil bath for 24 hours. After that, the mixture was diluted with deionized water and precipitated and the supernatant was poured out, diluted, and precipitated multiple times. After centrifugation (TG-16, 8000 rpm, 10 min), we poured off the supernatant and then washed the remaining material with DMF until the pH is 7. Finally, the MWCNTs-COOH was obtained by overnight drying in a vacuum for 60°C.

Amino functional groups are grafted onto carboxylated carbon nanotube. In typical experiments, 0.2 g of MWCNTs-COOH, 20 ml of DMF, 2 g of ODA, 1 g of DCC, and 0.6 g of DMAP were mixed. Then, the mixed liquor was put into trinecked flask and magnetically stirred for 4 days at 100°C oil bath. After that, it was centrifuged (8000 rpm, 10 min) and washed with ethanol and the treated substance was put into a vacuum oven for 60°C (DZF-6020, 450 W, 50 Hz) to dry overnight to get MWCNTs-ODA. The specific synthesis process is shown in Scheme 1.

2.3. Preparation of WMCNTs-ODA/PI Nanocomposite Films. The preparation process of the PI/MWCNTs-ODA composite films includes the synthesis of PAA and preparation of PI. First, 2.2737 g (11.36 mmol) ODA was added in DMAc in a 100 ml trinecked flask, followed by stirring vigorously at room temperature for 30 minutes. Afterwards, 2.5263 g (11.58 mmol) PMDA (the molar ratio of PMDA and ODA was 1.02 : 1) was added in batches for six times, keeping the reaction temperature unchanged. After adding all PMDA, the mixture is kept in ice bath (temperature controlled at 2°C-10°C) for 1 hour. At the same time, 18.5 ml DMAc and a certain amount of prepared MWCNTs-ODA were mixed in the beaker, ultrasonic treatment for 1 hour at room temperature was done for even dispersion, and then MWCNTs-ODA/DMAc mixture was added to the reaction mixture in the ice bath. After the ice bath, the preparation of polyimide precursor polyamic acid (PAA)/MWCNTs-ODA mixture was casted on a clean glass substrate and the thickness was controlled within 1 mm, which was then put into the vacuum oven for 0.5 hour. The mixture underwent a series of thermal treatments afterwards; i.e., it was heated at 30°C for 1 hour, 50°C for 3 hours, 100°C for 1 hour, 200°C for 3 hours, and 250°C for 3 hours to complete the thermal imidization. WMCNTs-ODA/PI was prepared by natural cooling at room temperature. The solid content of

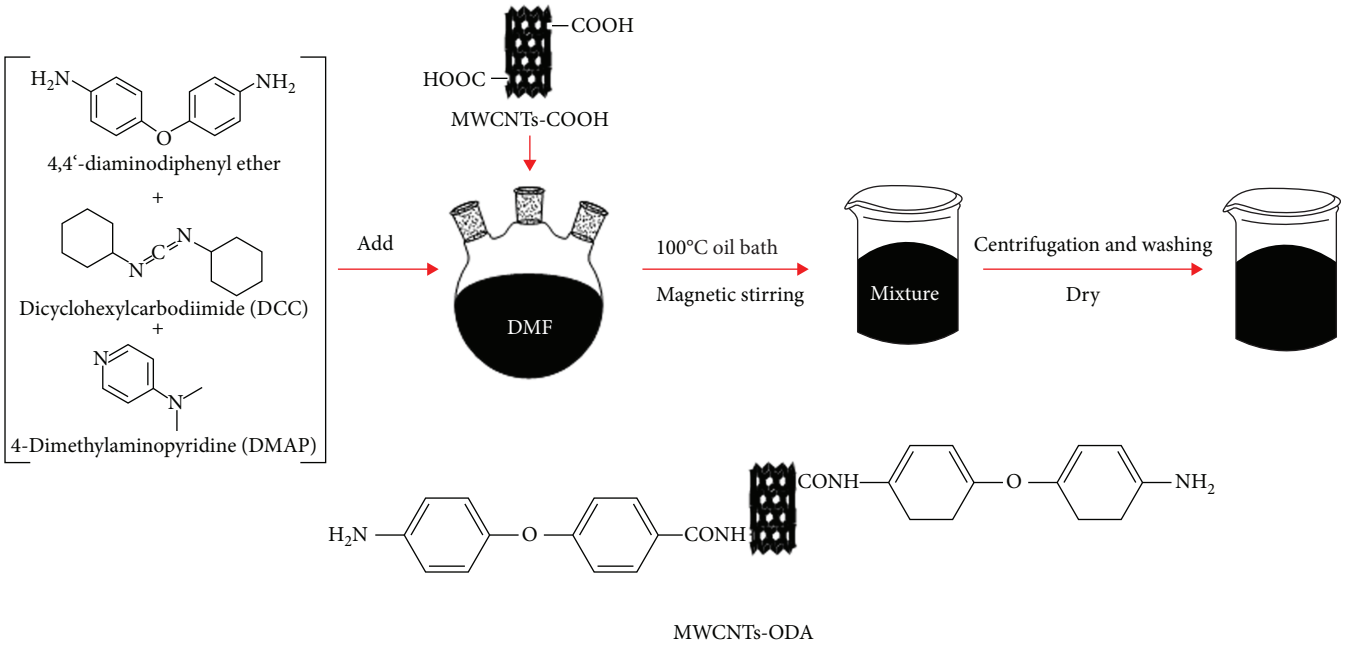

Scheme 1: The preparation process of MWCNTs-ODA.

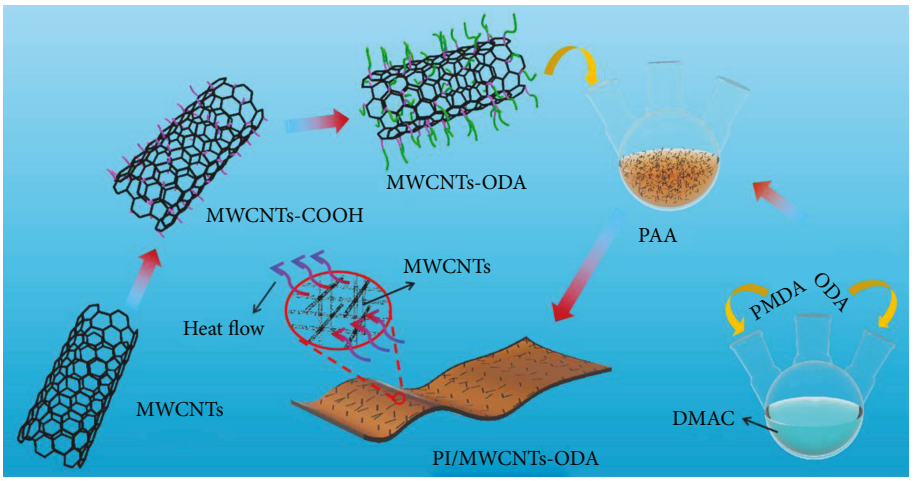

Scheme 2: The preparation process of MWCNTs-ODA/PI composite films.

the composite films was set at 8 wt.%, and the content of MWCNTs-ODA was set at 0 wt.%, 1 wt.%, 1.5 wt.%, 2 wt.%, 2.5 wt.%, 3 wt.%, and 4 wt.%, respectively. The specific synthesis process is shown in Scheme 2.

2.4. Characterization. XRD (X-ray diffraction) patterns of the samples were analyzed by D8 ADVANCE (Bruker Ltd., Germany), employing Cu radiation ($\lambda = 1.5418$ Å). The scanning was performed from 5°-85° at room temperature. FTIR (Fourier Transform infrared spectroscopy) of the samples was recorded by TENSOR II (Bruker Ltd., Germany), scanning from 500 to 4000 cm^{-1}. TEM (transmission electron microscopy) of the samples was analyzed by JEOL JEM-2100 (Japan Electron Optics Laboratory Co. Ltd., Japan). Before the characterizations, the powder samples were dispersed in ethanol and ultrasound was performed for 30-60 minutes. TGA (thermal gravimetric analyses) were conducted on a DSC/TGA Discovery SDT 650 (TA, America) instrument from room temperature to 800°C with a heating rate of 10°C/min in the nitrogen environment. XPS (X-ray photoelectron spectroscopy) of the samples was recorded by ESCALAB 250XI (Thermo Fisher Scientific). Tensile samples were measured by CMT5105 (MTS Corporation, America). The stretching velocity is 500 mm/min, and the sample size is 150 mm × 10 mm × 0.1 mm. SEM (scanning electron microscopy) of the samples was analyzed by Hitachi S-4800 (Hitachi, Japan). The thermal conductivity (λ) of the sample (20 mm × 20 mm × 0.1 mm) was measured by the TPS 2200 Hot Disk instrument (AB Corporation, Sweden). We place the sample between two parallel sensors (3.2 mm diameter), add 0.6 W power heat pulse with the duration of 20 s, and then record the corresponding thermal conductivity. The

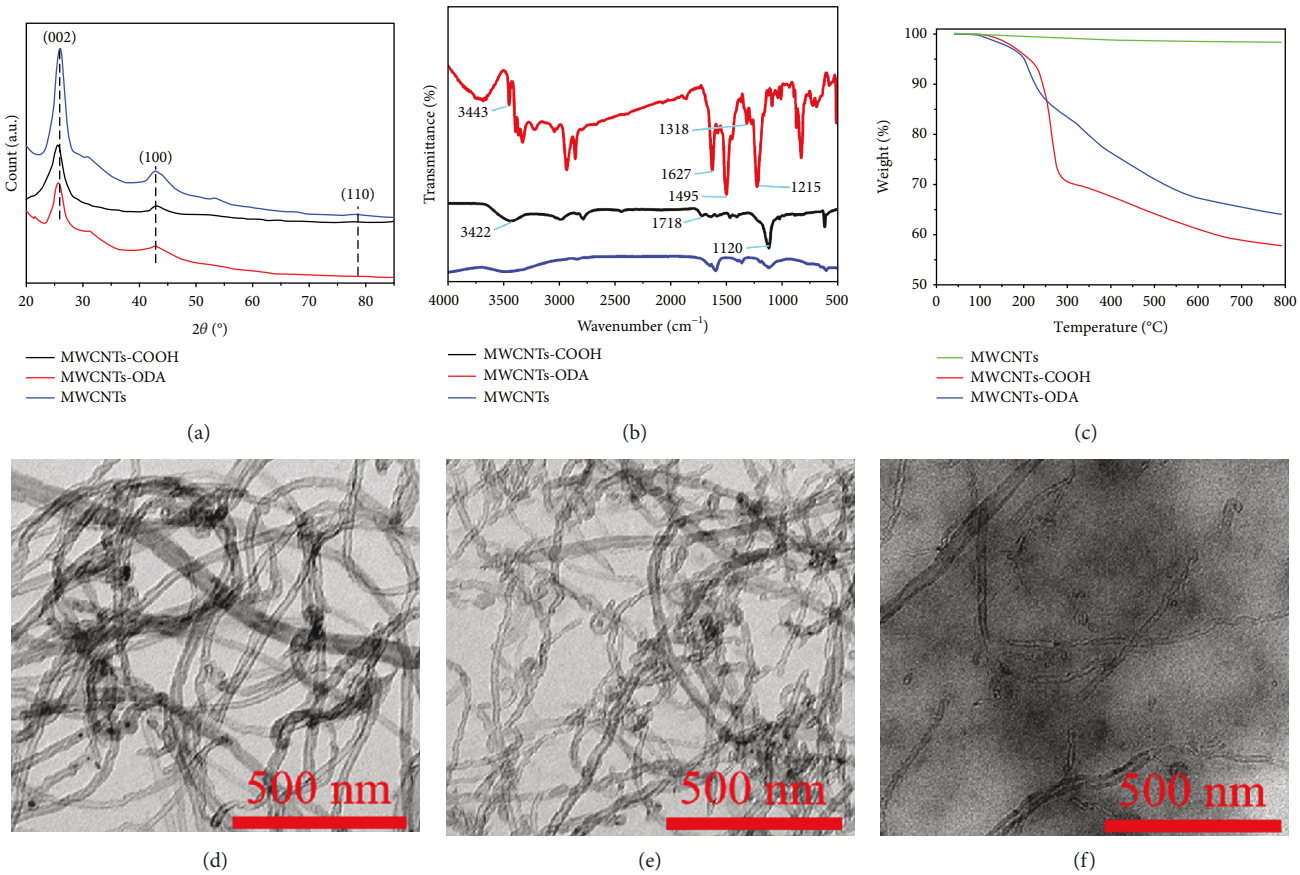

Figure 1: (a) XRD, (b) FTIR, and (c) TGA curves of MWCNTs, MWCNTs-COOH, and MWCNTs-ODA and TEM images of (d) MWCNTs, (e) MWCNTs-COOH, and (f) MWCNTs-ODA.

optical transmittance of composite films was examined by the UV-3600 spectrophotometer (Shimadzu Corporation, Japan); the wavelength range is 200-800 nm.

3. Results and Discussion

3.1. Structure and Performance of MWCNTs, MWCNTs-COOH, and MWCNTs-ODA. The XRD patterns of pure MWCNTs, MWCNTs-COOH, and MWCNTs-ODA are shown in Figure 1(a); it can be seen that the XRD patterns of the pure carbon nanotubes and the modified carbon nanotubes are similar, indicating that the functionalized carbon nanotubes still have the same tubular structure compared with the original carbon nanotubes and the lattice spacing remains unchanged. The pure carbon nanotubes shows strong diffraction peaks at $2\theta = 26^\circ$, 42°, and 77°. The functionalized carbon nanotubes have diffraction peaks at corresponding positions.

The FTIR spectra of pure MWCNTs, MWCNTs-COOH, and MWCNTs-ODA are shown in Figure 1(b); the original carbon nanotubes have no obvious characteristic absorption peaks. In contrast, the MWCNTs-COOH exhibited stretching vibration absorption of C=O and C-O bonds at 1718 cm^{-1} and 1120 cm^{-1} and a characteristic peak of the O-H bond of the carboxyl group appeared at 3422 cm^{-1}. It indicated that the carboxylic acid group was successfully grafted in the surface of the MWCNTs. Due to the formation of the amide bond, a stretching vibration peak of the C=O bond appeared at 1627 cm^{-1}; the characteristic peak at 1318 cm^{-1} is due to the formation of the C-N bond in the amino functional group; the characteristic peak at 1495 cm^{-1} is formed by the C=C bond in the benzene ring; the characteristic peak at 1215 cm^{-1} is formed by the C-O bond in the aromatic ether; and the characteristic peak at 3443 cm^{-1} is due to the N-H bond in the amino functional group. These results suggested that the amino group in the ODA has been successfully grafted onto the CNTs.

The TEM images of pure MWCNTs, MWCNTs-COOH, and MWCNTs-ODA are shown in Figures 1(d)–1(f); the pure CNTs show an obvious agglomeration, and the pipe wall is smooth, with a large aspect ratio and poor dispersion. After introducing the functional group, the aspect ratio of MWCNTs becomes smaller and the dispersion is more uniform, but the tube wall of the CNTs becomes rough. Compared with MWCNTs-COOH, the MWCNTs-ODA have a smaller aspect ratio, a rougher surface, and a significantly improved dispersibility.

The TGA of pure MWCNTs, modified MWCNTs-COOH, and modified MWCNTs-ODA are shown in Figure 1(c); thermogravimetric analysis of functionalized CNTs can provide more detailed information about the thermal stability and surface functionalization. The weight of pure CNTs at 800°C is 98.40%, because the CNTs themselves

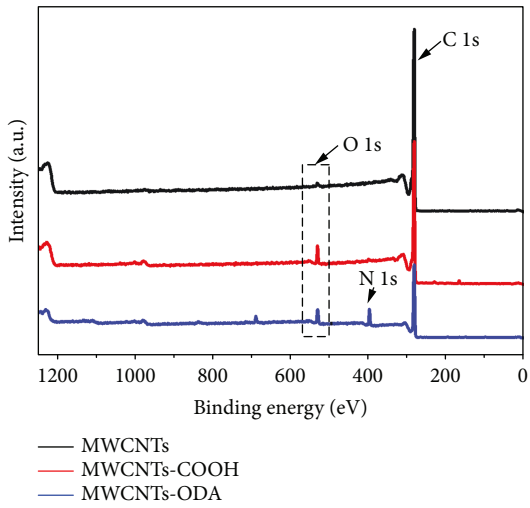

Figure 2: XPS spectrum of MWCNTs, MWCNTs-COOH, and MWCNTs-ODA.

have excellent thermal stability and high temperature resistance, and the weight loss of 1.6% may be due to structural defects of the CNTs themselves. In contrast, carboxylated and aminated CNTs exhibit significant decomposition at lower temperatures. The carboxylated CNTs have a significant weight loss step at 220°C-290°C due to the degradation of carboxyl and hydroxyl groups in MWCNTs-COOH, and the carboxylated CNTs have a residual amount of 57.72% at 800°C. The aminated CNTs have a weight loss of approximately 34.13% in the range of 100°C-700°C; this is mainly due to the thermal decomposition of ODA grafted onto the CNTs. This further demonstrates that ODA is successfully grafted onto the surface of CNTs. In addition, we found that the aminated CNTs have a residual content of 64.07% at 800°C compared to carboxylated CNTs, with higher residuals due to the absence of hydroxyl groups in MWCNTs-ODA, and the benzene ring contained in ODA in MWCNTs-ODA has a stable structure. In other words, replacement of unstable hydroxyl groups in MWCNTs-COOH with more stable ODA groups, MWCNTs-ODA, possesses enhanced thermal stability.

X-ray photoelectron spectroscopy (XPS) analysis was performed to detect the group distribution of the MWCNTs and functionalized MWCNTs. The XPS of pure MWCNTs, modified MWCNTs-COOH, and modified MWCNTs-ODA is shown in Figure 2; the C 1s prominent peak of MWCNTs appeared at 284.8 eV in the test results [49, 50]. Compared with MWCNTs, the O 1s prominent peaks of MWCNTs-COOH and the N 1s prominent peaks of MWCNTs-ODA appeared at 532.6 eV and 399.5 eV, respectively, indicating the presence of O and N atoms in the sample. Among them, MWCNTs-COOH has significantly enhanced O 1s peak intensity compared with MWCNTs. MWCNTs-ODA has new N 1s peaks compared with MWCNTs and MWCNTs-COOH. This all indicates the successful modification of MWCNTs.

The dispersion of DMAc solvent, pure MWCNTs, MWCNTs-COOH, and MWCNTs-ODA is allowed standing for 0 h, 2 h, 4 h, and 8 h, respectively, as shown in Figure 3; we can find that the pure MWCNTs/DMAc mixture showed obvious deposition after standing for 2 h, while the MWCNTs-COOH/DMAc mixture and the MWCNTs-ODA/DMAc mixture dispersed well after standing for 2 h, and there was no obvious deposition appeared. After standing for 4 h and 8 h, the deposition of pure MWCNTs/DMAc mixture became more obvious. The MWCNTs-COOH/DMAc mixture showed deposition after standing for 8 h, while the MWCNTs-ODA/DMAc mixture maintained a very good dispersion. The reason is that after the functionalization of carbon nanotubes, the surface energy can be effectively reduced and the effect of aminated MWCNTs is better, so the dispersibility with organic solvents is better.

3.2. Structural Characterization of the PI and MWCNTs-ODA/PI Composite Films. In order to study the structural characteristics of the pure PI and MWCNTs-ODA/PI composite films, XRD was performed; the result is shown in Figure 4(a). From previous tests, we can know the XRD pattern that the diffraction peak of carbon nanotubes at $2\theta = 26^{\circ}$ is most obvious, while the diffraction peak of PI and MWCNTs-ODA is the same, indicating that the structures of PI chains and MWCNTs do not affect each other. In addition, MWCNTs-ODA has a large lattice spacing, so MWCNTs-ODA has good dispersibility and chemical compatibility in the PI matrix. From the XRD pattern, we found that the XRD of pure PI and MWCNTs-ODA/PI composite films is similar, mainly for two reasons. First, the monomers for synthesizing PI are ODA (diamine) and PMDA (dianhydride). The pure carbon nanotubes are also modified by ODA, so the pure PI and PI composite films contain the same monomer, which is not much different in the XRD pattern. Second, the MWCNTs-ODA content is very small and the performance in XRD is not obvious.

The FTIR was used to detect the chemical bond of the composites [51, 52]. The FTIR spectra of pure PI and MWCNTs-ODA/PI composite films are shown in Figure 4(b); in the FTIR images of pure PI and PI composite films, the characteristic absorption peaks of imide groups appeared at 1778 cm^{-1} and 1707 cm^{-1}, the characteristic peaks of C-N bonds appeared at 1363 cm^{-1}, and the characteristic peaks of C=O bonds appeared at 722 cm^{-1}. It indicated that PI imidization was fully completed. Due to the low content of MWCNTs-ODA in the PI matrix, many functional groups on the surface of MWCNTs-ODA could not be clearly observed in the FTIR results.

3.3. Thermal Properties of the PI and MWCNTs-ODA/PI Composite Films. Thermal stability is an important factor for the application of PI-based composites in high temperature environments [53, 54]. The thermal stability of the films was measured by a TG test under nitrogen atmosphere. The TGA of pure PI and MWCNTs-ODA/PI composite films are shown in Figure 5(a); compared with the work of Kalchounaki et al. [55], the composite film prepared by this work has better thermal stability. The weight loss of the pure PI film at 500°C was 2.1121%, and the residual at 800°C was 55.9794%. It can be seen that the weight loss of the pure PI film and PI/MWCNTs-ODA composite films at 500°C and

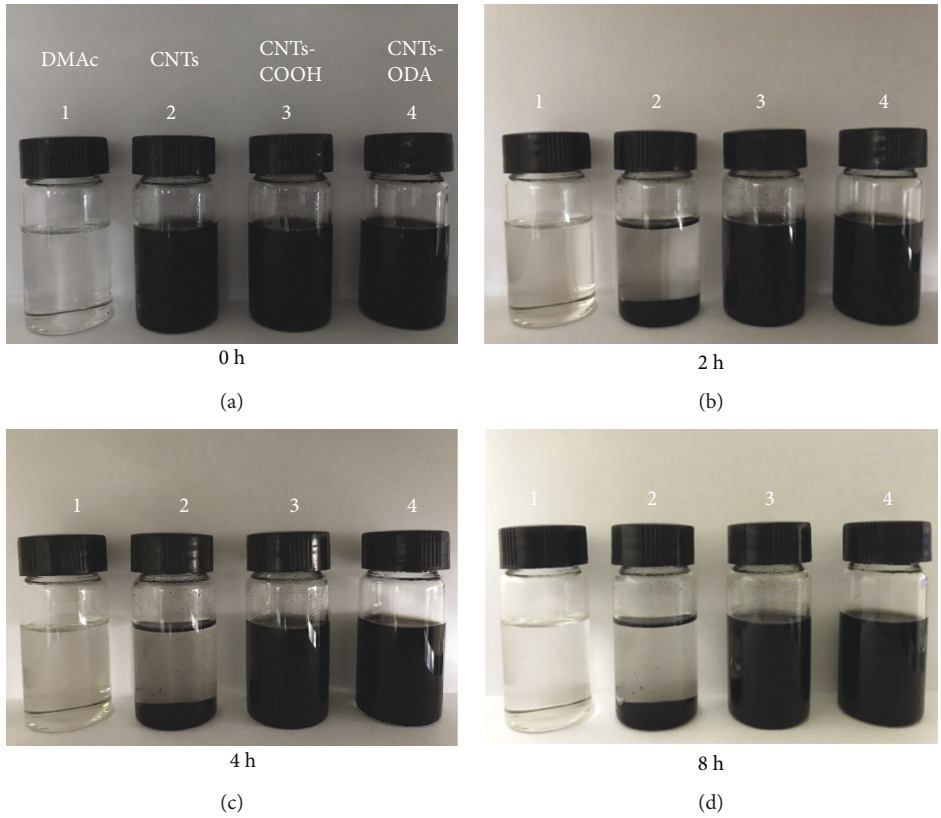

Figure 3: DMAc solvent, pure MWCNTs/DMAc mixture, MWCNTs-COOH/DMAc mixture, and MWCNTs-ODA/DMAc mixture allow standing for (a) 0 h, (b) 2 h, (c) 4 h, and (d) 8 h, respectively.

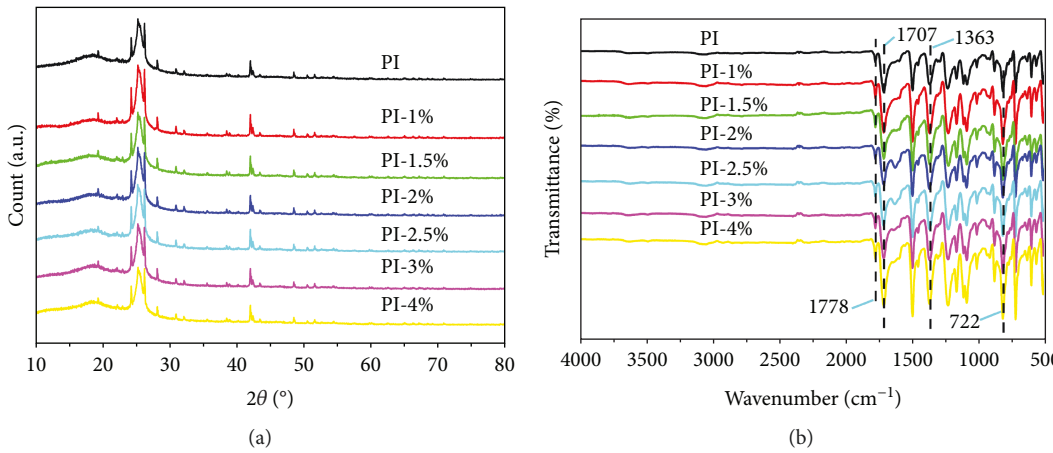

Figure 4: (a) XRD and (b) FTIR curves of pure PI and MWCNTs-ODA/PI composite films.

800°C is not much difference. There are two reasons for this phenomenon: first, only a small amount of aminated carbon nanotubes are added to the PI matrix, so there is no obvious difference in TGA curves; and second, although carbon nanotubes have significant weight loss between 100°C and 700°C after amino functionalization, due to good chemical compatibility and strong interaction between the aminated carbon tubes and the polyimide matrix, when the MWCNTs-ODA content is 3%, the weight loss at 500°C is 1.9077%, When the MWCNTs-ODA content is 3%, the weight loss at 500°C is 1.9077%. The corresponding data of thermal properties are summarized in Table 1.

The thermal conductivity curves of pure PI and MWCNTs-ODA/PI composite films are shown in Figure 5(b); compared with the work of Yan et al. [7], the composite film prepared by this work has better thermal conductivity. When the MWCNTs-ODA content increases from 0 wt.% to 4 wt.%, the thermal conductivity of the PI

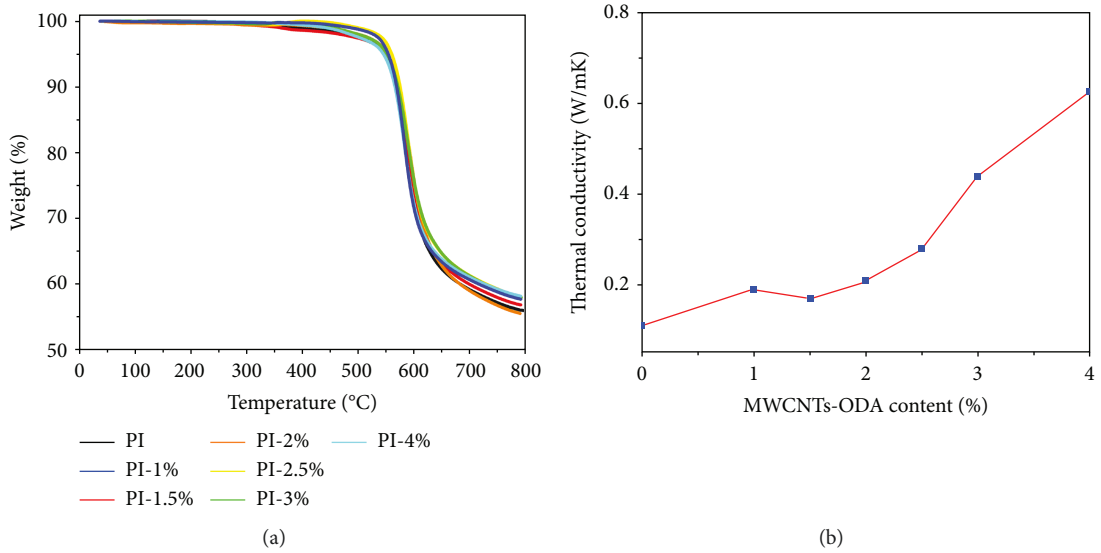

Figure 5: (a) TGA and (b) thermal conductivity curves of pure PI and MWCNTs-ODA/PI composite films.

Table 1: Thermal properties of pure PI and MWCNTs-ODA/PI composite films.

Sample	Thickness (mm)	$T_{5\%}$ (°C)	$T_{10\%}$ (°C)	R_w (%)	References
Pure PI	0.090	553	571	55.9794	
PI-1%	0.073	548	569	57.7443	
PI-1.5%	0.043	554	574	56.8719	
PI-2%	0.075	553	574	55.5747	This work
PI-2.5%	0.049	561	576	58.1314	
PI-3%	0.079	553	573	57.9916	
PI-4%	0.087	546	567	58.2038	
L-GI/MWCNT/PI 5%	—	162	189	46.0000	Kalchounaki et al. [55]

$T_{5\%}$ and $T_{10\%}$: temperature at 5% or 10% weight loss; R_w: residual weight at 800°C.

Table 2: Mechanical properties and thermal conductivity of pure PI and MWCNTs-ODA/PI composite films.

Sample	Pure PI	PI-1%	PI-1.5%	PI-2%	PI-2.5%	PI-3%	PI-4%	MWCNT/PI	BN-c-MWCNT/PI
Tensile strength (MPa)	117.2	126.5	138.4	137.1	140.3	141.5	83.2	135.6	131.9
Thermal conductivity (W/mK)	0.11	0.19	0.17	0.21	0.28	0.44	0.63	0.24	0.38
References	This work							Yan et al. [7]	

The MWCNT and BN-c-MWCNT contents in the reference are both 3 wt.%.

composite film increases with the increase of the MWCNTs-ODA content. Compared with pure PI (0.1366 W/mK), when the WMCNTs-ODA content is 3 wt.%, the thermal conductivity is 0.4397 W/mK. Its thermal conductivity is increased by 221.89%, because when the content of MWCNTs-ODA is low, the CNTs cannot form interconnected heat conduction channels and the carbon nanotubes appear in an isolated state in the PI matrix, which is like an "island-ocean" relationship, so the thermal conductivity is not obviously improved. When the content of carbon nanotubes is increased to 3 wt.%, the thermal conductivity is significantly improved, which is attributed to the fact that the MWCNTs-ODA nanofiller is connected to each other to form a heat conduction channel. The corresponding data of thermal conductivity are summarized in Table 2.

3.4. Mechanical Properties of MWCNTs-ODA/PI Composite Films. The tensile strength of pure PI and MWCNTs-ODA/PI composite films is shown in Figure 6(a); compared with the work of Yan et al. [7], the composite film prepared by this work has better mechanical properties. It can be seen that the tensile strength of the pure PI film is 117.18 MPa. When the MWCNTs-ODA content increased from 0 wt.% to 3 wt.%, the tensile strength of the PI composite films significantly increased, and when the MWCNTs-ODA content was 3 wt.%, the tensile strength reached to 141.48 MPa, compared with pure PI increased by 20.74%. On the one hand, because the MWCNTs-ODA content is below 3 wt.%, the 3D network structure of MWCNTs cross-linking provides the intermolecular bonding force between PI and MWCNTs-ODA. When the composite film is subjected to

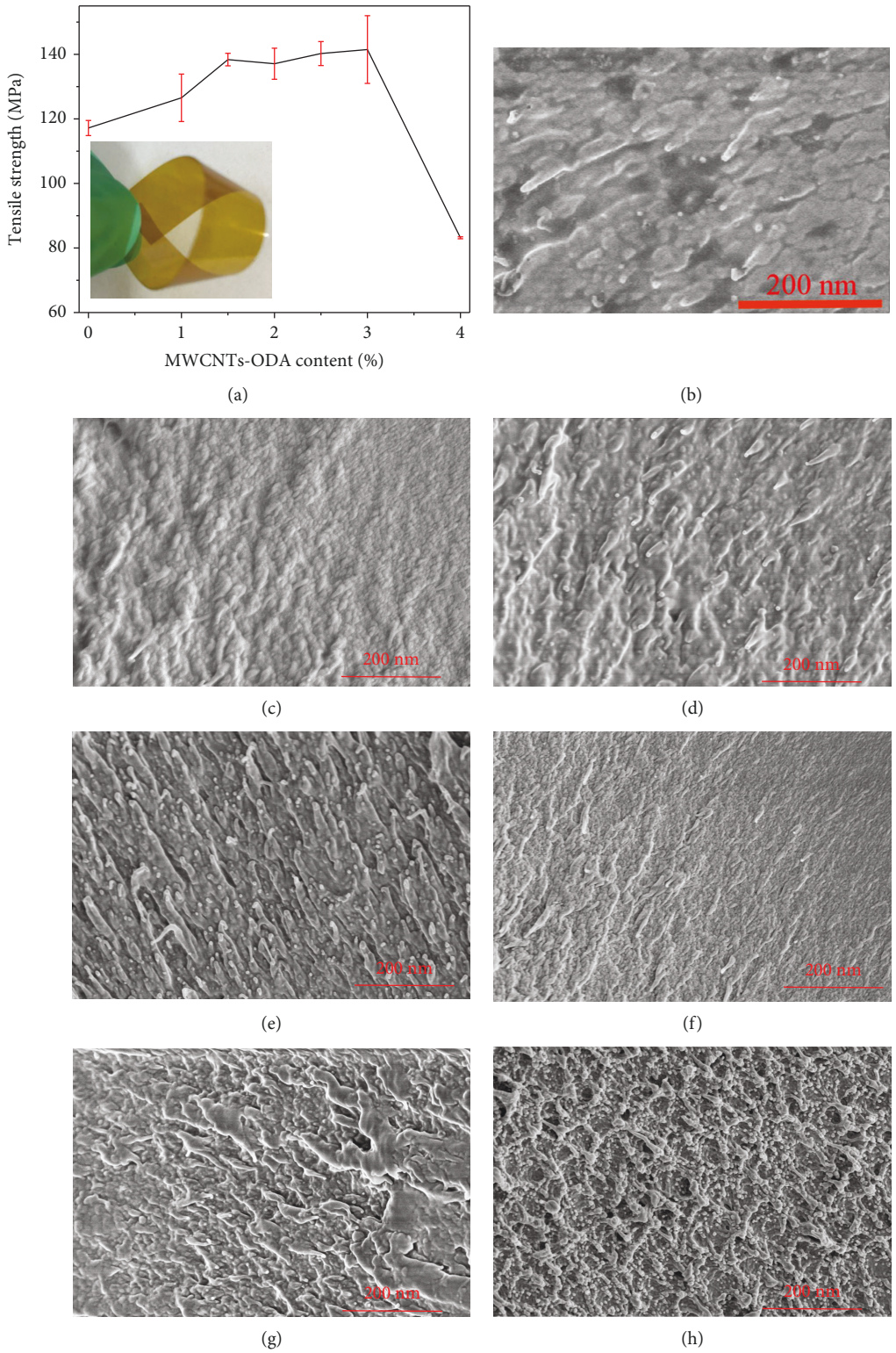

Figure 6: (a) Tensile strength curves of PI composite films and (b–h) SEM images of pure PI and MWCNTs-ODA/PI composite films with the MWCNTs-ODA content of 0 wt.%, 1 wt.%, 1.5 wt.%, 2 wt.%, 2.5 wt.%, 3 wt.%, and 4 wt.%, respectively.

external tensile force, the strong chemical bond between the MWCNTs-ODA and the PI chain can effectively transfer the stress of the PI chain to the surface of the MWCNTs-ODA and thus has excellent mechanical properties. Moreover, due to the good interaction and chemical compatibility between the aminated CNTs and PI matrix, the adhesion between them is obviously enhanced and the mechanical property is improved. However, when the MWCNTs-ODA

content increased from 3 wt.% to 4 wt.%, the tensile strength of the PI composite film decreased significantly, because the additional amount of MWCNTs-ODA reaches the mechanical percolation threshold, and when the MWCNTs-ODA content is lower than this value, the MWCNTs-ODA nanofiller can be well dispersed in the PI matrix and the loading of the composite film can be increased to make the machine works. The performance is significantly improved, and when the MWCNTs-ODA content is higher than this value, the MWCNTs-ODA nanofiller is stacked in the PI matrix, which impairs the improvement of mechanical property. The corresponding data of mechanical properties are summarized in Table 2.

The fracture surface of the tensile test was observed by SEM, and the SEM images of pure PI and 1 wt.%, 1.5 wt.%, 2 wt.%, 2.5 wt.%, 3 wt.%, and 4 wt.% MWCNTs-ODA/PI composite films are shown in Figures 6(b)–6(h), respectively; when the MWCNTs-ODA content is increased from 0 wt.% to 3 wt.%, it can be seen from the SEM image that the cross section of the MWCNTs-ODA/PI composite film has obvious break marks and the composite film is ductile fracture. At this time, the tensile strength of the MWCNTs-ODA/PI composite film increases with the increase of the MWCNTs-ODA content. In addition, when the content of MWCNTs-ODA is 3 wt.%, compared with pure PI, the cross section surface of the PI composite film is rough and there is obvious fracture surface in the enlarged view, due to the excellent interfacial adhesion and well compatibility between the PI matrix and the MWCNTs-ODA nanofiller; it is advantageous to transfer the tensile pressure from the polymer matrix to the MWCNTs-ODA nanofiller. When the MWCNTs-ODA content was increased from 3 wt.% to 4 wt.%, it can be seen from the SEM image that the cross section became significantly rougher and the MWCNTs-ODA/PI composite film was brittle fracture. Correspondingly, the tensile strength of the MWCNTs-ODA/PI composite film showed a significant decrease. Therefore, we conclude that the strong interaction between the nanofiller and the PI matrix makes the MWCNTs-ODA have good dispersibility and this is an important reason for the enhancement of mechanical properties of MWCNTs-ODA/PI nanocomposite films.

3.5. Optical Properties of MWCNTs-ODA/PI Composite Films. The optical properties of MWCNTs-ODA/PI composite films are shown in Figure 7; it shows the optical transmission of the MWCNTs-ODA/PI composite films with a thickness of 43-90 μm in the range of 200-800 nm. The test was carried out with reference to a pure PI film. Due to the introduction of MWCNTs-ODA, the transmittance of composite films decreased from 92.172% (PI-1.5%) to 63.164% (PI-4%), and with the increase of the MWCNTs-ODA content, the color of the films became significantly deeper. The addition of MWCNTs-ODA has a significant effect on the optical properties of MWCNTs-ODA/PI composite films. When the content of MWCNTs-ODA is small, the difference in transmittance of the composite film is not obvious, because the MWCNTs-ODA content is extremely small, resulting in little change in light transmittance.

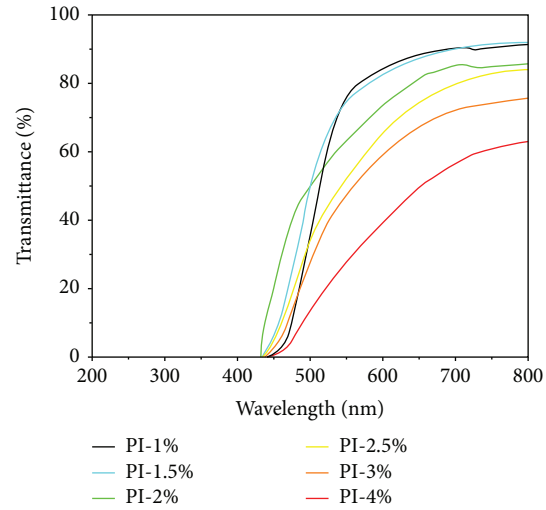

Figure 7: UV-vis spectral curves of PI composite films.

4. Conclusions

In summary, the XRD, FTIR, and XPS tests of MWCNT and MWCNTs-ODA demonstrated that the amino group was successfully grafted on CNTs without destroying the chemical structure of CNTs. The SEM, XRD, and FTIR tests of MWCNTs-ODA/PI composite films confirmed that the addition of MWCNTs-ODA did not destroy the structure and properties of the PI matrix and there was a strong interaction between MWCNTs-ODA and PI matrix and good chemical compatibility between MWCNTs-ODA and PI matrix. Through TGA data of pure PI and MWCNTs-ODA/PI composite films, we found that the addition of MWCNTs-ODA has little effect on the thermal stability of the PI matrix and the composite films has excellent thermal stability, which will not have significant weight loss before 500°C. Through the tensile test of the MWCNTs-ODA/PI composite film, we found that when the MWCNTs-ODA content is 3 wt.%, the tensile strength of the PI composite film is 141.48 MPa, which is 20.74% higher than that of the pure PI film. Through the thermal conductivity test of MWCNTs-ODA/PI composite films, we found that when the content of MWCNTs-ODA is 3 wt.%, the thermal conductivity of the PI composite film is 0.4397 W/mK, which is 221.89% higher than that of the pure PI film. Therefore, when the MWCNTs-ODA content is 3 wt.%, the MWCNTs-ODA/PI composite film has the best comprehensive performance, has excellent thermal conductivity and thermal stability, and might be further used as a potential heat dissipation material in the field of microelectronics and flexible circuit boards. In addition, we also found that as the MWCNTs-ODA content increases, the light transmittance is significantly reduced.

Data Availability

The data used to support the findings of this study are included within the article.

Disclosure

The authors Min Chao and Yanming Li should be considered co-first authors.

Conflicts of Interest

The authors declare that there is no conflict of interest regarding the publication of this paper.

Authors' Contributions

The authors Min Chao and Yanming Li contributed equally to this work.

Acknowledgments

This work was financially supported by the Special Fund for Basic Scientific Research of Central Colleges, Chang'an University (Nos. 300102318403 and 300102319306), the National Science Foundation of China (No. 51407134), the China Postdoctoral Science Foundation (No. 2016M590619), the College Students Innovation and Entrepreneurship Training Program (No. 201810710121), the Natural Science Foundation of Shandong Province (No. ZR2019YQ24), and the Key Laboratory of Engineering Dielectrics and Its Application (Harbin University of Science and Technology), Ministry of Education. The authors also thank their colleagues in their laboratory for their support.

References

[1] Q. Jiang, X. Wang, Y. Zhu, D. Hui, and Y. Qiu, "Mechanical, electrical and thermal properties of aligned carbon nanotube/-polyimide composites," *Composites Part B: Engineering*, vol. 56, pp. 408–412, 2014.

[2] G. Wu, Y. Cheng, Z. Wang, K. Wang, and A. Feng, "In situ polymerization of modified graphene/polyimide composite with improved mechanical and thermal properties," *Journal of Materials Science: Materials in Electronics*, vol. 28, no. 1, pp. 576–581, 2017.

[3] M. Cai, J. Zhu, C. Yang, R. Gao, C. Shi, and J. Zhao, "A parallel bicomponent TPU/PI membrane with mechanical strength enhanced isotropic interfaces used as polymer electrolyte for lithium-ion battery," *Polymers*, vol. 11, no. 1, p. 185, 2019.

[4] M. Chao, "Synthesis and characterization of semicrystalline polyimides containing bridged linkages," *International Journal of Polymer Science*, vol. 2018, Article ID 8590567, 7 pages, 2018.

[5] Z. Ahmad and J. E. Mark, "Polyimide-ceramic hybrid composites by the sol-gel route," *Chemistry of Materials*, vol. 13, no. 10, pp. 3320–3330, 2001.

[6] S. Jiang, H. Hou, S. Agarwal, and A. Greiner, "Polyimide nanofibers by "green" electrospinning via aqueous solution for filtration applications," *ACS Sustainable Chemistry & Engineering*, vol. 4, no. 9, pp. 4797–4804, 2016.

[7] W. Yan, Y. Zhang, H. Sun et al., "Polyimide nanocomposites with boron nitride-coated multi-walled carbon nanotubes for enhanced thermal conductivity and electrical insulation," *Journal of Materials Chemistry A*, vol. 2, no. 48, pp. 20958–20965, 2014.

[8] J. Dong, C. Yin, X. Zhao, Y. Li, and Q. Zhang, "High strength polyimide fibers with functionalized graphene," *Polymer*, vol. 54, no. 23, pp. 6415–6424, 2013.

[9] X. Xue, H. Yan, and Y. Fu, "Preparation of pure and metal-doped $Li_4Ti_5O_{12}$ composites and their lithium-storage performances for lithium-ion batteries," *Solid State Ionics*, vol. 335, pp. 1–6, 2019.

[10] Z. Li, K. Kou, J. Xue, C. Pan, and G. Wu, "Study of triazine-based-polyimides composites working as gel polymer electrolytes in ITO-glass based capacitor devices," *Journal of Materials Science: Materials in Electronics*, vol. 30, no. 4, pp. 3426–3431, 2019.

[11] W. Dai, J. Yu, Z. Liu et al., "Enhanced thermal conductivity and retained electrical insulation for polyimide composites with SiC nanowires grown on graphene hybrid fillers," *Composites Part A: Applied Science and Manufacturing*, vol. 76, pp. 73–81, 2015.

[12] L. Zuo, W. Fan, Y. Zhang et al., "Graphene/montmorillonite hybrid synergistically reinforced polyimide composite aerogels with enhanced flame-retardant performance," *Composites Science and Technology*, vol. 139, pp. 57–63, 2017.

[13] Y. Qin, Q. Peng, Y. Ding et al., "Lightweight, superelastic, and mechanically flexible graphene/polyimide nanocomposite foam for strain sensor application," *ACS Nano*, vol. 9, no. 9, pp. 8933–8941, 2015.

[14] T. Zhang, Y. Zhao, and K. Wang, "Polyimide aerogels cross-linked with aminated Ag nanowires: mechanically strong and tough," *Polymers*, vol. 9, no. 12, p. 530, 2017.

[15] Y. Song, H. Yao, H. Tan et al., "Synthesis and memory characteristics of highly organo-soluble hyperbranched polyimides with various electron acceptors," *Journal of Polymer Science Part A: Polymer Chemistry*, vol. 55, no. 14, pp. 2281–2288, 2017.

[16] X. Li, J. Wang, Y. Zhao, and X. Zhang, "Template-free self-assembly of fluorine-free hydrophobic polyimide aerogels with lotus or petal effect," *ACS Applied Materials & Interfaces*, vol. 10, no. 19, pp. 16901–16910, 2018.

[17] X. Lei, M. Qiao, L. Tian, Y. Chen, and Q. Zhang, "Tunable permittivity in high-performance hyperbranched polyimide films by adjusting backbone rigidity," *The Journal of Physical Chemistry C*, vol. 120, no. 5, pp. 2548–2561, 2016.

[18] S. Han, J. T. Lin, Y. Yamada, and D. D. L. Chung, "Enhancing the thermal conductivity and compressive modulus of carbon fiber polymer–matrix composites in the through-thickness direction by nanostructuring the interlaminar interface with carbon black," *Carbon*, vol. 46, no. 7, pp. 1060–1071, 2008.

[19] C. K. Leong, Y. Aoyagi, and D. D. L. Chung, "Carbon black pastes as coatings for improving thermal gap-filling materials," *Carbon*, vol. 44, no. 3, pp. 435–440, 2006.

[20] X. Liang, Y. Yang, X. Jin, Z. Huang, and F. Kang, "The high performances of SiO_2/Al_2O_3-coated electrospun polyimide fibrous separator for lithium-ion battery," *Journal of Membrane Science*, vol. 493, pp. 1–7, 2015.

[21] H. Wang, H. Li, L. Yu, Y. Jiang, and K. Wang, "Synthesis of porous Al_2O_3-PVDF composite separators and their application in lithium-ion batteries," *Journal of Applied Polymer Science*, vol. 130, no. 4, pp. 2886–2890, 2013.

[22] Y. Zhou, H. Wang, L. Wang et al., "Fabrication and characterization of aluminum nitride polymer matrix composites with high thermal conductivity and low dielectric constant for electronic packaging," *Materials Science and Engineering: B*, vol. 177, no. 11, pp. 892–896, 2012.

[23] B. L. Zhu, J. Wang, J. Ma, J. Wu, K. C. Yung, and C. S. Xie, "Preparation and properties of aluminum nitride-filled epoxy composites: effect of filler characteristics and composite processing conditions," *Journal of Applied Polymer Science*, vol. 127, no. 5, pp. 3456–3466, 2013.

[24] Y. Zhou, L. Wang, H. Zhang, Y. Bai, Y. Niu, and H. Wang, "Enhanced high thermal conductivity and low permittivity of polyimide based composites by core-shell Ag@SiO2 nanoparticle fillers," *Applied Physics Letters*, vol. 101, no. 1, article 012903, 2012.

[25] M. Shanthil, R. Thomas, R. S. Swathi, and K. George Thomas, "$Ag@SiO_2$ core–shell nanostructures: distance-dependent plasmon coupling and SERS investigation," *The Journal of Physical Chemistry Letters*, vol. 3, no. 11, pp. 1459–1464, 2012.

[26] G. Wu, J. Li, K. Wang, Y. Wang, C. Pan, and A. Feng, "In situ synthesis and preparation of TiO_2/polyimide composite containing phenolphthalein functional group," *Journal of Materials Science: Materials in Electronics*, vol. 28, no. 9, pp. 6544–6551, 2017.

[27] Z. Yuan, J. Yu, B. Rao et al., "Enhanced thermal properties of epoxy composites by using hyperbranched aromatic polyamide grafted silicon carbide whiskers," *Macromolecular Research*, vol. 22, no. 4, pp. 405–411, 2014.

[28] Y. Niu, X. Zhang, J. Zhao, Y. Tian, Y. Li, and X. Yan, "Preparation, characterization and properties of amine-functionalized silicon carbide/polyimide composite films," *RSC Advances*, vol. 4, no. 54, article 28456, 2014.

[29] W. Zhou, C. Wang, T. Ai, K. Wu, F. Zhao, and H. Gu, "A novel fiber-reinforced polyethylene composite with added silicon nitride particles for enhanced thermal conductivity," *Composites Part A: Applied Science and Manufacturing*, vol. 40, no. 6-7, pp. 830–836, 2009.

[30] Y. Zhou, H. Hyuga, D. Kusano, Y. Yoshizawa, and K. Hirao, "A tough silicon nitride ceramic with high thermal conductivity," *Advanced Materials*, vol. 23, no. 39, pp. 4563–4567, 2011.

[31] J. Hou, G. Li, N. Yang et al., "Preparation and characterization of surface modified boron nitride epoxy composites with enhanced thermal conductivity," *RSC Advances*, vol. 4, no. 83, pp. 44282–44290, 2014.

[32] K. Sato, H. Horibe, T. Shirai et al., "Thermally conductive composite films of hexagonal boron nitride and polyimide with affinity-enhanced interfaces," *Journal of Materials Chemistry*, vol. 20, no. 14, p. 2749, 2010.

[33] S. Uchida, T. Murakami, T. Iwamura, R. Ishige, and S. Ando, "Enhanced thermal conductivity in immiscible polyimide blend composites with needle-shaped ZnO particles," *RSC Advances*, vol. 7, no. 25, pp. 15492–15499, 2017.

[34] D. Yorifuji and S. Ando, "Enhanced thermal conductivity over percolation threshold in polyimide blend films containing ZnO nano-pyramidal particles: advantage of vertical double percolation structure," *Journal of Materials Chemistry*, vol. 21, no. 12, p. 4402, 2011.

[35] P. Kim, L. Shi, A. Majumdar, and P. L. McEuen, "Thermal transport measurements of individual multiwalled nanotubes," *Physical Review Letters*, vol. 87, no. 21, article 215502, 2001.

[36] R. H. Baughman, C. Cui, A. A. Zakhidov et al., "Carbon nanotube actuators," *Science*, vol. 284, no. 5418, pp. 1340–1344, 1999.

[37] M. J. Esplandiu, V. G. Bittner, K. P. Giapis, and C. P. Collier, "Nanoelectrode scanning probes from fluorocarbon-coated single-walled carbon nanotubes," *Nano Letters*, vol. 4, no. 10, pp. 1873–1879, 2004.

[38] M. Cadek, J. N. Coleman, K. P. Ryan et al., "Reinforcement of polymers with carbon nanotubes: the role of nanotube surface area," *Nano Letters*, vol. 4, no. 2, pp. 353–356, 2004.

[39] C. Wei, D. Srivastava, and K. Cho, "Thermal expansion and diffusion coefficients of carbon nanotube-polymer composites," *Nano Letters*, vol. 2, no. 6, pp. 647–650, 2002.

[40] K. Wang, Y. H. Chang, C. Zhang, and B. Wang, "Conductive-on-demand: tailorable polyimide/carbon nanotube nanocomposite thin film by dual-material aerosol jet printing," *Carbon*, vol. 98, pp. 397–403, 2016.

[41] L. Yan, G. Zhang, L. Zhang et al., "Robust construction of underwater superoleophobic CNTs/nanoparticles multifunctional hybrid membranes via interception effect for oily wastewater purification," *Journal of Membrane Science*, vol. 569, pp. 32–40, 2019.

[42] S. Song, Y. Zhai, and Y. Zhang, "Bioinspired graphene oxide/-polymer nanocomposite paper with high strength, toughness, and dielectric constant," *ACS Applied Materials & Interfaces*, vol. 8, no. 45, pp. 31264–31272, 2016.

[43] Z. Wang, X. Shen, M. Akbari Garakani et al., "Graphene aerogel/epoxy composites with exceptional anisotropic structure and properties," *ACS Applied Materials & Interfaces*, vol. 7, no. 9, pp. 5538–5549, 2015.

[44] W. H. Liao, S. Y. Yang, J. Y. Wang et al., "Effect of molecular chain length on the mechanical and thermal properties of amine-functionalized graphene oxide/polyimide composite films prepared by in situ polymerization," *ACS Applied Materials & Interfaces*, vol. 5, no. 3, pp. 869–877, 2013.

[45] J. F. Wang, X. X. Jin, H. Wu, and S. Y. Guo, "Polyimide reinforced with hybrid graphene oxide @ carbon nanotube: toward high strength, toughness, electrical conductivity," *Carbon*, vol. 123, pp. 502–513, 2017.

[46] X. L. Li, J. L. Lan, M. Ai, Y. G. Guo, Q. Cai, and X. P. Yang, "Biomineralization on polymer-coated multi-walled carbon nanotubes with different surface functional groups," *Colloids and Surfaces B: Biointerfaces*, vol. 123, pp. 753–761, 2014.

[47] X. H. Chen, J. F. Wang, M. Lin et al., "Mechanical and thermal properties of epoxy nanocomposites reinforced with amino-functionalized multi-walled carbon nanotubes," *Materials Science and Engineering: A*, vol. 492, no. 1-2, pp. 236–242, 2008.

[48] Y. Chen, D. X. Li, W. Y. Yang, C. G. Xiao, and M. L. Wei, "Effects of different amine-functionalized graphene on the mechanical, thermal, and tribological properties of polyimide nanocomposites synthesized by in situ polymerization," *Polymer*, vol. 140, pp. 56–72, 2018.

[49] H. Yan, Y. Fu, X. Wu, X. Xue, C. Li, and L. Zhang, "Core-shell structured $NaTi_2(PO_4)_3$@polyaniline as an efficient electrode material for electrochemical energy storage," *Solid State Ionics*, vol. 336, pp. 95–101, 2019.

[50] H. Zhang, B. Wang, A. Feng et al., "Mesoporous carbon hollow microspheres with tunable pore size and shell thickness as efficient electromagnetic wave absorbers," *Composites Part B: Engineering*, vol. 167, pp. 690–699, 2019.

[51] J. Li, J. Ma, S. Chen, J. He, and Y. Huang, "Characterization of calcium alginate/deacetylated konjac glucomannan blend films prepared by Ca^{2+} crosslinking and deacetylation," *Food Hydrocolloids*, vol. 82, pp. 363–369, 2018.

[52] J. Li, J. Ma, S. Chen, Y. Huang, and J. He, "Adsorption of lysozyme by alginate/graphene oxide composite beads with

enhanced stability and mechanical property," *Materials Science and Engineering C*, vol. 89, pp. 25–32, 2018.

[53] Z. Wang, M. Yang, Y. Cheng et al., "Dielectric properties and thermal conductivity of epoxy composites using quantum-sized silver decorated core/shell structured alumina/polydopamine," *Composites: Part A*, vol. 118, pp. 302–311, 2019.

[54] A. Feng, G. Wu, C. Pan, and Y. Wang, "Synthesis, preparation and mechanical property of wood fiber-reinforced poly(vinyl chloride) composites," *Journal of Nanoscience and Nanotechnology*, vol. 17, no. 6, pp. 3859–3863, 2017.

[55] E. K. Kalchounaki, A. Farhadi, and A. Zadehnazari, "Preparation and properties evaluation of polyimide-matrix nanocomposites reinforced with glutamine functionalized multi-walled carbon nanotube," *Polymer Bulletin*, vol. 75, no. 12, pp. 5731–5744, 2018.